Elias Rabel

Numerical Time Evolution of 1D Quantum Systems

DIPLOMARBEIT

zur Erlangung des akademischen Grades
Diplom-Ingenieur

Diplomstudium Technische Physik

Technische Universität Graz

Betreuer:
Ao.Univ.-Prof. Dipl.-Phys. Dr.rer.nat. Hans Gerd Evertz
Institut für Theoretische Physik - Computational Physics

Graz, Oktober 2010

Zusammenfassung

Diese Diplomarbeit beschäftigt sich mit der Simulation der Zeitentwicklung quantenmechanischer Vielteilchensysteme in einer Dimension. Dazu wurde ein Computerprogramm entwickelt, das den TEBD (Time Evolving Block Decimation) – Algorithmus verwendet. Dieser basiert auf Matrixproduktzuständen und weist interessante Verbindungen zur Quanteninformationstheorie auf. Die Verschränkung eines quantenmechanischen Zustandes hat dabei Einfluss auf die Simulierbarkeit des Systems. Unter Ausnützung einer erhaltenen Quantenzahl erreicht man eine Optimierung des Programms.

Als Anwendungen dienten fermionische Systeme in einer Dimension. Dabei wurde die Ausbreitung einer Störung der Teilchendichte simuliert, welche durch äußere Felder erzeugt wurde. Trifft diese Störung auf eine Wechselwirkungsbarriere, so treten Reflektionen auf, die sowohl positive als auch negative Änderungen der Teilchendichte sein können. Die negativen Reflektionen werden auch als Andreev-artige Reflektionen bezeichnet, benannt nach einem ähnlichen Effekt an einer Metall-Supraleiter-Grenze. Aus analytischen Rechnungen ist bekannt, dass diese Reflektionen im idealisierten Luttinger-Flüssigkeitsmodell für schwache Störungen existieren.

Das erste untersuchte Modell war eine Kette spinloser Fermionen, für die bereits publizierte Ergebnisse zur Andreev-artigen Reflektion erfolgreich reproduziert werden konnten. Einfache Konvergenzbetrachtungen zu diesen Ergebnissen wurden durchgeführt. Danach wurde das eindimensionale Hubbard-Modell auf ähnliche Art untersucht. Die Trennung von Spin und Ladung wurde demonstriert. Andreev-artige Reflektionen konnten mit passenden Parametern auch bei einer Hubbard-Kette in der Ladungsdichte nachgewiesen werden.

Abstract

The topic of this diploma thesis is the numerical simulation of the time evolution of quantum many-body systems in one dimension. A computer program was developed, which implements the TEBD (Time Evolving Block Decimation) - algorithm. This algorithm uses matrix product states and has interesting connections with quantum information theory. The amount of entanglement of the quantum state influences the system's simulatability. The program is optimized by exploiting the conservation of a quantum number.

The program was then applied to fermionic systems in one dimension. Specifically, the propagation of a particle density perturbation created by external fields was simulated. When this perturbation hits an interaction barrier, reflections occur, which can be positive or negative deviations of the particle density. The negative reflections are also known as Andreev-like reflections, related to a similar effect at a metal-superconductor boundary. They have been shown analytically to exist for weak perturbations in the idealised Luttinger liquid model.

The first model studied was a chain of spinless fermions, for which already published results on Andreev-like reflection were successfully reproduced. Convergence of these results was examined. Then the one dimensional Hubbard model was studied in a similar manner. The separation of spin and charge was demonstrated. It could be shown that Andreev-like reflection exists in the charge density of the full Hubbard model with suitable parameters.

Contents

Chapter 1

Introduction

Calculating the time evolution of a quantum state is a very promising approach in the theory of strongly correlated systems, because knowing a state at all (or up to a time long enough) points in time, gives access to the whole dynamical behaviour of a system. While it is in principle possible to calculate dynamical correlation functions from the time evolution, publications in this field usually deal with the real time behaviour of quantum systems itself.

It was only after the invention of methods such as the tDMRG variants (time dependent density matrix renormalization group) and the TEBD (Time Evolving Block Decimation) algorithm that numerical calculations of the evolution of quantum systems in real time, at least for one dimensional systems, became feasible. Approaches for 2D systems exist but are limited to small system sizes.

The TEBD algorithm by Guifré Vidal has its roots in quantum information theory. In [1] Vidal showed that efficient simulation of a quantum computation is possible, if the amount of entanglement involved is sufficiently low. Efficiency in this case means that the algorithm has a run-time that is upper bounded by a polynomial in the system size* - in contrast to e.g. a full diagonalisation of the Hamiltonian, where the run-time scales exponentially with system size. (See also section 4.4)

TEBD is an adaptive Hilbert space method, which means that at each TEBD step, only a few basis vectors are selected that form a low dimensional Hilbert space, in which the time-evolved quantum state is faithfully represented. The procedure that selects the most important basis vectors (Hilbert space truncation) is the same as in the successful density matrix renormalisation group (DMRG) [2, 3].

This work is organised as follows: In the following sections of **chap-**

*Note that for practical applications the order of the polynomial has to be low.

ter 1 the calculation of time evolutions for time-independent Hamiltonians is discussed. By decomposing the time evolution operator into a series of operators that act on two neighbouring sites, the equivalence of the approximate simulation of a time evolution with a quantum computation is shown.

In **chapter 2** basic quantum information theoretical notions are introduced, which are necessary for the development of the time evolving block decimation algorithm (TEBD). This includes the Schmidt decomposition of a quantum state and its link to the entanglement of quantum systems. As entanglement is a central property of many-particle quantum systems, being able to quantify the amount of entanglement turns out to be useful. If a system in a pure state is split into two parts, the entanglement between them is called the bipartite entanglement. It can be quantified by the von Neumann entropy of the reduced density matrix of one of the two parts or by the upper bound of the von Neumann entropy.

Chapter 3 introduces an efficient representation for certain quantum states, which is called the matrix product state (MPS) representation. One can show that such a representation can also be derived by Schmidt decompositions (canonical normal form). The connection between the entanglement of a state and its matrix product state representation is discussed.

Chapter 4 introduces the time evolving block decimation algorithm (TEBD), which consists of the application of two-site operators on a matrix product state. Error sources due to approximative steps in the algorithm are mentioned. An optimisation possibility using conserved additive quantum numbers is presented. Part of this work was also the implementation of this algorithm as a C++-program.

Chapter 5 gives a short introduction to interacting fermions in one dimension. Lattice models for fermions include the spinless fermion model and the Hubbard model for fermions with spin. A field theoretical (continuum) description is provided by the Luttinger liquid theory. Density perturbations created by external fields that are suddenly switched of can propagate through the system. If they enter a region with different interactions, reflection phenomena occur (normal and hole-like reflection). Applications of the TEBD algorithm on these effects are given in **chapter 6**.

1.1 Time Evolution of Quantum Systems

The time-evolution of a quantum system is given by the time-dependent Schrödinger equation.

$$i\hbar\frac{\partial}{\partial t}\left|\Psi(t)\right\rangle = \hat{H}\left|\Psi(t)\right\rangle \tag{1.1}$$

For notational simplicity it is reasonable to choose units in a way that $\hbar = 1$. The equation can be rewritten in terms of the time evolution operator $\hat{U}$, incorporating the initial condition given by the initial state $|\Psi(0)\rangle$:

$$\left|\Psi(t)\right\rangle = \hat{U}\left|\Psi(0)\right\rangle \tag{1.2}$$

In the case of a not explicitly time-dependent Hamiltonian H the time evolution operator is given by:

$$\hat{U} = e^{-i\hat{H}t} \tag{1.3}$$

From that we can see that the time-evolution of an eigenstate $|\Psi_E\rangle$ with energy E is trivial, giving just a time-dependent phase factor:

$$\left|\Psi_E(t)\right\rangle = e^{-iEt}\left|\Psi_E(0)\right\rangle \tag{1.4}$$

For non-stationary processes, however, the calculation of the time evolution provides additional valuable insights. Non-stationary processes can be created for example by modifying an eigenstate of the system by application of certain operators. The eigenstate of choice will be most likely the ground state (note: can be degenerate of course) of the system, due to his distinguished nature, being the state with the lowest energy. Another possibility is the sudden change of coupling parameters in the Hamiltonian at t = 0, which is a so-called "quantum quench". This can be done in two ways: Either spatially localized at one or a few bonds between quantum mechanical subsystems ("local quench") or by a coupling change affecting the whole system ("global quench"). As there is a sudden change of the couplings, the Hamiltonian becomes in fact time-dependent, which can be treated as a sudden change of the time evolution operator and we can restrict our discussion to the time-independent case. Another possibility is to suddenly change an external field which is the preferred method in this work.

1.2 Time Evolution as Quantum Computation

The Hamiltonian in most cases that are physically relevant consists only of local interactions (e. g. nearest-neighbour interactions), which means that

it consists of a sum of operators that act only at a few quantum subsystems close together. In the following sections only nearest-neighbor interactions will be discussed, therefore the Hamiltonian of an 1D system with open boundary conditions can be written as a sum of two-site operators $\hat{k}_{l,\,l+1}$ and single-site operators $\hat{b}_l$ (e.g. magnetic field terms) [4]:

$$\hat{H} = \sum_{l=1}^{L-1} \hat{k}_{l,l+1} + \sum_{l=1}^{L} \hat{b}_l \tag{1.5}$$

Single-site operator parts $\hat{b}_l$ of the Hamiltonian can be incorporated into the two-site-operator parts $\hat{k}_{l,l+1}$ by noting that

$$\begin{aligned}\hat{H} &= \sum_{l=1}^{L-1} \hat{k}_{l,l+1} + \sum_{l=1}^{L} \hat{b}_l \\ &= \sum_{l=1}^{L-1} \left[\hat{k}_{l,l+1} + \frac{\hat{b}_l}{2} \otimes \mathbb{1} + \mathbb{1} \otimes \frac{\hat{b}_{l+1}}{2} + \delta_{l,1} \left(\frac{\hat{b}_1}{2} \otimes \mathbb{1} \right) + \delta_{l,L-1} \left(\mathbb{1} \otimes \frac{\hat{b}_L}{2} \right) \right]\end{aligned}$$

Then the Hamiltonian consists of a sum of two-site operators $h_{l,l+1}$ only:

$$\hat{H} = \sum_{l=1}^{L-1} \hat{h}_{l,\,l+1} \tag{1.6}$$

with

$$\hat{h}_{l,l+1} = \hat{k}_{l,l+1} + \frac{\hat{b}_l}{2} \otimes \mathbb{1} + \mathbb{1} \otimes \frac{\hat{b}_{l+1}}{2} + \delta_{l,1} \left(\frac{\hat{b}_1}{2} \otimes \mathbb{1} \right) + \delta_{l,L-1} \left(\mathbb{1} \otimes \frac{\hat{b}_L}{2} \right) \tag{1.7}$$

The key to regarding time evolution as a quantum computation is to approximate the time evolution operator (1.3) by a product of 2-site-operators, which can be seen as "quantum gates" in analogy to logical gates [4]:

$$\hat{U} \approx \prod_{j=1}^{n} \prod_{i=1}^{L-1} \hat{u}_{i,i+1}^{(j)} \tag{1.8}$$

We need the following relation:

$$e^{-i(\hat{A}+\hat{B})t} = \left[e^{-i(\hat{A}+\hat{B})\frac{t}{n}} \right]^n \tag{1.9}$$

Note that the equality holds exactly even if $\hat{A}$ and $\hat{B}$ are non-commuting objects.

The next step, the Trotter decomposition, is crucial in simulating a quantum system. It is also an approximation step and therefore has to be discussed in the context of an error analysis. Here I will use the 1st order Trotter decomposition to make the algorithmic details clearer. One can Trotter-decompose the expression inside the square brackets of (1.9) by setting $\tau = \frac{t}{n}$, which gives

$$e^{-i(\hat{A}+\hat{B})\tau} = e^{-i\hat{A}\tau}e^{-i\hat{B}\tau} + O(\tau^2) \tag{1.10}$$

This is a good approximation if τ is small enough.

The sum in (1.6) is split into a sum over odd numbered l and into a sum over even numbered l:

$$\hat{H} = \hat{H}_{\text{even}} + \hat{H}_{\text{odd}} \tag{1.11}$$

$$\hat{H}_{\text{even}} = \sum_{l\,\text{even}} \hat{h}_{l,\,l+1} \tag{1.12}$$

$$\hat{H}_{\text{odd}} = \sum_{l\,\text{odd}} \hat{h}_{l,\,l+1} \tag{1.13}$$

While the commutator $[\hat{H}_{\text{even}}, \hat{H}_{\text{odd}}] \neq 0$ does not disappear, the operators in the sum (1.12) are mutually commuting. The same holds for the summands in equation (1.13).

Using the facts given above and the Trotter decomposition (1.10), we can approximate the time evolution operator:

$$\hat{U} = e^{-i\hat{H}t} = e^{-i(\hat{H}_{\text{even}}+\hat{H}_{\text{odd}})t} = \left[e^{-i(\hat{H}_{\text{even}}+\hat{H}_{\text{odd}})\tau}\right]^n \tag{1.14}$$

The Trotter decomposition of the expression in square brackets gives:

$$\begin{aligned} e^{-i(\hat{H}_{\text{even}}+\hat{H}_{\text{odd}})\tau} &= e^{-i\hat{H}_{\text{even}}\tau}e^{-i\hat{H}_{\text{odd}}\tau} + O(\tau^2) \\ &= \prod_{l\,\text{even}} e^{-i\hat{h}_{l,\,l+1}\tau} \prod_{l\,\text{odd}} e^{-i\hat{h}_{l,\,l+1}\tau} + O(\tau^2) \end{aligned} \tag{1.15}$$

Time evolution of a quantum state to time t is achieved by applying the right hand side of equation (1.15) n times on the initial state. The overall error is also $O(\tau^2)$.

In this way the time evolution operator has been decomposed into easy to calculate two-site quantum gates, showing that the approximate simulation of a time evolution is equivalent to simulating a quantum computation. See

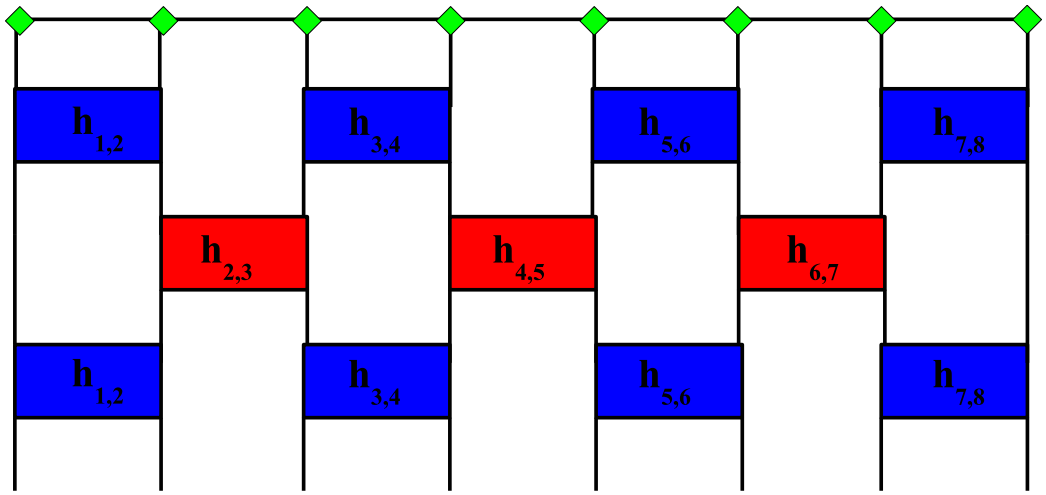

Figure 1.1: The quantum circuit for simulating a time evolution: Alternating application of odd and even numbered two-site quantum gates.

also [4]. The resulting "quantum circuit" with a checkerboard pattern is depicted in figure 1.1.

As it was shown in [5], two-site (two-qubit) gates are universal in the sense that any quantum computation can be performed with two-site gates.

Chapter 2

Quantum Information Theoretical Background

This chapter introduces some basic quantum information theoretical concepts associated with the TEBD algorithm. For algorithmic details knowledge of the Schmidt decomposition is necessary. Section 2.2 introduces entanglement, which is important for the theoretical background of the algorithm. Section 2.3 contains remarks about the notion of entanglement in fermionic and bosonic systems.

2.1 Schmidt Decomposition

A pure state $|\psi\rangle$ of a composite system AB (Fig. 2.1) can be decomposed as follows [6]:

$$|\Psi\rangle = \sum_{\alpha=1}^{\chi} \lambda_\alpha \left|\phi_\alpha^{[A]}\right\rangle \otimes \left|\phi_\alpha^{[B]}\right\rangle \tag{2.1}$$

where the vectors $\{\left|\phi_\alpha^{[A]}\right\rangle\}$ are an orthonormal basis of subsystem A and the vectors $\{\left|\phi_\alpha^{[B]}\right\rangle\}$ are an orthonormal basis of subsystem B. The values λ_α are called the Schmidt-coefficients and are positive. The following condition holds:

$$\sum_{\alpha=1}^{\chi} \lambda_\alpha^2 = 1 \tag{2.2}$$

The Schmidt coefficients are of great importance and by performing a partial trace on $|\psi\rangle\langle\psi|$ one can see that they are the square roots of the

eigenvalues of the reduced density matrices of subsystems A and B. (ρ_A and ρ_B have the same eigenvalues!)

χ is the Schmidt number or *Schmidt rank*, which is the number of non-zero Schmidt coefficients.

The Schmidt decomposition is closely related to the Singular Value Decomposition (SVD) of a matrix:

$$C = UDV^\dagger \tag{2.3}$$

where C is a general (rectangular) m x n matrix, U is a m x m unitary matrix and V is a n x n unitary matrix. D is a m x n matrix with positive values on the diagonal and the other elements equal to zero. These positive values are called the singular values of a matrix.

Let $\{|j\rangle\}$ and $\{|k\rangle\}$ be any orthonormal basis of subsystem A and B respectively. $|\psi\rangle$ can be written as

$$|\psi\rangle = \sum_{j,k} c_{jk} |j\rangle |k\rangle$$

with the elements c_{jk} of a rectangular matrix C. After inserting the SVD of C into the formula above, getting

$$|\psi\rangle = \sum_{\alpha,j,k} u_{j\alpha} d_{\alpha\alpha} v^*_{k\alpha} |j\rangle |k\rangle$$

one can define

$$\begin{aligned} |\phi^{[A]}_\alpha\rangle &= \sum_j u_{j\alpha} |j\rangle \\ |\phi^{[B]}_\alpha\rangle &= \sum_k v^*_{k\alpha} |k\rangle \\ \lambda_\alpha &= d_{\alpha\alpha} \end{aligned}$$

This leads to the Schmidt decomposition (2.1). Relation (2.2) follows from the properties of the reduced density matrices, whose trace is 1.
See also [6].

2.2 Pure State Entanglement

The tensor product structure of the many-body basis and the superposition principle give rise to a distinctive feature of quantum many body systems known as entanglement.

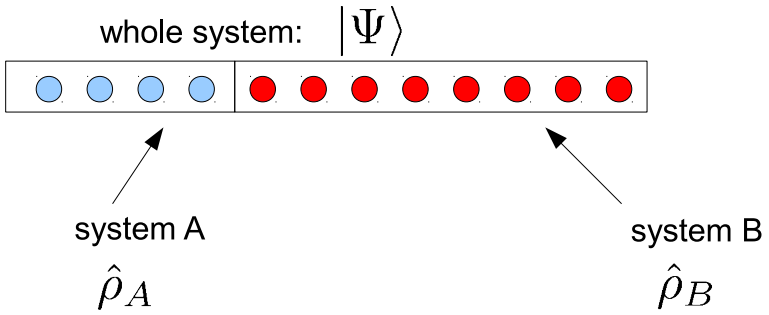

Figure 2.1: 1D chain cut into two parts

A pure state is entangled if and only if it does not factorise into a tensor product:

$$|\Psi\rangle \neq |\text{System A}\rangle \otimes |\text{System B}\rangle \tag{2.4}$$

We then say that System A and System B are entangled. It is useful to quantify the amount of entanglement between two subsystems - the so-called bipartite entanglement.

Therefore one needs entanglement measures which fulfil the following properties [7, 8]:

1. $E(|\Psi\rangle)$ is a map from the Hilbert space of quantum states to positive real numbers: $\mathcal{H} \to \mathbb{R}^+$
2. The entanglement of independent systems is additive: $E(|\Psi_A\rangle \otimes |\Psi_B\rangle) = E(|\Psi_A\rangle) + E(|\Psi_B\rangle)$
3. The entanglement does not change under local and unitary transformations: $E((\hat{U}_A \otimes \hat{U}_B)\,|\Psi\rangle) = E(|\Psi\rangle)$
4. The entanglement does not change on average under local non-unitary operations (e.g. measurements). The local non-unitary operation on $|\Psi\rangle$ yields the states $\{|\Psi_j\rangle\}$ with probabilities $\{p_j\}$. Then for the entanglement $\sum_j p_j E(|\Psi_j\rangle) \leq E(|\Psi\rangle)$ holds.

As a consequence the entanglement can not increase due to local operations and classical communication (LOCC).

One of these entanglement measures is the *von Neumann entropy*, the quantum analogue to the classical Shannon entropy:

$$S(\hat{\rho}) = -\mathrm{tr}\,\hat{\rho}\log\hat{\rho} \tag{2.5}$$

It measures the uncertainty about the quantum state a subsystem is in. A system that is not interacting with its environment can be described by a pure quantum state. The von Neumann entropy is zero only for pure states as there is then no uncertainty about the state the system is in. Often the logarithm to base 2 is used, here I will use the natural logarithm.

Parts of quantum systems are described by the reduced density matrix. Performing the partial trace on a mixed state, we get the state of the subsystem A, where we have no knowledge about subsystem B:

$$\hat{\rho}_A = \mathrm{tr}_B\,\hat{\rho}_{AB} \tag{2.6}$$

Using a complete orthonormal eigensystem $\{|\nu\rangle_B\}$ for system B we can calculate the partial trace:

$$\mathrm{tr}_B\,\hat{\rho}_{AB} = \sum_{\nu} \langle\nu|_B\,\hat{\rho}_{AB}\,|\nu\rangle_B \tag{2.7}$$

In the case of bipartite entanglement and a pure state composite system, we get the entanglement entropy:

$$S = -\mathrm{tr}\,\hat{\rho}_A\log\hat{\rho}_A = -\mathrm{tr}\,\hat{\rho}_B\log\hat{\rho}_B \tag{2.8}$$

Using the Schmidt decomposition and the spectral representation of the reduced density matrix, one sees that the eigenvalues of both reduced density matrices are the same. See also [6, 9].
One can choose any bipartition of the system and use the entanglement entropy (2.8) as an entropy measure $E(|\Psi\rangle)$ for states $|\Psi\rangle$.

The spectral representation of the reduced density matrix reads:

$$S = \sum_{\alpha=1}^{\chi} -\lambda_\alpha^2\log\lambda_\alpha^2 \tag{2.9}$$

λ_α^2 are the eigenvalues of the reduced density matrix. By building the reduced density matrix from the Schmidt decomposition, we see that the eigenvalues are just the Schmidt coefficients squared.

The expression above is maximal for equal eigenvalues. Together with relation (2.2) the following upper bound for the entanglement entropy follows:

$$E_\chi = \log\chi \tag{2.10}$$

where χ is the Schmidt rank, which is the number of non-zero Schmidt coefficients. One can show that E_χ is also an entanglement measure, which shows that the Schmidt rank also gives information about the amount of entanglement.

Instead of using a specific bipartition of the system to measure the entanglement of the whole state, one could set $\chi = \max \chi_i$, where the $\{\chi_i\}$ are the Schmidt numbers of all possible Schmidt decompositions of a system. In the following it will be sufficient to just look at the bipartitions that result from cutting the chain at each bond into two parts. [4, 1]

2.3 Entanglement of Fermionic and Bosonic Systems

While it is most convenient to develop the underlying theory for spin systems, where the Hilbert space's tensor product structure in configuration space (lattice) and partition in subsystems is obvious, fermionic and bosonic systems deserve some remarks. These concern the definition of entanglement for indistinguishable particles. In the following paragraphs only spinless fermions are considered for the sake of simplicity.

For fermionic systems bases of properly antisymmetrised tensor products of single particle states are used. If $H_L(N)$ is the Hilbert space for a N-particle state, the Fock space $\mathcal{H}_L$ is the direct sum from $H_L(0)$ to $H_L(L)$, where L is the lattice size (at most L fermions are allowed in the system due to the Pauli-principle).

$$\mathcal{H}_L = \bigoplus_i^L H_L(i) \tag{2.11}$$

The Fock (basis) states are usually given in the occupation number representation and can be encoded as binary numbers. It is easy to see that there exists a map between each Fock state to just one of the L-fold tensor products of 2-state-subsystems states. E.g.: $|010\rangle \rightarrow |0\rangle \otimes |1\rangle \otimes |0\rangle$. This means nothing else that the local Hilbert space has dimension 2. More formally: There exists an isomorphism (not unique) between the Fock space of a L-site spinless fermion system and a system of L spin-1/2.

The Fock states are considered unentangled in this picture, although they are in general non-separable superpositions of tensor products of single-particle states. The notion of entanglement depends on what we consider as the quantum mechanical subsystems a larger system is composed of (entanglement relativity) [10].

In the case of spinless fermions on a lattice we can measure whether a site is occupied by a particle or not, whereas the single particle states are not accessible due to indistinguishability.

This operational argument lets us pick the right subsystems and therefore the type of entanglement and all requirements about entanglement made for matrix product state algorithms stay valid.

The generalisation to spinful fermions is straightforward and for bosons, where the number of particles at one site is in principle unlimited, one can use the isomorphism $\mathcal{H}_L \rightarrow h_\infty^{\otimes L}$, where h_∞ is for example the harmonic oscillator state space with elements $|0\rangle$, $|1\rangle$, $|2\rangle$, ... In practical simulations however the number of bosons per site has to be limited to a certain number and the local Hilbert space has finite dimension.
See also [11].

Chapter 3

Matrix Product States

In this section I will give a summary of a very favourable representation of quantum states for physically interesting 1D quantum systems - the Matrix Product State (MPS) formalism. After the development of the Density Matrix Renormalisation Group method (DMRG), a lot of interest was drawn to explaining the success of this method. It was pointed out by Östlund and Rommer [12, 13] that DMRG in fact creates a matrix product state, which were first introduced in a different context as valence bond states (see AKLT-state). Matrix product states are sometimes called finitely correlated states. Introductions to matrix product states can be found in [14, 8, 15, 16, 9]. A different representation, the canonical normal form, is presented in [1] and discussed in section 3.2. The canonical normal form is derived using the Schmidt decomposition (2.1) and gives insights into the quantum information theoretical background of matrix product states.

3.1 Construction of a Matrix Product State

The main problem in simulating quantum systems is the exponential growth of the corresponding Hilbert space dimension. Suppose that $\{|m_{l-1}\rangle\}$ is a set of basis vectors for a $(l-1)$-site Hilbert space with dimension M. Then the vectors $|m_{l-1}\rangle \otimes |s_l\rangle$, where $|s_l\rangle$ are orthonormal basis vectors of a one site subsystem, are a basis of a l-site system. Thus we have added one additional site to the system, but the number of basis states has increased to dM, where d is the dimension of the local Hilbert space. Performing a general basis transformation one gets:

$$|m_l\rangle = \sum_{(m_{l-1},s_l)} U_{m_l,(m_{l-1},s_l)} \, |m_{l-1}\rangle \otimes |s_l\rangle \tag{3.1}$$

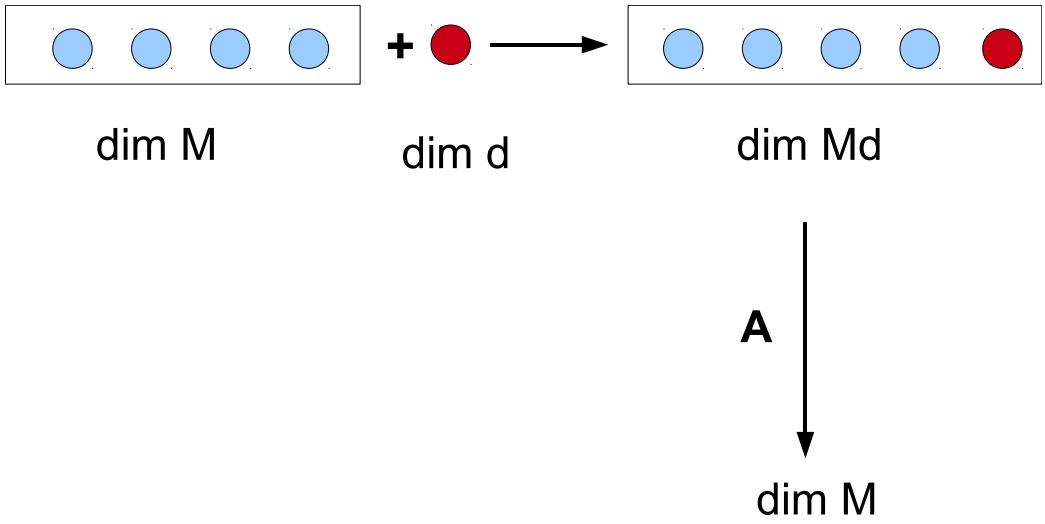

Figure 3.1: Hilbert space truncation

The object U is a matrix where the second index is a composite index. If we demand that $\{|m_{l-1}\rangle\}$ and $\{|m_l\rangle\}$ are orthonormal sets of basis vectors, we have to impose the following (unitarity) constraint: $UU^\dagger = 1$

What remains is the problem that by adding one site the Hilbert space dimension has grown d times, so the basis transformation is combined with a Hilbert space truncation. This is achieved by making the matrix U rectangular. A $M \times dM$ transformation matrix keeps the Hilbert space dimension fixed at M. (Fig. 3.1)

The main idea of the Matrix Product State (MPS) approach is to find a suitable combination of basis transformations and truncations, such that a specific state of the l-site system is still faithfully represented by a Hilbert space with dimension M.

In MPS literature the notation is somewhat different and the transformation is written as:

$$|m_l\rangle = \sum_{s_l}^{d} \sum_{m_{l-1}}^{M} A^{s_l\,[l]}_{m_l, m_{l-1}} |m_{l-1}\rangle \otimes |s_l\rangle \tag{3.2}$$

Here we use a third index s_l (superscript) instead of the composite index in U. This index is called the *physical index*, whereas m_l and m_{l-1} are called *virtual indices*. I will adopt the common practise of writing the virtual indices with Greek letters in some of the following sections. Additionally a site index $[l]$ in square brackets is written with the transformation matrix A.

See also [16].

The orthonormality condition mentioned above now translates to:

$$\sum_{s_l} A^{s_l[l]} (A^{s_l[l]})^\dagger = 1$$

Further discussion of orthonormality conditions is in section 3.2.3.

Starting with a single site system and by iterating the procedure of first adding one site, then transforming the basis and truncating the Hilbert space, one gets a matrix product state representation:

$$|\Psi\rangle = \sum_{\{s_1,s_2,\ldots,s_L\}} A^{s_1[1]} A^{s_2[2]} A^{s_3[3]} \ldots A^{s_L[L]} |s_1\rangle \otimes |s_2\rangle \ldots \otimes |s_L\rangle \tag{3.3}$$

$$|\Psi\rangle = \sum_{\{s_1,s_2,\ldots,s_L\}} c_{s_1,s_2,\ldots,s_L} |s_1\rangle \otimes |s_2\rangle \ldots \otimes |s_L\rangle \tag{3.4}$$

Comparing this to the general expansion of a quantum state in a many-body basis (3.4) one notices that the d^L coefficients are replaced by $d * L$ matrices with dimension M.

It is convenient to visualise this expression in graphical form [14]. A MPS matrix is represented by a three-legged object as given in the upper left corner of figure 3.2. The vertical leg corresponds to the physical index, whereas the horizontal legs correspond to the virtual indices. For *open boundary conditions* we have matrices with just one physical index at the edges, given by the object in the upper right corner. If we connect two legs of MPS matrices, we have to perform a tensor contraction - that is a summation over a common index as shown in the bottom of figure 3.2. Unconnected legs remain as indices. In this fashion we can represent the matrix product state coefficients as in Fig. 3.3

The next expression (3.5), which is used for periodic boundary conditions is a generalisation of the matrix product state representation above. On the edges one can use general matrices and the trace operation ensures that the coefficients are scalar:

$$|\Psi\rangle = \sum_{\{s_1,s_2,\ldots,s_L\}} \mathrm{tr}\, A^{s_1[1]} A^{s_2[2]} A^{s_3[3]} \ldots A^{s_L[L]} |s_1\rangle \otimes |s_2\rangle \ldots \otimes |s_L\rangle \tag{3.5}$$

A matrix product state representation is not unique since one can always insert a resolution of the identity operator between two neighboring matrices:

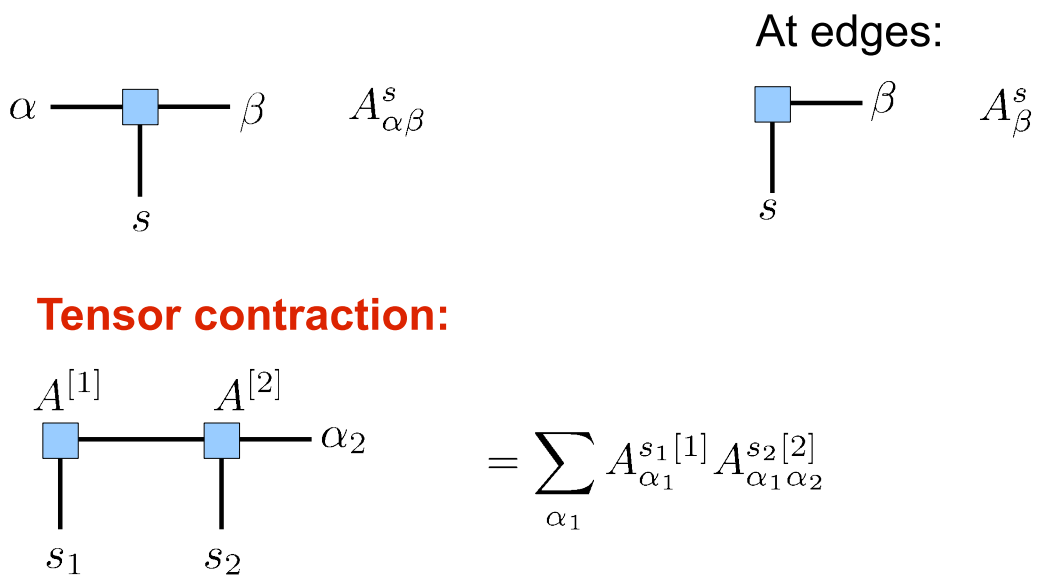

Figure 3.2: Graphical representation of MPS matrices, tensor contraction

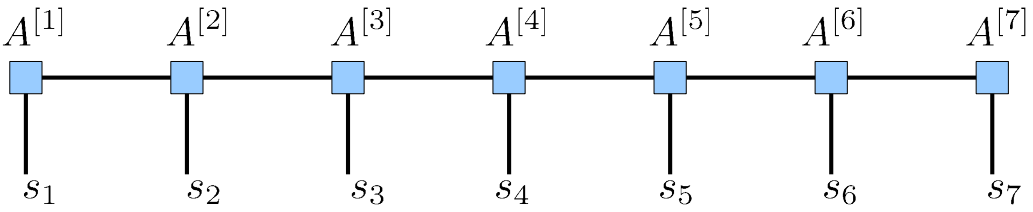

Figure 3.3: Graphical representation of MPS coefficients

$$A^{s_l[l]}A^{s_{l+1}[l+1]} = A^{s_l[l]}\underbrace{X^{-1}X}_{\mathbb{1}}A^{s_{l+1}[l+1]} = \tilde{A}^{s_l[l]}\tilde{A}^{s_{l+1}[l+1]} \tag{3.6}$$

$$A^{s_l[l]}X^{-1} =: \tilde{A}^{s_l[l]}$$

$$XA^{s_{l+1}[l+1]} =: \tilde{A}^{s_{l+1}[l+1]}$$

Now the non-singular matrix X is often choosen such that certain orthonormality constraints are fulfilled. (see section 3.2.3)

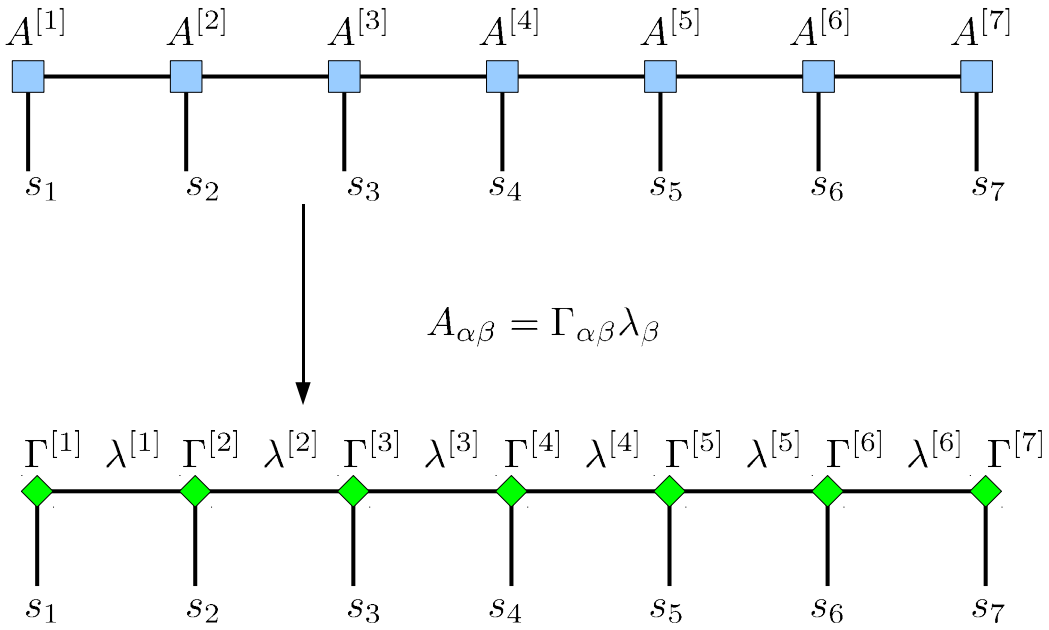

Figure 3.4: Canonical normal form of a MPS for use in the TEBD algorithm

3.2 Canonical Normal Form

If one chooses as orthonormal basis sets $\{|m_{l-1}\rangle\}$ and $\{|m_l\rangle\}$ in (3.2) the Schmidt basis sets from Schmidt decompositions at every bond, one obtains another MPS representation - the canonical normal form.

This representation is used for the TEBD algorithm and moreover shows the connection between the entanglement of a state and the matrix dimension M needed in a MPS.

Instead of using the A-matrices, the Schmidt coefficients of every Schmidt decomposition are explicitely introduced into the representation by setting $A^{k[l]}_{\alpha\beta} = \Gamma^{k[l]}_{\alpha\beta}\,\lambda^{[l]}_\beta$.

The canonical normal form then reads:

$$|\Psi\rangle = \sum_{\substack{\{s_1,s_2,\ldots,s_L\}\\ \{\alpha_1,\alpha_2,\ldots,\alpha_{L-1}\}}} \Gamma^{s_1[1]}_{\alpha_1}\lambda^{[1]}_{\alpha_1}\Gamma^{s_2[2]}_{\alpha_1\alpha_2}\lambda^{[2]}_{\alpha_2}\ldots\lambda^{[L-1]}_{\alpha_{L-1}}\Gamma^{s_L[L]}_{\alpha_{L-1}}\,|s_1 s_2 \ldots s_L\rangle \qquad (3.7)$$

3.2.1 Derivation of the Canonical Normal Form

The canonical normal form, which assumes open boundary conditions, is derived by repeated Schmidt-decompositions of an 1D system's state [1]:

Looking at the Schmidt-decomposition at bond 1:

$$|\Psi\rangle = \sum_{\alpha_1}^{\chi_1} \lambda_{\alpha_1}^{[1]} \left|\Phi_{\alpha_1}^{[1]}\right\rangle \otimes \left|\Phi_{\alpha_1}^{[2\ldots L]}\right\rangle \tag{3.8}$$

We write the basis vectors $\left\{|\Phi_{\alpha_1}^{[1]}\rangle\right\}$ as:

$$\left|\Phi_{\alpha_1}^{[1]}\right\rangle = \sum_{s_1}^{d_1} \Gamma_{\alpha_1}^{s_1[1]} |s_1\rangle \tag{3.9}$$

arriving at:

$$|\Psi\rangle = \sum_{s_1}^{d_1} \sum_{\alpha_1}^{\chi_1} \Gamma_{\alpha_1}^{s_1[1]} \lambda_{\alpha_1}^{[1]} |s_1\rangle \otimes |\Phi_{\alpha_1}^{[2\ldots L]}\rangle \tag{3.10}$$

The basis vectors $\left\{|\Phi_{\alpha_1}^{[2\ldots L]}\rangle\right\}$ on the other hand are written as:

$$\left|\Phi_{\alpha_1}^{[2\ldots L]}\right\rangle = \sum_{s_2}^{d_2} |s_2\rangle \otimes |\tau_{\alpha_1,s_2}^{[3\ldots L]}\rangle \tag{3.11}$$

where $|\tau_{s_1}\rangle$ are unnormalised vectors.

These vectors are expanded in the right hand side basis of the Schmidt decomposition at the next bond (bond 2), using transformation matrices A as in (3.2):

$$|\tau_{\alpha_1,s_2}^{[3\ldots L]}\rangle = \sum_{\alpha_2}^{\chi_2} A_{\alpha_1\alpha_2}^{s_2[2]} |\Phi_{\alpha_2}^{[3\ldots L]}\rangle \tag{3.12}$$

We define the matrices Γ to introduce the Schmidt coefficients into the representation:

$$\Gamma_{\alpha\beta}^{k[l]} \lambda_{\beta}^{[l]} := A_{\alpha\beta}^{k[l]} \tag{3.13}$$

We get:

$$|\tau_{\alpha_1,s_2}^{[3\ldots L]}\rangle = \sum_{\alpha_2}^{\chi_2} \Gamma_{\alpha_1\alpha_2}^{s_2[2]} \lambda_{\alpha_2}^{[2]} |\Phi_{\alpha_2}^{[3\ldots L]}\rangle \tag{3.14}$$

The result of this basis transformation is:

$$|\Psi\rangle = \sum_{s_1}^{d_1} \sum_{s_2}^{d_2} \sum_{\alpha_1}^{\chi_1} \sum_{\alpha_2}^{\chi_2} \Gamma_{\alpha_1}^{s_1[1]} \lambda_{\alpha_1}^{[1]} \Gamma_{\alpha_1\alpha_2}^{s_2[2]} \lambda_{\alpha_2}^{[2]} |s_1\rangle \otimes |s_2\rangle \otimes |\Phi_{\alpha_2}^{[3\ldots L]}\rangle \tag{3.15}$$

For bond l the previous step (transformation from Schmidt basis to computational basis) reads:

$$\left|\Phi^{[l\ldots L]}_{\alpha_{l-1}}\right\rangle = \sum_{s_l} |s_l\rangle \otimes |\tau^{[l+1\ldots L]}_{\alpha_{l-1},s_l}\rangle \tag{3.16}$$

$$|\tau^{[l+1\ldots L]}_{\alpha_{l-1},s_l}\rangle = \sum_{\alpha_l} \Gamma^{[l]s_l}_{\alpha_{l-1}\alpha_l} \lambda^{[l]}_{\alpha_l} |\Phi^{[l+1\ldots L]}_{\alpha_l}\rangle \tag{3.17}$$

Iterating these steps gives:

$$|\Psi\rangle = \sum_{\substack{\{s_1,s_2,\\ \ldots,s_L\}}} \left(\sum_{\alpha_1}^{\chi_1} \ldots \sum_{\alpha_{L-1}}^{\chi_{L-1}} \Gamma^{s_1[1]}_{\alpha_1} \lambda^{[1]}_{\alpha_1} \Gamma^{s_2[2]}_{\alpha_1\alpha_2} \lambda^{[2]}_{\alpha_2} \ldots \lambda^{[L-1]}_{\alpha_{L-1}} \Gamma^{s_L[L]}_{\alpha_{L-1}} \right) |s_1 s_2 \ldots s_L\rangle \tag{3.18}$$

This is an *exact* representation of the state, provided that always the full Schmidt ranks χ_l are taken into account. We can rewrite the formula by letting the summations over the virtual indices α_l run to a common number $\chi = \max_l \chi_l$. As we have seen in section 2.2, the maximum Schmidt rank χ can be used for the entanglement measure E_χ of the state $|\Psi\rangle$ using (2.10).

From the Schmidt decomposition we know that χ can be as large as $d^{\lfloor L/2 \rfloor}$ (for site-independent local Hilbert space dimension), which is usually too large for practical purposes. Therefore one restricts the summation to a maximal index $M \leq \chi$ and gets the canonical normal form (3.7). We identify M as the matrix dimension of a matrix product state. This is the main result that links quantum information theory with simulations that use matrix product states.

> **Conclusion.** A quantum state is exactly represented by a matrix product state with matrix dimension $M = \chi$, where χ is the maximal Schmidt number of all Schmidt decompositions of the form $[1, 2, 3, \ldots, l] : [l + 1, l + 2, \ldots, L]$.

3.2.2 Graphical Representation

In a graphical representation (Fig. 3.4) we write the Schmidt coefficients at the respective bonds and it is then easy to read off Schmidt decompositions and MPS-representations of Schmidt vectors.

Figure 3.5 shows how to get the Schmidt decomposition from the graphical representation of the canonical normal form: By tensor contracting what

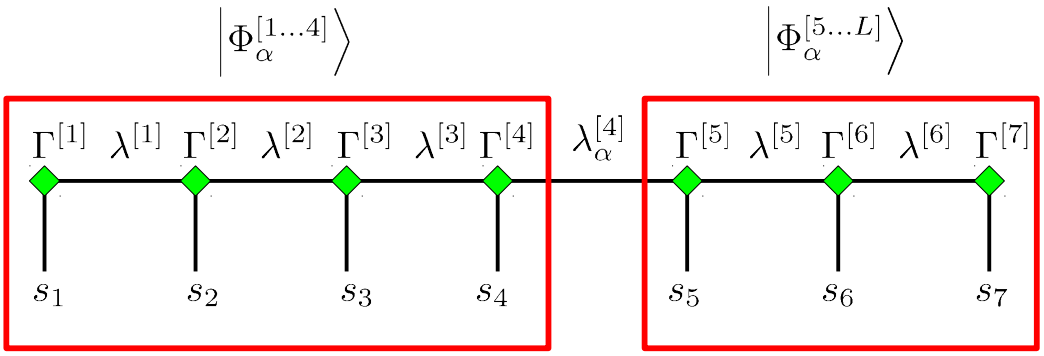

Figure 3.5: Getting the Schmidt decomposition from the canonical normal form

is in the left box we get the left Schmidt basis vectors. Note that there is one unconnected horizontal leg which corresponds to the index α of the basis vectors. Similarly we get the right Schmidt basis vectors (or rather their expansion coefficients) by contracting the contents of the right box.

3.2.3 Orthonormality Constraints

Similar to above a state representation of block - single site - block can be read off from the graphical scheme:

$$|\Psi\rangle = \sum_{\alpha\beta}\sum_{k} \lambda_\alpha^{[l-1]}\ \Gamma_{\alpha\beta}^{k[l]}\ \lambda_\beta^{[l]}\ |\Phi_\alpha^{[1\ldots l-1]}\rangle \otimes |k\rangle \otimes |\Phi_\beta^{[l+1\ldots L]}\rangle \tag{3.19}$$

Using (3.13) we can write (3.19) as:

$$|\Psi\rangle = \sum_{\alpha} \lambda_\alpha^{[l-1]}\ |\Phi_\alpha^{[1\ldots l-1]}\rangle \otimes \left(\sum_{k\beta} A_{\alpha\beta}^{k[l]}\ |k\rangle \otimes |\Phi_\beta^{[l+1\ldots L]}\rangle\right) \tag{3.20}$$

By comparing this expression with the Schmidt decomposition one can identify the expression in round brackets with the right Schmidt basis vectors $|\Phi_\alpha^{[l\ldots L]}\rangle$. Suppose that the vectors $|\Phi_\beta^{[l+1\ldots L]}\rangle$ are already orthonormal. If we demand that also the basis vectors $|\Phi_\alpha^{[l\ldots L]}\rangle$ were orthonormal, then the following orthonormality constraint on the matrices $A^{k[l]}$ must hold:

$$\sum_k A^{k[l]} A^{k[l]\dagger} = \mathbb{1} \tag{3.21}$$

Since this is the condition for orthonormal basis sets to the *right* of site l, this is the so-called *right-handed* orthonormality constraint.

Similarly we can find a left-handed orthonormality constraint using the definition

$$B^{k[l]}_{\alpha\beta} := \lambda^{[l-1]}_{\alpha}\Gamma^{k[l]}_{\alpha\beta} \tag{3.22}$$

one can write (3.19) as

$$|\Psi\rangle = \sum_{\beta} \lambda^{[l]}_{\beta} \left(\sum_{\alpha k} B^{k[l]}_{\alpha\beta} \, |\Phi^{[1\ldots l-1]}_{\alpha}\rangle \otimes |k\rangle \right) \otimes |\Phi^{[l+1\ldots L]}_{\beta}\rangle \tag{3.23}$$

Arguments analogous to above give the *left-handed* orthonormality constraint:

$$\sum_{k} B^{k[l]\dagger} B^{k[l]} = \mathbb{1} \tag{3.24}$$

These orthonormality constraints are often used in the MPS context and are not restricted to the canonical normal form.

We have also seen that for the canonical normal form the orthonormality constraint fulfilled depends on the use of either (3.13) or (3.22).

3.3 Efficient Representation of Quantum States

For certain classes of quantum states MPS are an efficient representation in the sense that memory requirements grow slowly with system size (at best linearly). Some examples are:

1. Simple tensor products/Fock states: $|s_1\rangle \otimes |s_2\rangle \otimes |s_3\rangle \otimes \ldots \otimes |s_L\rangle$ $(M = 1)$

$$A^{s'_l[l]} = \delta_{s'_l, s_l} \tag{3.25}$$

2. GHZ state (Greenberger-Horne-Zeilinger state): $\frac{1}{\sqrt{2}}(|000\ldots\rangle + |111\ldots\rangle)$ $(M = 2)$

$$A^{0[l]} = 2^{-\frac{1}{2L}} \begin{pmatrix} 1 & 0 \\ 0 & 0 \end{pmatrix} \quad A^{1[l]} = 2^{-\frac{1}{2L}} \begin{pmatrix} 0 & 0 \\ 0 & 1 \end{pmatrix}$$

3. AKLT state ($M = 2$): Exact solution for the ground state of a certain spin-1 Hamiltonian with quadratic spin-spin interaction:

$$\hat{H} = \sum_{\langle i,j \rangle} \left(\vec{\hat{S}}_i \cdot \vec{\hat{S}}_j + \frac{1}{3} \left(\vec{\hat{S}}_i \cdot \vec{\hat{S}}_j \right)^2 + \frac{2}{3} \right)$$

[14]

4. Ground states of 1D spin systems for Hamiltonians with local interactions

The last group of states deserves further discussion:

3.3.1 Area Laws

For ground states of spin systems whose Hamiltonians include only local interactions entropy scaling relations suggest that the entanglement in these states is sufficiently restricted. The connection between the entanglement and the matrix dimension M of a MPS (section 3.2.1) then suggests that M is also restricted.

The entanglement entropy of a block of spins embedded in an infinite-size system with linear dimension L scales as:

$$S \sim L^{D-1} \tag{3.26}$$

D is the dimension. This means that the quantum entanglement entropy is not an extensive quantity but rather scales like the surface of the block of spins. In one dimension the surface consists only of two points and the entropy approaches a constant value. (Fig. 3.6)

$$S \sim \text{const.} \tag{3.27}$$

For critical 1D systems a logarithmic correction has to be made:

$$S \sim \log L \tag{3.28}$$

[14]

From (2.10) follows that $\chi \geq e^S$. In the non-critical one dimensional case this means that χ is greater than a value independent of the system size. Numerical results suggest that χ and e^S are approximately proportional. [16] Therefore such a state is efficiently represented by a matrix product state with fixed matrix dimension $M \simeq \chi$. In higher dimensions we see that

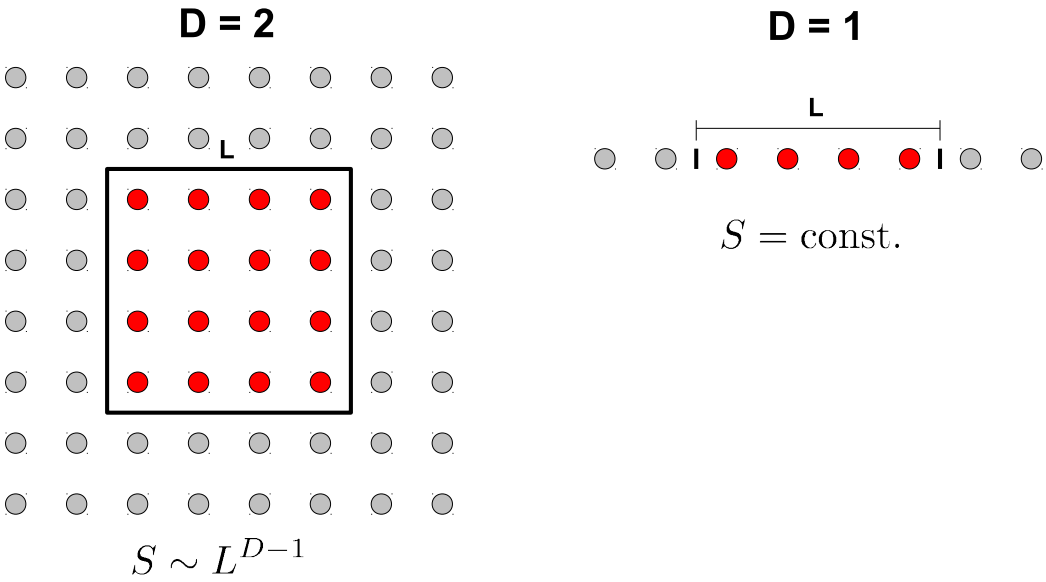

Figure 3.6: Entropy scaling for ground states of local Hamiltonians

χ has to grow exponentially with system size which limits the use of MPS methods and the related DMRG to small systems.

Time evolution algorithms using matrix product states assume that the time evolving quantum state (starting from a perturbed ground state) is well represented by a MPS with fixed M.

3.4 Matrix Product State Calculations

Having an efficient representation for quantum states would not be of much use if there was not also an efficient way to evaluate expectation values, correlators, overlaps...

This calculations usually require the application of one-site operators on a matrix product state, which changes the matrix for the respective site:

$$\hat{V}^{[l]} = \sum_{i_l, j_l} V_{i_l, j_l} \left| i_l \right\rangle \left\langle j_l \right| \tag{3.29}$$

$$A'^{\,i_l[l]}_{\alpha\beta} = \sum_{j_l} V_{i_l, j_l} A^{j_l[l]}_{\alpha\beta} \tag{3.30}$$

Here $\hat{V}^{[l]}$ is an operator that acts only on site l. $A'^{\,i_l[l]}$ are the new matrices after the operator application. This follows from applying the operator (3.29) on (3.3).

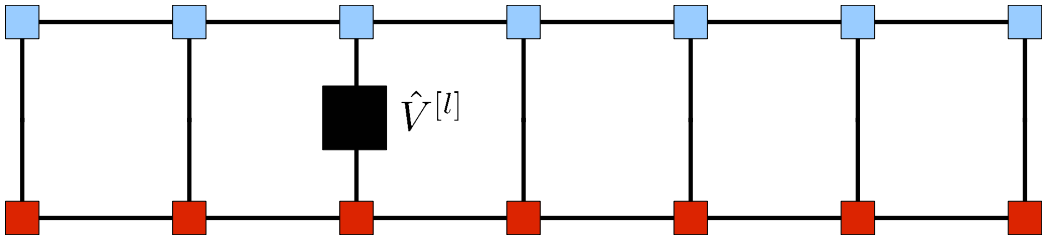

Figure 3.7: Calculation of matrix elements of single-site operator products: $\left\langle \phi \middle| \hat{V}^{[l]} \dots \middle| \Psi \right\rangle$

Figure 3.7 shows the calculation of $\left\langle \phi \middle| \hat{V}^{[1]} \hat{V}^{[2]} \dots \hat{V}^{[L]} \middle| \Psi \right\rangle$ for open boundary conditions. Such a product of operators sandwiched between two state vectors can be specialised to expectation values, correlation functions and an overlap calculation by setting the appropriate operators equal to the identity. For the sake of simplicity only one operator application on $|\Psi\rangle$ is depicted in the figure. We assume that the all of the operators act on just one site, therefore the operator application on $|\Psi\rangle$ is calculated using (3.29).

It is important how one performs this tensor contraction: Starting at e.g. the left edge, building a two-index object and then building up the contraction site by site reduces the computational cost to $O(M^3)$. [14] If one did not start the contraction at the edge, the computational cost would be one order of magnitude higher.

Figure 3.8 depicts the faster full tensor contraction strategy. Suppose that all the operators have been applied to $|\Psi\rangle$, yielding a state whose MPS-representation is given by the matrices $A^{[l]}$. The matrix product state $|\phi\rangle$ is represented by the matrices $C^{[l]}$. Starting the contraction at the left edge, one gets the matrix $M^{[1]}$:

$$M^{[1]}_{\alpha_1\beta_1} = \sum_{s_1} A^{s_1[1]}_{\alpha_1} \left(C^{s_1[1]}_{\beta_1}\right)^* \tag{3.31}$$

If we proceed to the next site, we get the matrix $M^{[2]}$ (see also figure 3.8):

$$M^{[2]}_{\alpha_2\beta_2} = \sum_{s_2} \sum_{\alpha_1,\beta_1} M^{[1]}_{\alpha_1\beta_1} A^{s_2[2]}_{\alpha_1\alpha_2} \left(C^{s_2[2]}_{\beta_1\beta_2}\right)^* \tag{3.32}$$

This procedure is iterated until the final result $M^{[L]} = \left\langle \phi \middle| \hat{V}^{[1]} \hat{V}^{[2]} \dots \hat{V}^{[L]} \middle| \Psi \right\rangle$ is obtained, which is a scalar value. In matrix notation the iteration reads:

$$M^{[l]} = \sum_{s_l} \left(A^{s_l[l]}\right)^T M^{[l-1]} \left(C^{s_l[l]}\right)^* \tag{3.33}$$

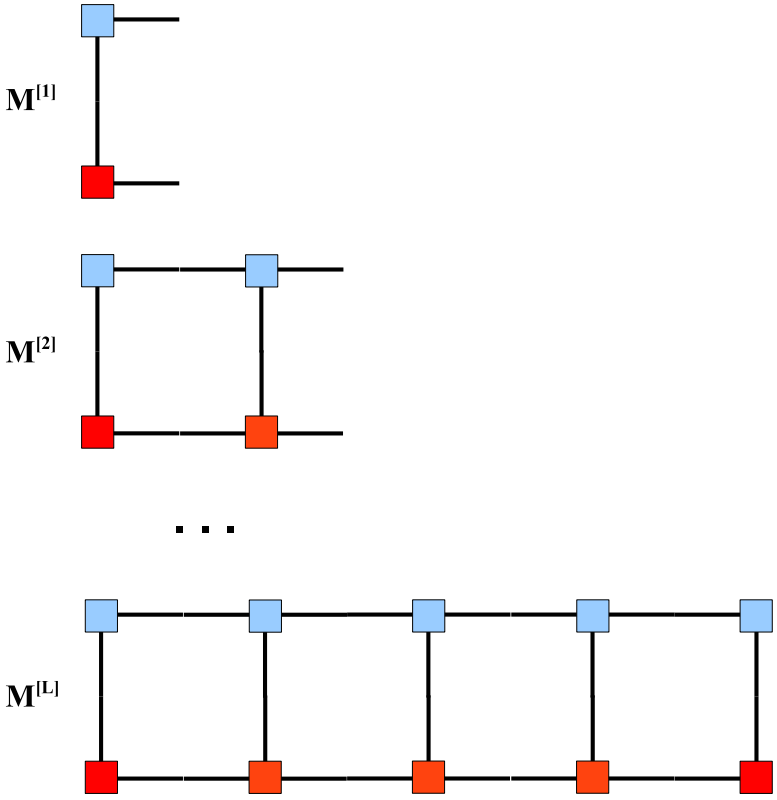

Figure 3.8: Faster tensor contraction strategy for open boundary conditions

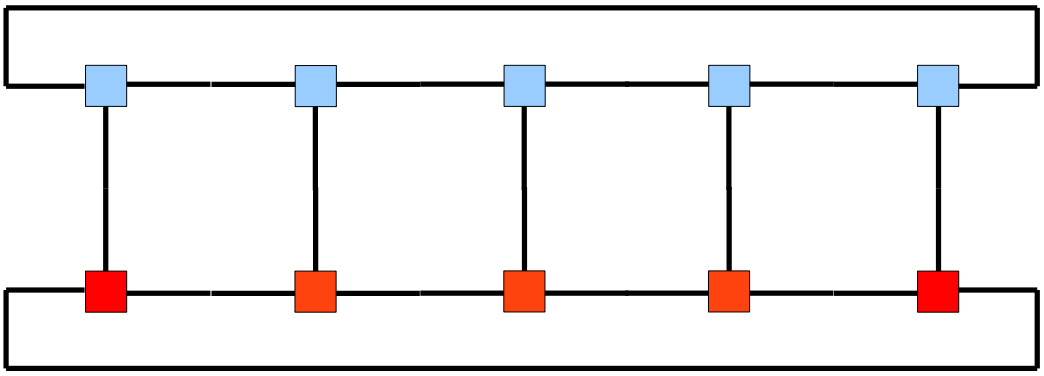

Figure 3.9: Full tensor contraction for periodic boundary conditions.

Note that this is only valid for open boundary conditions. Figure 3.9 shows the situation for periodic boundary conditions, where two additional contraction over the outer legs are necessary. Then the full tensor contraction scales as $O(M^5)$, which is of higher order than MPS methods which scale as $O(M^3)$. However approximate calculations of $O(M^3)$ are possible [15, 17].

Using the orthonormality constraints for the canonical normal form (section 3.2.3), the calculation of expectation values of single site operators simplifies:

$$\left\langle \Psi \middle| \hat{V}^{[l]} \middle| \Psi \right\rangle = \sum_{\alpha} \sum_{\beta} \sum_{k} \left(\lambda_{\alpha}^{[l-1]}\right)^2 \left(\Gamma_{\alpha\beta}^{k[l]}\right)^* \Gamma'^{\,k[l]}_{\alpha\beta} \left(\lambda_{\beta}^{[l]}\right)^2 \tag{3.34}$$

where

$$\begin{aligned} \Gamma'^{\,i_l[l]}_{\alpha\beta} &= \sum_{j_l} V_{i_l,j_l} \Gamma_{\alpha\beta}^{j_l[l]} \\ \hat{V}^{[l]} &= \sum_{i_l,j_l} V_{i_l,j_l} \left|i_l\right\rangle \left\langle j_l\right| \end{aligned} \tag{3.35}$$

This can be generalised to the calculation of $\left\langle \Psi \middle| \hat{V}^{[l]} \hat{V}^{[l+1]} \ldots \hat{V}^{[m]} \middle| \Psi \right\rangle$, where because of the orthonormality conditions the contraction has to be performed only from site l to site m.

For two-site operator expectation values a simplified formula is

$$\left\langle \Psi \middle| \hat{V}^{[l,l+1]} \middle| \Psi \right\rangle = \sum_{\alpha k \ell \gamma} (\Theta_{\alpha k,\ell\gamma})^* \Theta'_{\alpha k,\ell\gamma} \tag{3.36}$$

The object Θ' is calculated from (4.4). Θ is calculated by setting $\hat{V} = \mathbb{1}$ in the same expression.

An example where two-site operator expectation values are useful is the calculation of the energy expectation value using (1.6):

$$\langle E \rangle = \left\langle \Psi \middle| \hat{H} \middle| \Psi \right\rangle = \sum_{l=1}^{L-1} \left\langle \Psi \middle| \hat{h}_{l,l+1} \middle| \Psi \right\rangle \tag{3.37}$$

Dynamical correlations of the form $\left\langle \Psi_0 \middle| \hat{A}(t)\, \hat{B}(0) \middle| \Psi_0 \right\rangle$, where $|\Psi_0\rangle$ is the ground state with energy E_0, are calculatable using a time evolution algorithm such as the one presented in chapter 4.

$$\begin{aligned} \left\langle \Psi_0 \middle| \hat{A}(t)\, \hat{B}(0) \middle| \Psi_0 \right\rangle &= \left\langle \Psi_0 \middle| e^{i\hat{H}t}\, \hat{A}\, e^{-i\hat{H}t}\, \hat{B} \middle| \Psi_0 \right\rangle = \\ &= \left\langle \Psi_0 \middle| e^{i\hat{H}t}\, \hat{A}\; e^{-i\hat{H}t} \middle| \phi(0) \right\rangle = e^{iE_0 t} \left\langle \Psi_0 \middle| \hat{A} \middle| \phi(t) \right\rangle \end{aligned} \tag{3.38}$$

In the last line we have defined $|\phi(0)\rangle := \hat{B}\,|\Psi_0\rangle$. $|\phi(t)\rangle$ is then the time evolved state of $|\phi(0)\rangle$. We see that at each t, we are interested in, a calculation of one operator sandwiched between two different states is necessary. These calculations have just been described above.

Chapter 4

Time Evolving Block Decimation

The simulation of the real time evolution is possible by applying the product of two-site gates given in expression (1.15) on an initial quantum state with known MPS representation. This leads to the time evolving block decimation algorithm (TEBD). [18, 1] describe the two-site gate application in detail. The TEBD algorithm can be optimised by taking into account conserved additive quantum numbers (section 4.1.3).

Errors are introduced by the Trotter decomposition and the Hilbert space truncation. An evolution in imaginary time is useful to calculate ground state approximations. Eventually an implementation of the algorithm is presented and related methods are listed.

4.1 Two-site Quantum Gates

To learn how to apply a two-site gate/operator on a matrix product state, we look at the Schmidt decomposition of the quantum state that we get after applying the operator:

$$|\Psi'\rangle = \sum_{\beta} \lambda_{\beta}^{\prime[l]} \left|{\Phi'}_{\beta}^{[1\ldots l]}\right\rangle \left|{\Phi'}_{\beta}^{[l+1\ldots L]}\right\rangle \tag{4.1}$$

The two-site operator $\hat{V}$ expanded in a two-site basis reads:

$$\hat{V} = \sum_{ij} \sum_{k\ell} V_{k\ell,ij} \, |k\ell\rangle \, \langle ij| \tag{4.2}$$

The state $|\Psi'\rangle$ after the application of the two site operator can be expanded in the following basis: left block - site - site - right block (in DMRG

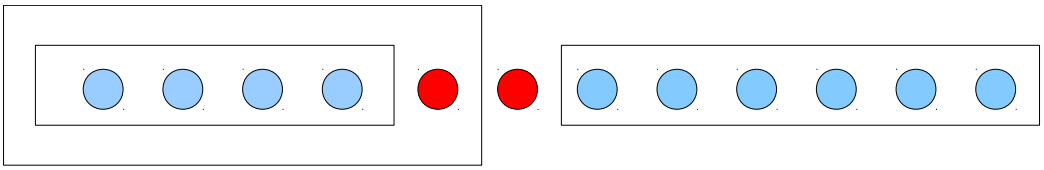

Figure 4.1: TEBD block configuration

a S••E configuration, Fig. 4.1) with the coefficients $\Theta_{\alpha k,\ell\gamma}$ which form a four-index tensor. Here $\{|\alpha\rangle\}$ denote orthonormal (Schmidt) basis vectors of the left block, $\{|k\rangle\}$ and $\{|\ell\rangle\}$ are single site basis vectors and $\{|\gamma\rangle\}$ are basis vectors of the right block.

The expansion reads:

$$|\Psi'\rangle = \hat{V}\,|\Psi\rangle = \sum_{\alpha k\ell\gamma} \Theta_{\alpha k,\ell\gamma}\,|\alpha\rangle \otimes |k\rangle \otimes |\ell\rangle \otimes |\gamma\rangle \tag{4.3}$$

where the coefficient tensor is given by

$$\Theta_{\alpha k,\ell\gamma} := \sum_{\beta}^{M} \sum_{i}^{d} \sum_{j}^{d} V_{k\ell,ij} \lambda_{\alpha}^{[l-1]} \Gamma_{\alpha\beta}^{i[l]} \lambda_{\beta}^{[l]} \Gamma_{\beta\gamma}^{j[l+1]} \lambda_{\gamma}^{[l+1]} \tag{4.4}$$

The density matrix of the pure state is

$$\hat{\rho} = |\Psi'\rangle\langle\Psi'| = \sum_{\alpha' k'\ell'\gamma'} \sum_{\alpha k\ell\gamma} \Theta^{*}_{\alpha' k',\ell'\gamma'} \Theta_{\alpha k,\ell\gamma}\,|\alpha' k'\ell'\gamma'\rangle\langle\alpha k\ell\gamma| \tag{4.5}$$

By tracing out the subsystem consisting of the left block + single site, one gets the reduced density matrix for the subsystem single site + right block (Fig. 4.1):

$$\hat{\rho}_B^{[l+1\ldots L]} = \sum_{\ell'\gamma'} \sum_{\ell\gamma} \left(\sum_{\alpha k} \Theta^{*}_{\alpha k,\ell'\gamma'} \Theta_{\alpha k,\ell\gamma} \right) |\ell'\gamma'\rangle\langle\ell\gamma| \tag{4.6}$$

If $\Theta_{\alpha k,\ell\gamma}$ is viewed as a matrix with the composite index (αk) as row index and $(\ell\gamma)$ as column index, the reduced density matrix $\hat{\rho}_B^{[l+1\ldots L]}$ in the $|\ell\gamma\rangle$-basis is:

$$\rho_B = \Theta^{\dagger}\Theta \tag{4.7}$$

Equation (4.6) is the starting point for the basis truncation: By diagonalising this reduced density matrix one gets the eigenvalues $\{(\lambda_{\beta}^{\prime[l]})^2\}$ which are the new Schmidt coefficients squared (See 2.1).

The eigenvectors $\{|\Phi'^{[l+1\ldots L]}_{\beta}\rangle\}$ form the new right Schmidt basis for the Schmidt decomposition at site l. They are given in the $\{|\ell\gamma\rangle\}$-basis and their representation in this basis shall be $\vec{\Phi}'_{\beta}$.

Up to now all expressions were exact, now the truncation is performed. The dimension of the reduced density matrix is $d*M$. To reduce the number of basis states, one keeps only the M eigenstates with the highest weight - that are the eigenvectors corresponding to the M highest eigenvalues.

Since some of the Schmidt coefficients are discarded and condition (2.2) has to be fulfilled, one has to renormalise the new Schmidt coefficients:

$$\tilde{\lambda}'^{[l]}_{\alpha} = \frac{\lambda'^{[l]}_{\alpha}}{\sqrt{\sum_{\beta=1}^{M}\left(\lambda'^{[l]}_{\beta}\right)^2}} \tag{4.8}$$

A useful quantity in error discussions is the *truncated weight* w, resulting from this approximation step:

$$w = 1 - \sum_{\beta=1}^{M}\left(\lambda'^{[l]}_{\beta}\right)^2 \tag{4.9}$$

From the Schmidt decomposition (4.1) the following expression follows:

$$\left|\Phi'_{\beta}{}^{[l+1\ldots L]}\right\rangle = \sum_{\ell}^{d}\sum_{\gamma}^{M}\Gamma'_{\beta\gamma}{}^{\ell[l+1]}\lambda^{[l+1]}_{\gamma}\,|\ell\gamma\rangle \tag{4.10}$$

The new $\Gamma'^{\ell[l+1]}$ tensors are then given by

$$\Gamma'_{\beta\gamma}{}^{\ell[l+1]} = \frac{1}{\lambda^{[l+1]}_{\gamma}}\left\langle \ell\gamma \,\middle|\, \Phi'_{\beta}{}^{[l+1\ldots L]}\right\rangle \tag{4.11}$$

or

$$\Gamma'_{\beta\gamma}{}^{\ell[l+1]} = \frac{(\vec{\Phi}'_{\beta})_{(\ell\gamma)}}{\lambda^{[l+1]}_{\gamma}} \tag{4.12}$$

Aside from the Hilbert space truncation, one has to introduce a cut-off of the Schmidt coefficients, because of the divisions in (4.12) and (4.16).

What is still missing are the new $\Gamma'^{\,k[l]}$ tensors: The Schmidt decomposition (4.1) gives

$$\lambda'^{[l]}_{\beta}\left|\Phi'_{\beta}{}^{[1\ldots l]}\right\rangle = \left\langle \Phi'_{\beta}{}^{[l+1\ldots L]}\,\middle|\,\Psi'\right\rangle \tag{4.13}$$

Plugging in expression (4.3) and using (4.11) one gets

$$\lambda'^{[l]}_{\beta} \left| \Phi'_{\beta}{}^{[1\ldots l]} \right\rangle = \sum_{\alpha k} \left(\sum_{\ell\gamma} (\Gamma'_{\beta\gamma}{}^{\ell[l+1]})^* \lambda^{[l+1]}_{\gamma} \Theta_{\alpha k,\ell\gamma} \right) |\alpha k\rangle \tag{4.14}$$

Comparing this with the expansion of $\left|\Phi'^{[1\ldots l]}_{\beta}\right\rangle = \sum_{\alpha k} \lambda^{[l-1]}_{\alpha} \Gamma'_{\alpha\beta}{}^{k[l]} |\alpha k\rangle$ yields:

$$\Gamma'_{\alpha\beta}{}^{k[l]} = \frac{1}{\lambda^{[l-1]}_{\alpha}} \sum_{\ell} \sum_{\gamma} \left(\Gamma'_{\beta\gamma}{}^{\ell[l+1]} \right)^* \lambda^{[l+1]}_{\gamma} \Theta_{\alpha k,\gamma\ell} \tag{4.15}$$

Using (4.12) finally gives

$$\Gamma'_{\alpha\beta}{}^{k[l]} = \frac{1}{\lambda^{[l-1]}_{\alpha}} \sum_{\ell\gamma} \Theta_{\alpha k,\ell\gamma} (\vec{\Phi}'_{\beta})^*_{(\ell\gamma)} \tag{4.16}$$

One sees that this expression can be realised by a matrix-vector multiplication. See also [18, 1]

The calculation of all elements of the Θ-Tensor in (4.4) dominates the computational cost of the TEBD algorithm. It takes $O(d^4 M^3)$ elementary operations. Considering the system size L and the number of timesteps n, the TEBD algorithm therefore has the following asymptotical runtime T:

$$T(n, L, d, M) = O(n\, L\, d^4\, M^3) \tag{4.17}$$

The amount of memory needed is essentially the size of one matrix product state in memory, which is $O(L\, d\, M^2)$.

> This shows that the computational cost of TEBD algorithm scales only linearly with system size. Thus it is "efficient" in the information theoretical sense.

4.1.1 Justification of the Truncation Procedure

The reasons for keeping the states with the highest eigenvalue of the reduced density matrix are:

1. Minimisation of the distance between true and approximate state

   $$|| \, |\Psi\rangle - |\tilde{\Psi}\rangle \, ||^2 = w \tag{4.18}$$

   The distance squared between the state $|\Psi\rangle$ and the approximate state $|\tilde{\Psi}\rangle$ is equal to the truncated weight w (4.9). We see this by inserting the Schmidt decompositions into the formula above. Keeping the highest eigenvalues minimises the truncated weight and therefore the distance between the states.

2. Optimization of expectation values
   For a bounded operator $\hat{A}$, the error of its expectation value is of the order of the truncated weight. We suppose that $\hat{A}$ acts on the right subsystem B:

$$\langle \hat{A} \rangle = \operatorname{tr} \hat{\rho}_B \hat{A} = \sum_{\beta=1}^{\chi} \lambda'^2_\beta \left\langle {\Phi'_\beta}^{[l+1\ldots L]} \,\middle|\, \hat{A} \,\middle|\, {\Phi'_\beta}^{[l+1\ldots L]} \right\rangle \tag{4.19}$$

$$\langle \hat{A} \rangle_{\text{approx.}} = \sum_{\beta=1}^{M} \lambda'^2_\beta \left\langle {\Phi'_\beta}^{[l+1\ldots L]} \,\middle|\, \hat{A} \,\middle|\, {\Phi'_\beta}^{[l+1\ldots L]} \right\rangle$$

$$\begin{aligned} |\langle \hat{A} \rangle - \langle \hat{A} \rangle_{\text{approx.}}| &= \sum_{\beta=M+1}^{\chi} \lambda'^2_\beta \left\langle {\Phi'_\beta}^{[l+1\ldots L]} \,\middle|\, \hat{A} \,\middle|\, {\Phi'_\beta}^{[l+1\ldots L]} \right\rangle \\ &\leq k \left(\sum_{\beta=M+1}^{\chi} \lambda'^2_\beta \right) = k \cdot w \end{aligned} \tag{4.20}$$

   In the last line k is an upper bound for the expectation value of the bounded operator $\hat{A}$.

3. Preservation of entanglement
   The discarded von Neumann entropy $-\sum_{\beta=M+1}^{\chi} \lambda'^2_\beta \log \lambda'^2_\beta$ is also minimised, provided that the discarded eigenvalues are small enough. Small enough means that $0 \leq \lambda'^2_\beta \leq 1/e$ because in this interval $-x \log x$ grows monotonically.

[16]

4.1.2 Equivalence with the SVD

In this section it is shown that constructing the reduced density matrix and diagonalising it to get the states with highest weight is equivalent to the singular value decomposition (SVD, section 2.1) of Θ.

Instead of using the reduced density matrix of the right subsystem, one could also use the reduced density matrix of the left subsystem, for they have the same eigenvalues (see section 2.2).

Analogous to (4.7) the reduced density matrix for the left subsystem is

$$\rho_A = \Theta\Theta^\dagger \tag{4.21}$$

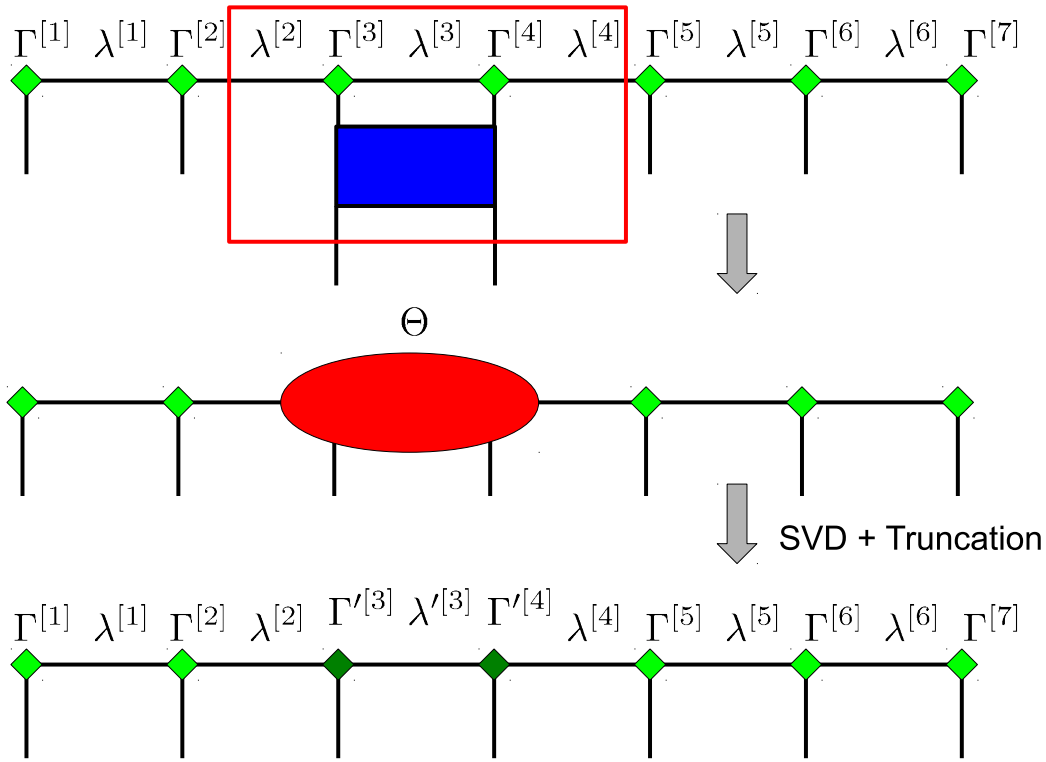

Figure 4.2: Outline: Application of a two-site operator. Here the two-site operator acts on sites 3 and 4. Only the Γ and λ in the box are modified.

which can be shown by performing the partial trace over the right subsystem in (4.5). With the singular value decomposition $\Theta = U\Lambda V^\dagger$ one gets

$$\rho_A = U\Lambda\Lambda^\dagger U^\dagger \qquad \rho_B = V\Lambda^\dagger\Lambda V^\dagger \tag{4.22}$$

Since $\Lambda\Lambda^\dagger$ and $\Lambda^\dagger\Lambda$ are diagonal matrices, and U and V are unitary, equation (4.22) shows the spectral decomposition of the reduced density matrices of the left and the right subsystem respectively. We know that these eigenvalues are the same and any other entry on the diagonals is zero. Therefore the matrix Λ of the SVD decomposition contains the Schmidt coefficients $\lambda_\beta^{[l]}$ on its diagonal. For the tensors Γ' one gets:

$$\Gamma'^{\,k[l]}_{\alpha\beta} = \frac{1}{\lambda_\alpha^{[l-1]}} U_{(\alpha k),\,\beta} \tag{4.23}$$

$$\Gamma'^{\,\ell[l+1]}_{\beta\gamma} = \frac{1}{\lambda_\gamma^{[l+1]}} V^\dagger_{\beta,\,(\ell\gamma)} \tag{4.24}$$

This follows by comparison of

$$\Theta_{\alpha k,\ell\gamma} = \sum_\beta^M \lambda_\alpha^{[l-1]} \Gamma'^{\,k[l]}_{\alpha\beta} \lambda'^{[l]}_\beta \Gamma'^{\,\ell[l+1]}_{\beta\gamma} \lambda_\gamma^{[l+1]} \tag{4.25}$$

with the singular value decomposition of Θ:

$$\Theta_{\alpha k,\,\ell\gamma} = \sum_\beta U_{(\alpha k),\,\beta}\, \Lambda_{\beta\beta}\, V^\dagger_{\beta,\,(\ell\gamma)} \tag{4.26}$$

Figure 4.2 summarises the procedure of the two-site operator application: At first the Γ and λ objects in the box are reduced to the Θ-tensor, then a SVD or the procedure described in 4.1 is performed. Only the states with the highest weight are kept (truncation) and the new Γ' and λ' are constructed.

4.1.3 Conserved Additive Quantum Numbers

The two-site operator application can be substantially optimised using symmetries of the model which lead to conserved quantum numbers. Here one additive quantum number such as the total particle number in the Hubbard model or total spin in z-direction will be considered. An overview of the necessary modifications to the algorithm can be found in [18]. Here I want to give a more detailed description:

If a system is split into two parts A and B, the additive quantum number can be evaluated for each part and adds up to constant: $N(A)+N(B) = N = \text{const}$. $N(A)$ means that the quantum number is evaluated for subsystem A.

Let N be the conserved total number. Then in equation (4.3) the coefficients $\Theta_{\alpha k,\ell\gamma}$ are non-zero only if $N(\alpha)+N(k)+N(\ell)+N(\gamma)=N$

Conserved total particle number (charge conservation) in the Hubbard model and conservation of total spin in z-direction (e.g. Hubbard and Heisenberg model) correspond to U(1) symmetries [16]. We define the following quantities:

$$\begin{aligned} N_L &:= N(\alpha)+N(k) \\ N_R &:= N(\ell)+N(\gamma) \\ N_L + N_R &= N \end{aligned} \tag{4.27}$$

N_L is the quantum number in the left subsystem, N_R the number in the right subsystem. Equation (4.3) can then be rewritten as

$$|\Psi'\rangle = \sum_{\{N_R\}} \left(\sum_{\substack{\alpha k \\ N(\alpha)+N(k)=N-N_R}} \sum_{\substack{\ell\gamma \\ N(\ell)+N(\gamma)=N_R}} \Theta_{\alpha k,\ell\gamma} \, |\alpha k \ell\gamma\rangle \right) \tag{4.28}$$

In this expression a sum over all possible N_R is introduced. The indices α, k, ℓ and γ are restricted to values such that conditions (4.27) are fulfilled.

One then sees that the reduced density matrix $\hat{\rho}_B^{[l+1\ldots L]}$ of equation (4.6) is block diagonal, with blocks $\hat{\rho}_B^{[l+1\ldots L],N_R}$ that can be labelled by the quantum number N_R:

$$\begin{aligned} \hat{\rho}_B^{[l+1\ldots L]} = \sum_{\{N_R\}} \Bigg[& \sum_{\substack{\ell'\gamma' \\ N(\ell')+N(\gamma')=N_R}} \sum_{\substack{\ell\gamma \\ N(\ell)+N(\gamma)=N_R}} \\ & \left(\sum_{\substack{\alpha k \\ N(\alpha)+N(k)=N-N_R}} (\Theta_{\alpha k,\ell'\gamma'})^* \Theta_{\alpha k,\ell\gamma} \right) |\ell'\gamma'\rangle \langle \ell\gamma| \Bigg] =: \sum_{\{N_R\}} \hat{\rho}_B^{[l+1\ldots L],N_R} \end{aligned} \tag{4.29}$$

Introducing the mapping μ_R that maps the running index $x = 1, 2, 3, \ldots$ to the composite index $(\ell\gamma)$ such that $N(\ell)+N(\gamma)=N_R$ we can rewrite the previous equations. The mapping μ_L maps x to the composite index (αk) such that $N(\alpha)+N(k)=N_L$:

$$\begin{array}{lcll} \mu_R(x;N_R) & : & x \mapsto (\ell\gamma) & \text{where} \quad N(\ell)+N(\gamma)=N_R \\ \mu_L(x;N_R) & : & x \mapsto (\alpha k) & \text{where} \quad N(\alpha)+N(k)=N-N_R \end{array} \tag{4.30}$$

Equation (4.28) becomes:

$$|\Psi'\rangle = \sum_{\{N_R\}} \sum_{x=1} \sum_{y=1} \Theta_{\mu_L(x;N_R),\,\mu_R(y;N_R)}\, |\mu_L(x;N_R)\ \mu_R(y;N_R)\rangle \tag{4.31}$$

This leads to the definition of the matrices Θ^{N_R}, which are labelled by the quantum number N_R. Their matrix elements are

$$\begin{aligned} \Theta^{N_R}_{x,y} &:= \Theta_{\mu_L(x;N_R),\,\mu_R(y;N_R)} \\ x &= 1, 2, 3, \ldots \\ y &= 1, 2, 3, \ldots \end{aligned} \tag{4.32}$$

The reduced density matrix blocks $\hat{\rho}_B^{[l+1\ldots L],N_R}$ of (4.29) represented in the $|\ell\gamma\rangle$ basis with fixed N_R are:

$$\rho_B^{N_R} = (\Theta^{N_R})^\dagger \Theta^{N_R} \tag{4.33}$$

Diagonalising each block on its own saves computational time and gives eigenvalues, whose square roots are $\lambda'^{[l],N_R}_\beta$ and corresponding eigenvectors $\vec{\Phi}'^{N_R}_\beta$ also labelled by N_R. Then only the solutions with the M highest eigenvalues of *all* blocks are kept: $\beta = 1, 2, \ldots M$

Bookkeeping is necessary to keep track of the quantum numbers for (4.27). This is done by using hash tables for each site l which map the quantum number $N_{R,l}$ of the block to the right of site l to its corresponding block index β. These tables will be called *number tables*. They have to be updated after the reduced density matrix diagonalisation. The number tables are initialised according to the starting state one uses. For a Fock state (simple tensor product) the number of particles to the right of any site (N_R) is known and the number maps each get one entry which map index $\beta = 1$ to N_R. It is also necessary to know the mapping of the single site basis to the single site quantum number contribution.

One has to take care to put the results into the correct positions in the new Γ-tensors. We use mappings $\mu_{L,\alpha}$ and $\mu_{L,k}$ that give the indices α, k of the composite index (αk). Similarly $\mu_{R,\ell}$ and $\mu_{R,\gamma}$ give the indices ℓ, γ of $(\ell\gamma)$. Then (4.12) translates to

$$\Gamma'^{\ \mu_{R,\ell}(y;N_R)\ [l+1]}_{\beta,\ \mu_{R,\gamma}(y;N_R)} = \frac{(\vec{\Phi}'^{N_R}_\beta)_y}{\lambda^{[l+1]}_{\mu_{R,\gamma}(y;N_R)}} \tag{4.34}$$

Equation (4.16) becomes

$$\Gamma'^{\ \mu_{L,k}(x;N_R)\ [l]}_{\mu_{L,\alpha}(x;N_R),\ \beta} = \frac{1}{\lambda^{[l-1]}_{\mu_{L,\alpha}(x;N_R)}} \sum_{y=1} \Theta^{N_R}_{x,y} (\vec{\Phi}'^{N_R}_\beta)^*_y \tag{4.35}$$

This procedure is again equivalent to the singular value decomposition (section 4.1.2) as one can perform the SVD on each Θ^{N_R} individually.

To implement the conservation of more than one additive quantum number N_R is replaced by a vector of quantum numbers $\vec{N}_R$ and conditions similar to (4.27) have to be fulfilled for all quantum numbers simultaneously.

In the Hubbard model, for example, the number of spin-up ($N_\downarrow$) and spin-down ($N_\uparrow$) particles are conserved individually. If only one conserved quantum number is implemented in the program the following workaround allows the conservation of both particle numbers: Count each spin-up particle as $L+1$ particles and each spin-down particle as 1 particle, where L is the number of sites. Use $\tilde{N} = (L+1)N_\uparrow + N_\downarrow$ as the new conserved quantum number. Since each site can be occupied only by one particle of a spin species, $N_\downarrow$ and $N_\uparrow$ are conserved. This is important because otherwise small numerical errors can lead to conversion from one spin species to another.

Summary. The steps of the algorithm are now:

1. For the application of the two-site operator on site l and $l+1$, form all valid combinations of N_L and N_R, such that their sum equals the total quantum number N: $N_L + N_R = N$.

2. Build lists of valid indices α, k, ℓ and γ, such that $N(\alpha) + N(k) = N_L$ and $N(\ell) + N(\gamma) = N_R$

3. For each N_R calculate the matrix Θ^{N_R} (4.32) using the index lists to calculate only non-zero elements.

4. Build the blocks of the reduced density matrix and diagonalise them or perform SVDs on the Θ^{N_R}. Sort all solutions by eigenvalue and keep the solutions with the M highest eigenvalues.

5. Update the number tables.

6. Calculate the new Schmidt coefficients (square roots of eigenvalues) and Γ-Tensors (4.34) and (4.35).

The computational cost of the algorithm taking into account conserved quantum numbers is still given by (4.17), since the dimension of the largest reduced density block is still $O(M)$. Nevertheless, a speed-up by a considerable constant factor is achieved.

4.1.4 TEBD Sweeps

A TEBD sweep using the 1st order Trotter decomposition is one application of (1.15) on the matrix product state. The relevant two-site gates are then $\exp(-i\hat{h}_{l,l+1}\tau)$, where $\hat{h}_{l,l+1}$ are the parts in sum (1.6). The two-site gates are therefore (small) $d^2 \times d^2$ matrices and the matrix exponential is calculated easily.

For more accurate results one can use the 2nd order Trotter decomposition with almost no additional computational effort. The 2nd order Trotter decomposition is (x and y are non-commuting objects):

$$\begin{aligned} e^{x+y} &= e^{x/2}\, e^{y}\, e^{x/2} + O(\tau^3) \\ x &= -i\hat{H}_{\text{odd}}\, \tau \\ y &= -i\hat{H}_{\text{even}}\, \tau \end{aligned} \tag{4.36}$$

By applying the matrix exponentials in the formula above repeatedly and simplifying, one gets:

$$e^{x/2}\, e^{y}\, \underbrace{e^{x/2}\, e^{x/2}}_{e^{x}}\, e^{y}\, e^{x/2}\, \ldots\, e^{x/2}\, e^{y} e^{x/2} = e^{x/2}\, e^{y}\, e^{x}\, e^{y}\, e^{x}\, \ldots\, e^{y}\, e^{x/2} \tag{4.37}$$

This resembles the 1st order decomposition, except that the first and the last operator are different. Therefore the computational cost is roughly the same. Note that before performing a measurement step the current time step has to be completed and after the measurement a new time step starts. The sequence of operations therefore is: apply $e^{x/2}$ - measure - apply $e^{x/2}$.

In the case of an evolution in imaginary time, the two-site gate is not unitary, which leads to orthonormality problems. A solution to this is described in section 4.3.2.

A different approach is the use of a N-operator decomposition, where no even-odd splitting is necessary and one can sweep sequentially through the chain. This is described in [19], but was not used in this work. As a convenient side-effect the problem of non-unitary operators is also solved.* Non-unitary operators are used e.g. for the evolution in imaginary time, which is treated in section 4.3.

*Thanks to A. Daley for bringing this to my attention.

4.2 Error Sources

The TEBD algorithm has two sources of error: the Trotter error and the truncation error. Section 1.2 deals with the Trotter decomposition of a matrix exponential and its associated error. A p-th order Trotter decomposition for one timestep τ has a error of order τ^{p+1}. Since the number of timesteps needed to simulate up to a time t is t/τ the overall Trotter error is [20]

$$\epsilon_{\text{Trotter}} = O(\tau^p\, t) \tag{4.38}$$

The Trotter error is independent of system size and scales *linearly* with simulation time.

For the long time behaviour of adaptive Hilbert space methods the truncation error is the dominant error source. At each application of a two-site gate states with the weight (4.9) are discarded. Because of this truncated weight a renormalisation of the state (4.8) takes place. The number of gate applications for a simulation up to time t is $O(Lt/\tau)$, which is also the number of state renormalisations. Therefore the truncation error is

$$\epsilon_{\text{trunc}} = O((1-w)^{L\,t/\tau}) = O(\exp(\ln(1-w) * L\,t/\tau)) \tag{4.39}$$

where w is the maximal truncated weight.

This shows that the truncation error scales *exponentially* with time and system size, determining the long time stability of the algorithm, which leads to a "run-away time" at which the simulation breaks down [20]. A reduction of the truncation error is possible if one increases the MPS matrix dimension M and therefore reduces the truncated weight.

The choice of the timestep also plays a crucial role: On the one hand small timesteps lead to a smaller Trotter error, but on the other hand a higher number of gate application is necessary, which increases the truncation error. This limits the usefulness of higher order Trotter decompositions.

Reliable absolute error values are difficult to obtain, unless the time-evolution is exactly calculatable. One possibility is to perform the same calculation for different M, considering a result with high M as "exact".

4.3 Imaginary Time Evolution

4.3.1 Ground State Approximation by Imaginary Time Evolution

Being able to simulate time evolutions makes it possible to find an approximation to the ground state of a system with almost unchanged simulation

code [4, 18]. Instead of simulating the evolution in real time one sets

$$t = -i\beta \tag{4.40}$$

in the time evolution operator. In the limit $\beta \to \infty$ one gets the ground state $|E_0\rangle$:

$$|E_0\rangle = \lim_{\beta\to\infty} \frac{e^{-\beta\hat{H}}\,|\phi\rangle}{||e^{-\beta\hat{H}}\,|\phi\rangle\,||} \tag{4.41}$$

Here $|\phi\rangle$ is a starting state with non-zero overlap with the ground state:

$$\langle E_0\,|\,\phi\rangle \neq 0 \tag{4.42}$$

As initial state one can choose a simple tensor product state using (3.25).

By using the expansion of $|\phi\rangle$ in the eigenbasis of $\hat{H}$ one sees that states with energy above the ground state are exponentially damped:

$$e^{-\beta\hat{H}}\,|\phi\rangle = \sum_{i=0} e^{-\beta E_i} c_i\,|E_i\rangle = e^{-\beta E_0} c_0\,|E_0\rangle + e^{-\beta E_0} \sum_{i=1} e^{-\beta(E_i-E_0)} c_i\,|E_i\rangle \tag{4.43}$$

It is now obvious that an energy gap is necessary for the imaginary time evolution to yield the ground state. The condition for the imaginary time reached during simulation is $\beta \gg \frac{1}{E_1-E_0}$. Many interesting systems are gapless in the thermodynamic limit, but as we are simulating finite size systems, there is always a finite size gap. This gap decays with system size thus rendering the imaginary time evolution less useful for large systems. Here optimisation schemes such as DMRG or variational MPS methods are advantageous.

It is important to choose quite large imaginary timesteps in the beginning to reach a large β. Then the timestep is decreased, reducing the Trotter error, to get a more accurate representation of the state. One decreases the timestep, when the energy change between two measurement steps becomes smaller than a certain tolerance.

4.3.2 Non-Unitary Operators in TEBD

As pointed out by Daley in [18], the application of a non-unitary operator changes not only the norm of the state, but also does not conserve the orthonormality of Schmidt basis vectors. All Schmidt vectors that contain the sites the operator is applied on, are expected to become non-orthonormal. To see what happens, consider the application of the non-unitary operator on sites l and $l+1$. Note that the sets $\{|\Phi_\alpha^{[1\ldots l]}\rangle\}$ and $\{|\Phi_\alpha^{[l+1\ldots L]}\rangle\}$ of Schmidt

vectors are explicitly normalised by the TEBD-algorithm. On the other hand bases of the left subsystem such as $\{|\Phi_\alpha^{[1\ldots l+1]}\rangle\}$, $\{|\Phi_\alpha^{[1\ldots l+2]}\rangle\}$, ... and bases of the right subsystem such as $\{|\Phi_\alpha^{[l\ldots L]}\rangle\}$, $\{|\Phi_\alpha^{[l-1\ldots L]}\rangle\}$, ... lose orthonormality because they contain site l or site $l+1$.

The following imaginary time evolution scheme was used to ensure orthonormality: Apply odd operator on sites (1,2), apply identity operator on sites (2,3), apply odd operator on sites (3,4), ... and so on. When the end of the chain is reached, perform a backward sweep with the even operators alternating with the identity operator: If the last operation was an application of the identity operator, apply an even operator and vice versa. In the end a last sweep with just the identity operator is performed to restore orthonormality. Using this simulation scheme using a higher order Trotter decomposition is possible.

During the two-site operator application one also has to renormalise the Θ-coefficients (4.3) to keep the norm of the state equal to 1:

$$\tilde{\Theta}_{\alpha k \ell \gamma} = \frac{\Theta_{\alpha k \ell \gamma}}{\sqrt{\sum_{\alpha k \ell \gamma} |\Theta_{\alpha k \ell \gamma}|^2}} \tag{4.44}$$

4.4 Consequences for Quantum Computing

In computer science (decision) problems are divided into complexity classes according to their "difficulty". An algorithm is called efficient if its running time is upper bounded by a polynomial of the input length.

All problems that are solved by an efficient (polynomial time) algorithm are members of the complexity class P. For probabilistic algorithms the class BPP contains problems that can be solved by a classical computer in polynomial time with low probability of error.

A quantum analogue to BPP is the class BQP, which contains the problems that can be solved by a polynomial time *quantum* computation with low probability of error. Showing that BQP contains problems that are not in BPP would prove that quantum computers are more powerful than classical computers. Up to date this remains an open question. See also [6].

As stated in Vidal's paper [1] a future quantum computer has to involve dynamics which are not efficiently simulatable on a classical computer to perform calculations in polynomial time that a classical computer can not.

Combining the knowledge about entanglement, matrix product states and the application of quantum gates, the following consequence for the classical simulation of a quantum computation arises:

> Suppose that an input of L qubits should be processed in a quantum computation. This quantum computation is efficiently simulatable on a classical computer if it uses poly(L) gates and E_χ (2.10) does not grow faster than $\log(L)$. [1]

Thus the minimal amount of entanglement that must be present in a quantum computer has to scale faster then $\log(L)$.

4.5 The TEBD Program

I implemented the algorithm in the previous sections using the C++ programming language. Matrix and vector data structures are provided by uBLAS which is part of the Boost C++-libraries [21]. The diagonalisation of the reduced density matrix uses LAPACK [22].

I wrote simulation code for the Heisenberg and the Hubbard model. During development results for systems with few sites were checked with a MATLAB-program I wrote, which calculates the full time evolution operator. Features of the program include binary input and output of matrix product states in canonical normal form, conserved particle number and ground state approximation by imaginary time evolution. Core parts of the program were used to obtain the results in [23, 24].

Some elements of object oriented programming are used in the program. Figure 4.3 shows the class diagram. The class `MatrixProductState` implements a MPS in canonical normal form. The central method is `apply_two_site_op`, which implements the two-site gate operation described in section 4.1.

This class serves as a base class for `MatrixProductStateFixedNumber`, whose overloaded method `apply_two_site_op` uses the conservation of one additive quantum number for speed-up.

One then has to implement the desired TEBD sweep scheme, which involves repeated calls of `apply_two_site_op` with the desired TEBD time evolution gate given as a complex matrix.

4.6 Related Methods

- Adaptive time dependent density matrix renormalisation group (*adaptive t-DMRG*): This method is essentially an implementation of the TEBD idea of applying two-site gates into existing DMRG code, taking advantage of already existing DMRG-optimisations such as conserved

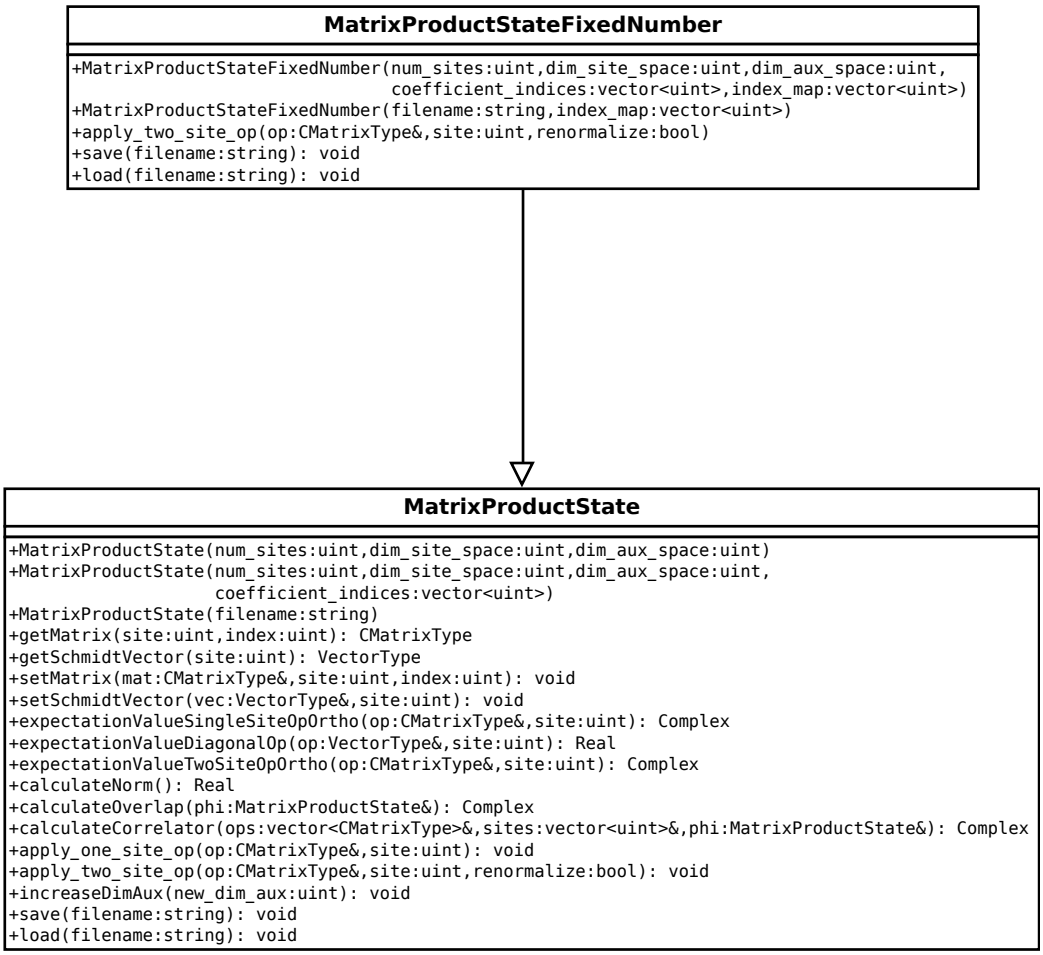

Figure 4.3: Class diagram of the TEBD program core

quantum numbers [9]. It was developed independently from TEBD though.

- iTEBD (infinite size TEBD): For translationally invariant systems [25]
- TEBD for mixed states: Mixed state evolution is calculatable by writing the mixed state as a partial trace of a pure state in a larger Hilbert space (purification). The approach in the cited paper uses the superoperator formalism [26].

Chapter 5

Interacting Fermions in One Dimension

This chapter provides some theoretical background for the simulations that are presented in chapter 6. Spinless fermions with nearest-neighbour interactions and the Hubbard model, which includes spin, describe fermions on a lattice. The Luttinger liquid theory is a field theoretical treatment of interacting fermions in one dimension. If the interaction strength varies throughout the system, reflection phenomena such as hole-like reflections can occur. These reflections are also known as Andreev-like reflections.

5.1 Spinless Fermions

One can speak of "spinless fermions", if spin can be disregarded, e.g. if all particles have the same spin orientation. In a spinless fermion lattice model one site can either be occupied or unoccupied. In second quantisation the Hamiltonian for spinless fermions on a one dimensional lattice with open boundary conditions is:

$$\hat{H} = -t \sum_{i=1}^{L-1} (c_i^\dagger c_{i+1} + c_{i+1}^\dagger c_i) + \sum_{i=1}^{L-1} V_i \ \hat{n}_i \hat{n}_{i+1} + \sum_{i=1}^{L} \epsilon_i \hat{n}_i \tag{5.1}$$

The operators $c_i / c_i^\dagger$ destroy/create a fermion in a Wannier-state localised at site i. Here the interaction consists of nearest-neighbour interactions (possibly site-dependent). Furthermore an interaction with a site dependent external field ϵ_i is added (related to a chemical potential by $\mu_i = -\epsilon_i$). $\hat{n}_i = c_i^\dagger c_i$ is the number operator.

This Hamiltonian is related to the Hamiltonian of the one-dimensional Heisenberg model (with anisotropy):

$$\hat{H} = \frac{J_{xy}}{2} \sum_{i=1}^{L-1} (\hat{S}_i^+ \hat{S}_{i+1}^- + \hat{S}_{i+1}^+ \hat{S}_i^-) + \sum_i J_{z,i}\ \hat{S}_i^z \hat{S}_{i+1}^z - \sum_i B_i \hat{S}_i^z \tag{5.2}$$

The spin operators $\hat{S}_i^+$, $\hat{S}_i^-$, $\hat{S}_i^z$ can be transformed into the fermionic creation/annihilation operators $c_i / c_i^\dagger$ by means of the Jordan-Wigner transformation:

$$\hat{S}_j^+ = \exp\left(i\pi \sum_{k=1}^{j-1} \hat{n}_k\right) c_j^\dagger \qquad \hat{S}_1^+ = c_1^\dagger \tag{5.3}$$

$$\hat{S}_j^- = c_j \exp\left(-i\pi \sum_{k=1}^{j-1} \hat{n}_k\right) \qquad \hat{S}_1^- = c_1$$

$$\hat{S}_j^z = \hat{n}_j - \frac{1}{2}$$

This transformation is necessary because of the different commutation/ anticommutation - relations of spin and fermion operators. [27]

5.2 Hubbard Model

The Hubbard model describes fermions with spins on a lattice and includes only an on-site (Coulomb) interaction for a pair of anti-parallel spins (Pauli principle). The Hamiltonian for the 1D Hubbard model with open boundary conditions is

$$\hat{H} = -t \sum_{\substack{i=1 \\ \sigma=\uparrow,\downarrow}}^{L-1} (c_{i,\sigma}^\dagger c_{i+1,\sigma} + c_{i+1,\sigma}^\dagger c_{i,\sigma}) + \sum_i U_i \hat{n}_{i\uparrow} \hat{n}_{i\downarrow} \tag{5.4}$$

The operators $c_{i,\sigma}$ destroy a particle with spin σ in the Wannier state localized at site i.

The possible configurations for one site are $|\,\rangle$, $|\downarrow\rangle$, $|\uparrow\rangle$, $|\downarrow\uparrow\rangle$ - the local Hilbert space has dimension 4.

At half filling and strong interaction $U \gg t$ the Hubbard model is approximated by the anti-ferromagnetic Heisenberg model with $J = 4t^2/U$. [28] (In this case the Heisenberg model is isotropic with $J = J_z = J_{xy}$)

In the following section we will discuss perturbations of the charge and spin density. The charge/particle density is given by

$$\hat{n}_i^\rho = \hat{n}_{i\uparrow} + \hat{n}_{i\downarrow} \tag{5.5}$$

and the spin density by

$$\hat{n}_i^\sigma = \hat{n}_{i\uparrow} - \hat{n}_{i\downarrow} \tag{5.6}$$

5.3 Luttinger Liquid

In two and three dimensions interacting electrons/fermions are often successfully described by Landau's Fermi liquid theory. It assumes an one-to-one correspondence between the eigenstates of the non-interacting system and the system with interaction. This means that the interacting system can be described by the same quantum numbers as the non-interacting system. The elementary excitations for low energies are quasi-particle excitations. These quasi-particles are fermions and carry one elementary charge (in the case of charged particles). In solid state physics one calls this quasi-particle also an electron, but with a new *effective* mass. It is customary to introduce "holes" if an electron is absent. [29, 30, 31]

In one dimension, however, it turns out that the Fermi-liquid theory does not apply. The elementary excitations are collective, *bosonic* ones.

In one dimension the Fermi-surface is just two Fermi-points at wavenumbers $-k_F$ and k_F. The Luttinger-liquid theory assumes linearised energy-momentum dispersion relations around the Fermi-points.

In the spinless Fermion case one gets after applying the "bosonisation"-technique the following Hamitonian:

$$H = \frac{1}{2\pi} \int u \left[K(\pi \Pi(x))^2 + \frac{1}{K} (\partial_x \phi(x))^2 \right] dx \tag{5.7}$$

Here $\phi(x)$ is a field operator which is related to the charge density operator by $\rho(x) = -\frac{1}{\pi} \partial_x \phi(x)$. $\Pi(x)$ is the conjugate momentum to $\phi(x)$.

u and K are the Luttinger parameters, which completely determine the behaviour of the system.

The commutator of $\phi(x)$ and $\Pi(x')$ obeys the familiar *bosonic* commutation relation:

$$[\phi(x), \Pi(x')] = i\delta(x - x') \tag{5.8}$$

The Hamiltonian resembles that of the continuum limit of coupled harmonic oscillators.

The bosonisation procedure can be carried out for fermions with spin as well. A change in variables from the field corresponding to spin up $\phi_\uparrow$ and spin down $\phi_\downarrow$ to fields associated with spin (ϕ_σ) and charge (ϕ_ρ) shows that

the Hamiltonian decouples into a charge part H_ρ and a spin part H_σ. An additional term turns out to be irrelevant in a renormalisation group study and is dropped:

$$H = H_\rho + H_\sigma \tag{5.9}$$

The terms H_ρ and H_σ are similar to the spinless case with:

$$H_\nu = \frac{1}{2\pi} \int u_\nu \left[K_\nu (\pi \Pi_\nu(x))^2 + \frac{1}{K_\nu} (\partial_x \phi_\nu(x))^2 \right] dx \tag{5.10}$$
$$\nu = \rho,\ \sigma$$

The decoupling of the Hamiltonian leads to an effect known as spin-charge separation: Spin and charge become completely independent degrees of freedom. Therefore the elementary excitations can not be attributed to quasiparticles carrying spin *and* charge. See also [32, 33]. For a more detailed presentation I refer to additional literature [31].

The four Luttinger parameters u_ρ, u_σ, K_ρ and K_σ can only be calculated if one chooses an underlying *microscopic* theory such as the 1D Hubbard model (Section 5.2). Using the Hubbard model it turns out that K_σ is always equal to 1, leaving only three parameters. The parameters depend on the interaction strength U/t and on the Fermi-momentum - and therefore also on the number of particles in the system. u_ρ and u_σ are identified as charge- and spin-velocity respectively. They are given by the slopes of the linear dispersion relations of charge and spin excitations.

The calculation of the Luttinger parameters is based on the Bethe-ansatz, which provides an analytical solution to the one-dimensional Hubbard-model. Graphs which show the dependence of the Luttinger parameters on the parameters of the Hubbard model can be found in [33] and [31] (shown in figures 5.1 and 5.2). The repulsive Hubbard model has $K_\rho < 1$, whereas the attractive Hubbard model has $K_\rho > 1$. For non-interacting fermions ($U = 0$), $K_\rho = 1$ and $u_\rho = u_\sigma = v_F$, where v_F is the Fermi-velocity.

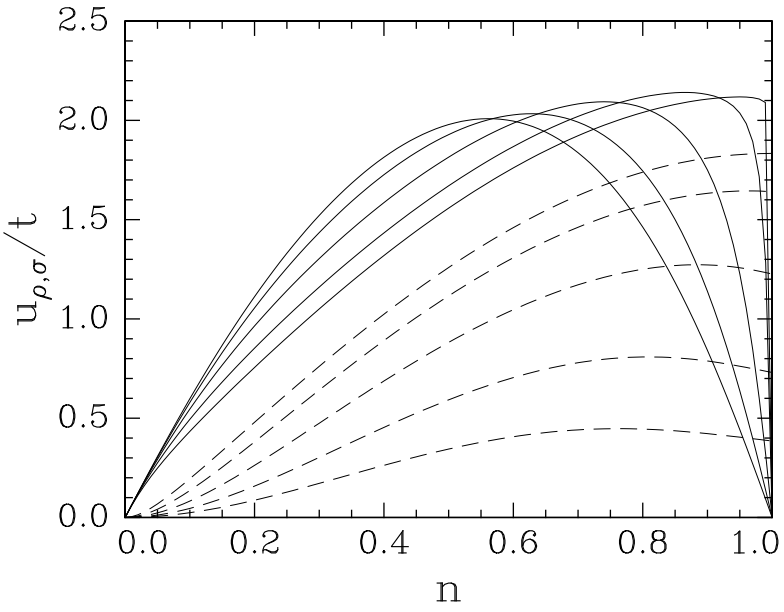

Figure 5.1: Dependence of the Luttinger velocity parameters u_ρ and u_σ on the mean particle density n (5.12) and the Hubbard on-site interaction U. The charge velocity u_ρ is given by the solid lines for $U = 16$, 8, 4, 2, 1 from top to bottom in the very left part of the figure. The spin velocity u_σ for $U = 1$, 2, 4, 8, 16 is given by the dashed line curves from top to bottom. Taken from [33].

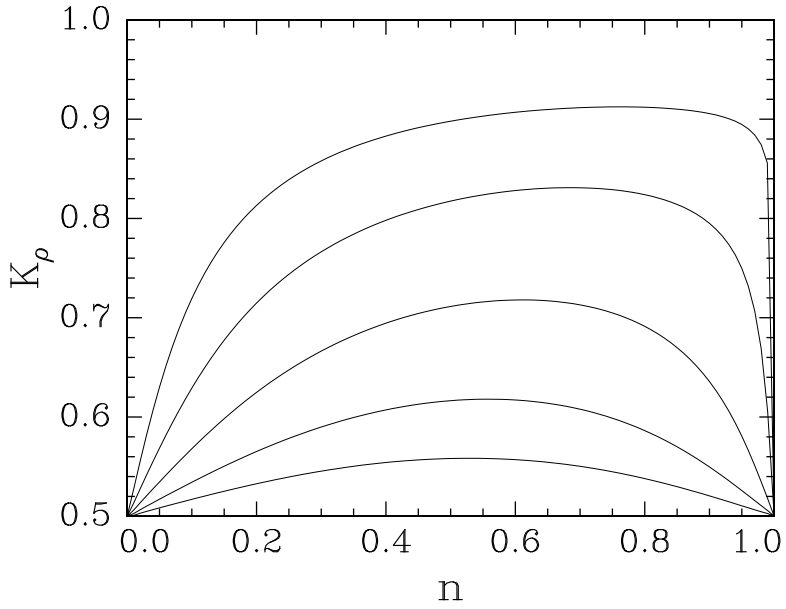

Figure 5.2: Dependence of the Luttinger parameter K_ρ on the mean particle density n (5.12) and the Hubbard on-site interaction U. The curves are for $U = 1$, 2, 4, 8, 16 from top to bottom. Taken from [33].

5.3.1 Andreev-like Reflection

The Andreev reflection occurs at a metal - superconductor boundary, when an incident electron hits the boundary and a hole is reflected. The electron has to form a pair in the superconductor. Conservation laws then require a hole to be reflected. A similar effect has been shown analytically by Safi and Schulz [34, 35, 36] to exist in an inhomogeneous Luttinger liquid for *weak* perturbations, although there is no metal-superconductor boundary but an interaction boundary, this effect is known as Andreev-like reflection [37]. An interaction boundary at a site x_B splits the system into two parts with different interaction strengths. In the inhomogeneous Luttinger liquid the parameters of equation (5.10) depend on the spatial coordinate x. The interaction strength to the right of the interaction boundary is different from the interaction strength to the left. If we denote the parameter K on the left hand side of the barrier with K_L and the parameter on the right with K_R the reflection coefficient γ is given by:

$$\gamma = \frac{K_L - K_R}{K_L + K_R} \tag{5.11}$$

This is the reflection coefficient for a particle density perturbation in a spinless model. It is also valid for spinful fermions for charge and spin separately: $K_L = K_{\nu,L}$ and $K_R = K_{\nu,R}$ with $\nu = \rho, \sigma$. [35]

A negative reflection coefficient means Andreev-like reflection. Then an incident propagating density perturbation splits into a reflected negative perturbation and a transmitted, amplified perturbation at the interaction boundary.

Numerical simulations using tDMRG for spinless fermions with nearest-neighbour interactions (section 5.1) were done by Daley, Zoller and Trauzettel in [37]. They suggest that the Andreev-like reflection could be observed using cold atoms in an optical 1D lattice. Optical lattices allow the engineering of systems that are accurately described by the model Hamiltonians that are used in the field of strongly correlated systems. In these experimental setups interaction parameters are tunable over a wide range. It is suggested that an initial perturbation is created using a laser beam focused over about ten sites, thus creating a Gaussian shaped deviation in the particle density. Their numerical results show that this perturbation splits into two propagating wave packets and is reflected at an interaction boundary. This reflection can be particle- or hole-/Andreev-like. Thus they showed that the predicted Andreev-like reflection does indeed exist outside of the idealised Luttinger liquid and with strong perturbations. In section 6.2 I use the TEBD implementation presented in section 4.5 to verify the results of their simulations.

For fermions with spins the same reflection coefficient is expected for charge perturbations. Since the coefficient K_σ is always equal to 1 for the Hubbard model, no reflection for spin density perturbations should occur. Simulations for spinful fermions can be found in section 6.3.

By looking at the graphs (Fig. 5.1, fig. 5.2) [33] that show the dependence of the Luttinger parameters on the Hubbard parameters and the mean particle density (filling factor)

$$n = \frac{N}{L} \qquad N = N_\uparrow + N_\downarrow \qquad (N_\uparrow = N_\downarrow), \tag{5.12}$$

one can anticipate the parameter ranges, where Andreev-like reflection is observable. For the repulsive Hubbard model, Andreev-like is expected for the transition from a region with strong on-site repulsion to a region with weak on-site repulsion. This can be seen by looking at the U-dependence of the Luttinger parameter K_ρ (fig. 5.2) and equation (5.11).

In the spinless fermion case Andreev-like reflection occurs for a transition from a region with large nearest-neighbour interaction V to a region with smaller interaction. An example would be going from no or repulsive nearest-neighbour interaction to a region with attractive interaction [37].

Chapter 6

Simulations

The simulations in this section show some applications of the TEBD algorithm to interacting fermions in one dimension. They illustrate the effects of propagation of density perturbations, spin-charge separation and Andreev-like reflection as presented in chapter 5.

The initial perturbations are created by calculating the ground state with imaginary time evolution ("cooling to T=0"). The Hamiltonians used include external fields which are electric field/chemical potential like and magnetic field like (if spin is also included, $\hat{H}_0$ is then (5.4)):

$$\hat{H} = \hat{H}_0 + \hat{H}_{\text{ext}} \tag{6.1}$$

$$\hat{H}_{\text{ext}} = \sum_{i=1}^{L} \epsilon_i (\hat{n}_{i\uparrow} + \hat{n}_{i\downarrow}) \; - \; \sum_{i=1}^{L} \frac{B_i}{2} (\hat{n}_{i\uparrow} - \hat{n}_{i\downarrow}) \tag{6.2}$$

For spinless fermions we just have:

$$\hat{H}_0 = -t \; \sum_{i=1}^{L-1} (c_i^\dagger c_{i+1} + c_{i+1}^\dagger c_i) + \sum_{i=1}^{L-1} V_i \; \hat{n}_i \hat{n}_{i+1} \tag{6.3}$$

$$\hat{H}_{\text{ext}} = \sum_{i=1}^{L} \epsilon_i \; \hat{n}_i \tag{6.4}$$

Thus one can create a local increase or decrease in particle density. With an additional magnetic field one can create an excess or depletion of one spin species. By setting $\epsilon_i = \pm \frac{B_i}{2}$ one can create a field which couples only to one spin species. The external fields were chosen to have a Gaussian shape.
In the next expression f can be an electric (ϵ) or a magnetic (B) field:

$$f_i = f_0 \exp\left(-\frac{(i - x_0)^2}{2\sigma^2} \right) \qquad f = \epsilon, B \tag{6.5}$$

f_0 ($= \epsilon_0$ or B_0) is the peak field strength at site x_0. σ determines the width of the Gaussian field. After the ground state is reached, the external fields are switched off at $t = 0$. That means that the real time evolution is performed with the Hamiltonian $\hat{H}_0$. Because of the local imbalance in the particle density that was created, equilibration processes lead to the propagation of the perturbation. This can be observed by measuring the expectation values of the charge density (5.5) and the spin density (5.6) at each site.

One would expect that an arbitrary perturbation of the ground state particle density would have components that travel at various different velocities. In the idealised Luttinger-model, however, only one velocity (group velocity) should occur (one each for charge and spin), because of the linear energy-momentum relation. In numerical studies of spinless fermions and the Hubbard model, a Gaussian-shaped density perturbation has proven to be quite stable after splitting into two components. These components travel in opposite directions with a group velocity that is equal to the Luttinger parameters u_ν ($\nu = \rho,\ \sigma$), calculated using the local interaction and particle density [32]. The splitting of the initial perturbation is explained by conservation of (pseudo-)momentum.

6.1 Spin-Charge Separation

The decoupling of the Hamiltonian in (5.9) means that charge and spin are completely separate degrees of freedom. This effect is known as *spin-charge separation*. This means that a description of fermionic quasi-particles carrying spin and charge does not apply in one dimension.

Real-time studies of spin-charge separation with the adaptive tDMRG algorithm can be found in [38, 32]. In these papers charge- and spin-velocity were determined by creating fairly large density perturbations. The charge velocity agreed well with the theoretical prediction in figure 5.1, if the mean particle density n (5.12) was set equal to the peak density of the initial perturbation. The authors of the cited papers found the spin velocity to be strongly dependent on the amplitude of the perturbation, which they explained by an indirect coupling to the charge degrees of freedom, resulting from the initial field configuration used. Another numerical study of spin-charge separation can be found in [39].

I will also present similar studies calculated with TEBD in this section *using only very weak fields*. The basis of these simulations on a one-dimensional lattice is the Hubbard model (5.4).

The initial perturbation was created as described in the beginning of this chapter. In (6.5) one sets $f = \epsilon$ for a chemical potential / electric field like

term and $f = B$ for a magnetic field term. The important parameters are then: ϵ_0 is the peak electrical field strength and B_0 the peak magnetic field. The parameter σ in (6.5) determines the width of the applied Gaussian fields.

The plots in this section show charge/spin density expectation values minus a background density (l is the site index, ν stands for charge or spin):

$$\langle \hat{n}_l^\nu \rangle(t) - \langle \hat{n}_l^\nu \rangle_{\substack{\epsilon_0=0 \\ B_0=0}} \qquad \nu = \rho,\, \sigma \tag{6.6}$$

Here the background density expectation values $\langle \hat{n}_l^\nu \rangle_{\substack{\epsilon_0=0 \\ B_0=0}}$ are calculated from the ground state of the system without external fields. Furthermore the spin density was averaged over 3 sites to smooth out oscillations.

For non-interacting ($U = 0$) fermions spin- and charge velocity are the same. This is shown in figures 6.1 and 6.2 for $N_\uparrow = N_\downarrow = 28$, which gives a mean particle density (5.12) of $n \approx 0.78$.

For interacting fermions ($U = 4$), however, spin- and charge velocity are clearly different: Figure 6.3 and figure 6.4. Figure 6.5 and figure 6.6 show the same situation for $n = 0.5$. For a mean particle density of $n \approx 0.22$ no clear propagation is visible in this setup (especially for the spin): Figure 6.7 and figure 6.8.

The numerical results suggest that the perturbation propagates with the characteristic velocities u_ρ, u_σ of an *infinitesimally* weak density perturbation from (5.10). According to the graphs in figure 5.1 [33], where u_ρ and u_σ are plotted versus n, different particle densities lead to different velocities.

The peak field strengths $\epsilon_0 = -0.1$ and $B_0 = 0.2$, where chosen to create only a weak perturbation, such that a propagation with the characteristic velocities is visible more clearly. If a strong perturbation is created, local imbalances of spin-up and spin-down particle densities extending over a few sites couple spin and charge degrees of freedom and lead to the breakdown of spin-charge separation. This is also observed when $N_\uparrow \neq N_\downarrow$ [32].

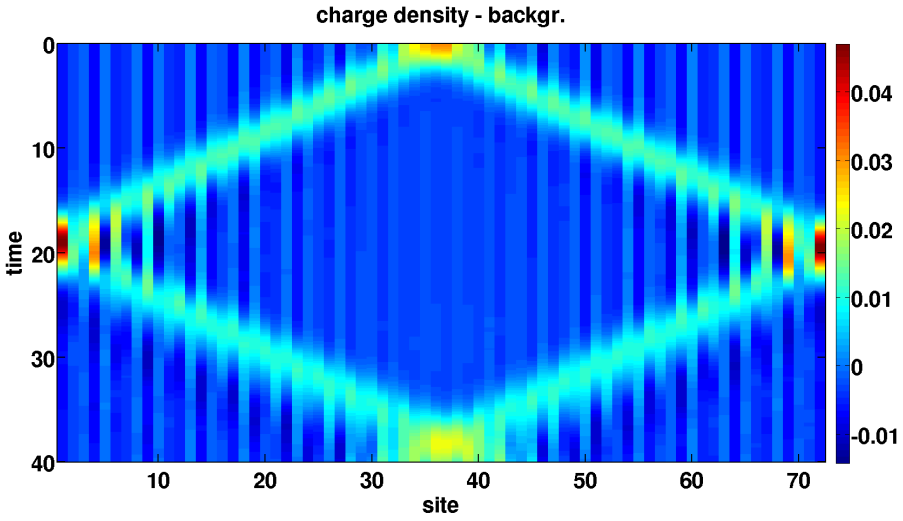

Figure 6.1: Non-interacting fermions. Propagation of a density perturbation: *Charge density* (colour), $\mathbf{U = 0}$, $L = 72$, $N_\uparrow = N_\downarrow = 28$, $\mathbf{n \approx 0.78}$, $\epsilon_0 = -0.1$, $B_0 = 0.2$, $x_0 = 35$, $M = 80$, $\tau = 0.02$, background subtracted

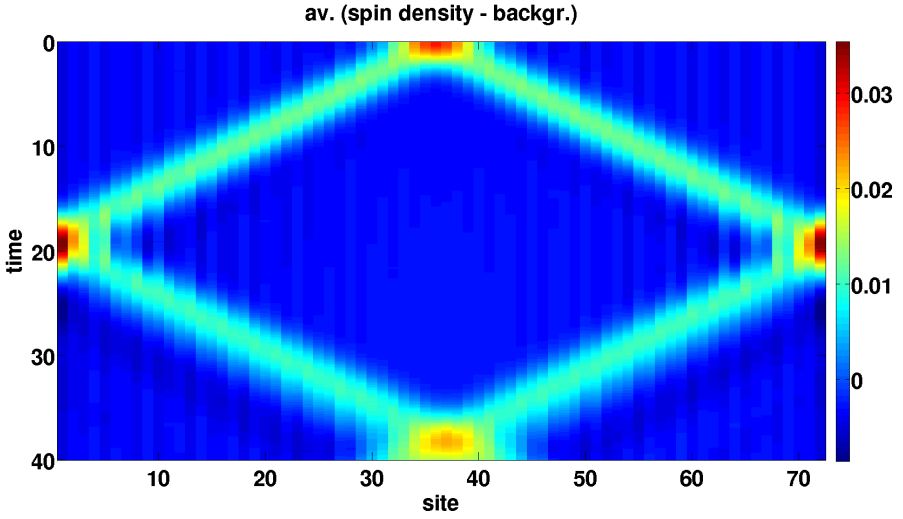

Figure 6.2: Non-interacting fermions. Propagation of a density perturbation: *Spin density* (colour), $\mathbf{U = 0}$, $L = 72$, $N_\uparrow = N_\downarrow = 28$, $\mathbf{n \approx 0.78}$, $\epsilon_0 = -0.1$, $B_0 = 0.2$, $x_0 = 35$, $M = 80$, $\tau = 0.02$, 3-site-average, background subtracted

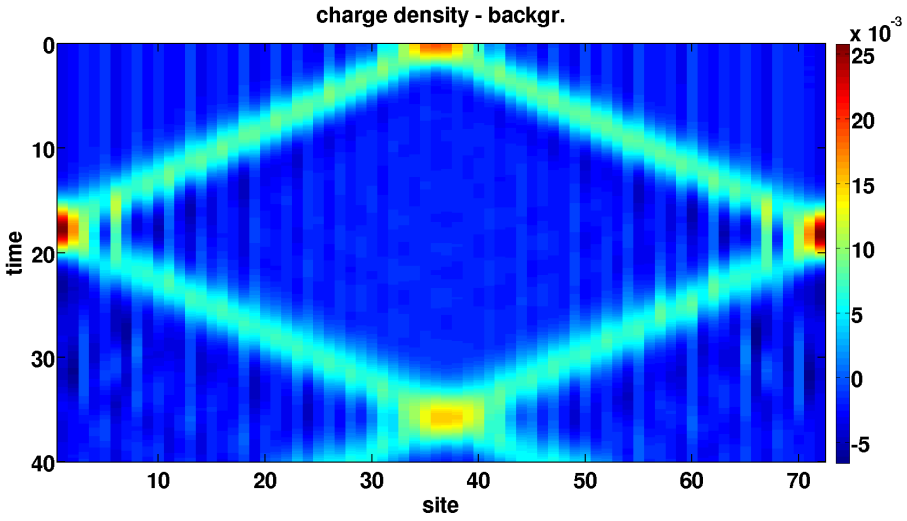

Figure 6.3: Interacting fermions. Propagation of a density perturbation: *Charge density* (colour), $\mathbf{U = 4}$, $L = 72$, $N_\uparrow = N_\downarrow = 28$, $\mathbf{n \approx 0.78}$, $\epsilon_0 = -0.1$, $B_0 = 0.2$, $x_0 = 35$, $M = 80$, $\tau = 0.02$, background subtracted

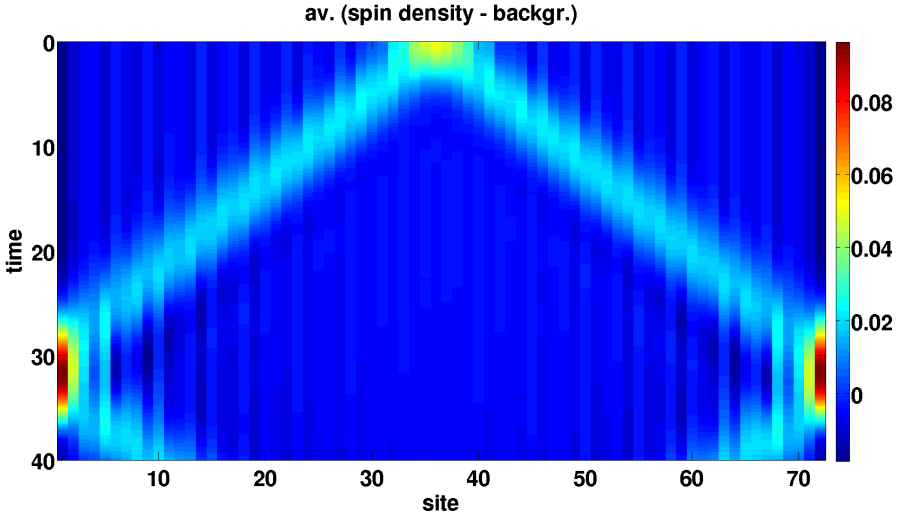

Figure 6.4: Interacting fermions. Propagation of a density perturbation: *Spin density* (colour), $\mathbf{U = 4}$, $L = 72$, $N_\uparrow = N_\downarrow = 28$, $\mathbf{n \approx 0.78}$, $\epsilon_0 = -0.1$, $B_0 = 0.2$, $x_0 = 35$, $M = 80$, $\tau = 0.02$, 3-site-average, background subtracted

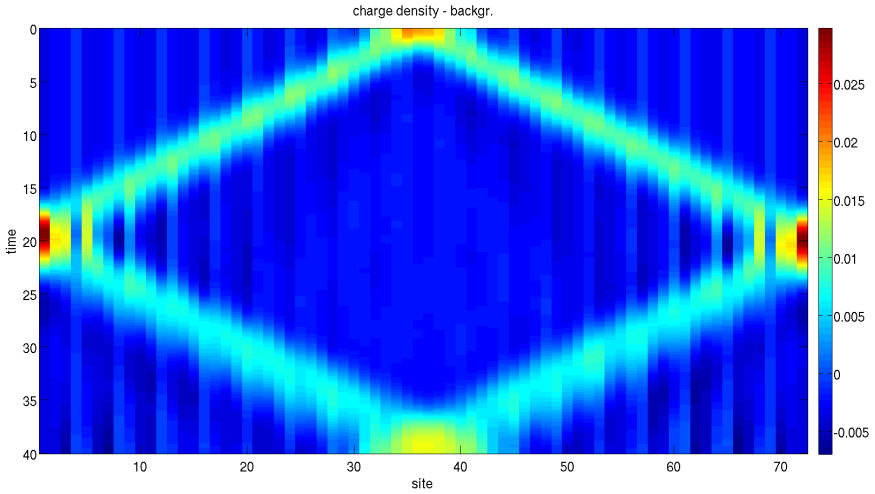

Figure 6.5: Propagation of a density perturbation: *Charge density* (colour), $\mathbf{U = 4}$, $L = 72$, $N_\uparrow = N_\downarrow = 16$, $\mathbf{n = 0.5}$, $\epsilon_0 = -0.1$, $B_0 = 0.2$, $x_0 = 35$, $M = 80$, $\tau = 0.02$, background subtracted

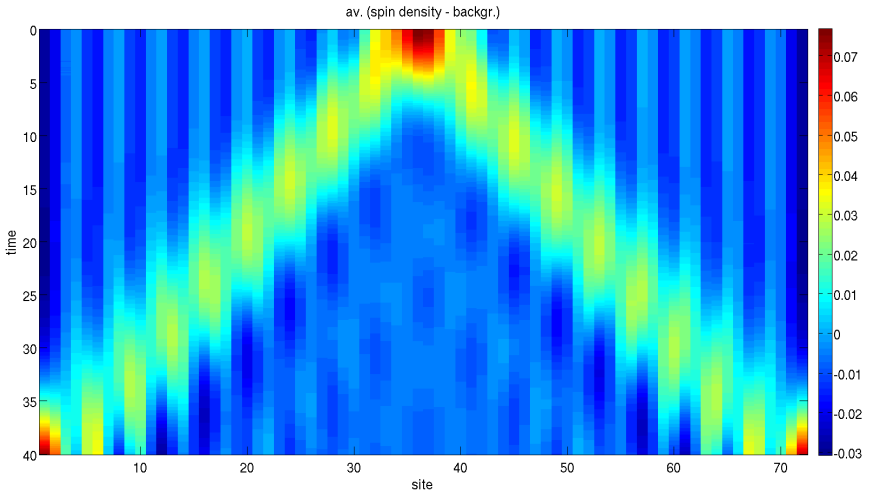

Figure 6.6: Propagation of a density perturbation: *Spin density* (colour), $\mathbf{U = 4}$, $L = 72$, $N_\uparrow = N_\downarrow = 16$, $\mathbf{n = 0.5}$, $\epsilon_0 = -0.1$, $B_0 = 0.2$, $x_0 = 35$, $M = 80$, $\tau = 0.02$, 3-site-average, background subtracted

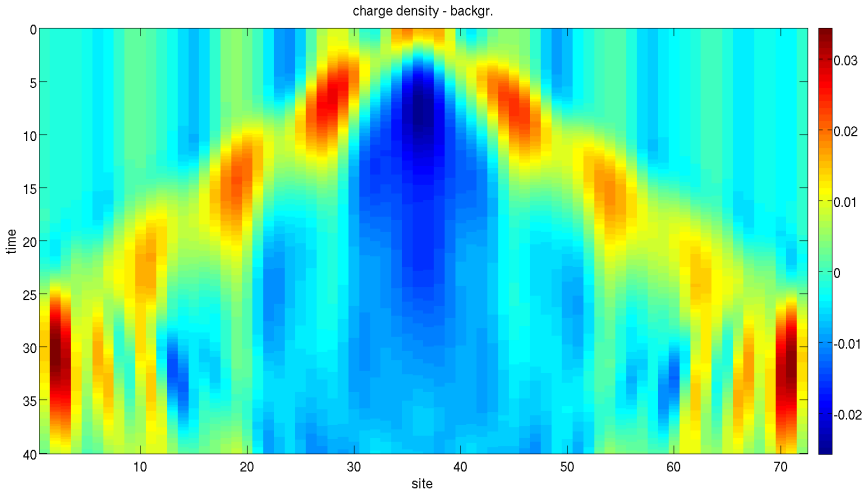

Figure 6.7: Propagation of a density perturbation: *Charge density* (colour), $\mathbf{U = 4}$, $L = 72$, $N_\uparrow = N_\downarrow = 8$, $\mathbf{n \approx 0.22}$, $\epsilon_0 = -0.1$, $B_0 = 0.2$, $M = 80$, $\tau = 0.02$, background subtracted

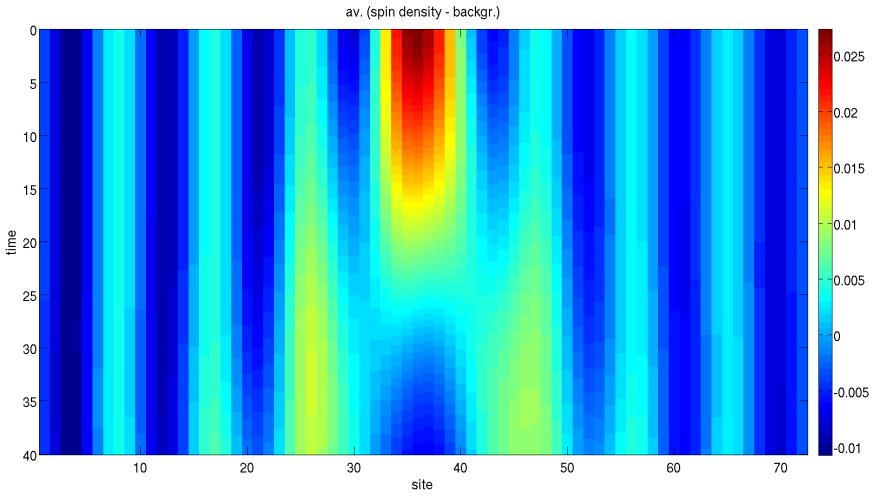

Figure 6.8: Propagation of a density perturbation: *Spin density* (colour), $\mathbf{U = 4}$, $L = 72$, $N_\uparrow = N_\downarrow = 8$, $\mathbf{n \approx 0.22}$, $\epsilon_0 = -0.1$, $B_0 = 0.2$, $M = 80$, $\tau = 0.02$, 3-site-average, background subtracted

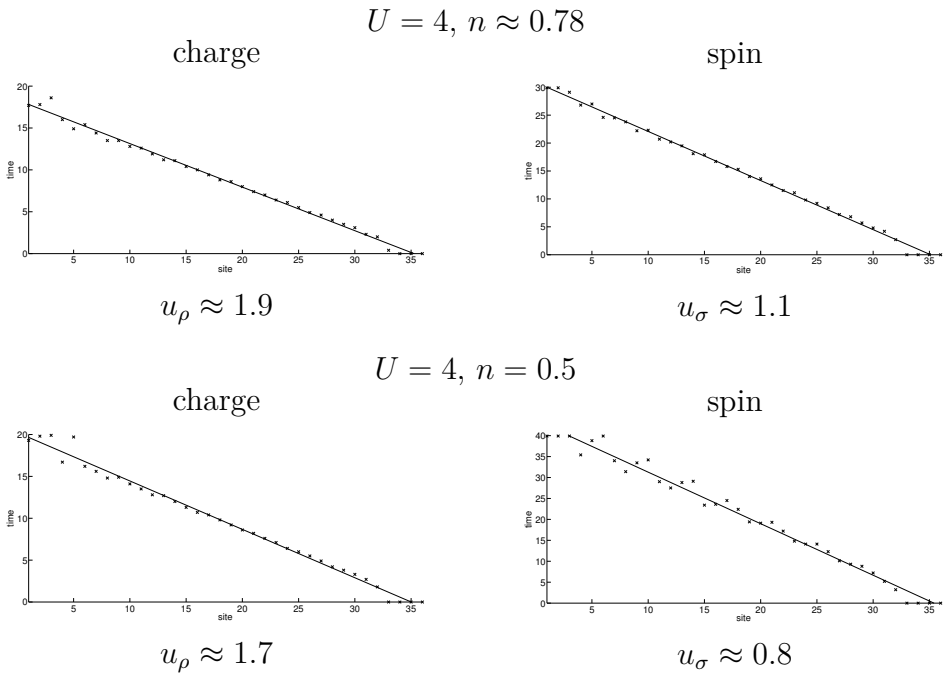

Figure 6.9: Spin-charge separation: Calculation of charge and spin velocities. The positions of the density maxima in space and time are plotted. A linear fit allows the estimation of the velocities.

Velocities. Velocities can be estimated using the propagation of the maximum of the wave packet. For each site the density maximum is determined. If one plots the positions of the maxima in time versus the positions in space and performs a linear fit, the velocity can be calculated. It is given by the inverse of the slope. Figure 6.9 shows calculations for $U = 4$ and densities $n \approx 0.78$, $n = 0.5$. For this parameters the propagation was clearly visible. The calculated velocities are given in the figure. For the weak perturbations that were applied here, we have good agreement with the theoretical results (fig. 5.1) for the charge velocity and for the spin velocity as well.

6.2 Andreev-like Reflection for Spinless Fermions

This section deals with Andreev-like reflection in a spinless fermion model with Hamiltonian (5.1). Thereby a verification of the results in [37] is given. The parameters were chosen according to the cited paper. Other parameters such as the chemical potential term ϵ_R, the matrix dimension M and the timestep τ were not specified in [37] and had to be selected appropriately. Additionally I compared calculations with different matrix dimension and calculated the entanglement entropy.

To include an interaction boundary at site x_B we set in (5.1):

$$V_i = \begin{cases} V_L & i < x_B \\ V_R & i \geq x_B \end{cases} \tag{6.7}$$

This separates the system into two regions with different nearest-neighbour interactions.

The perturbation was created as described in the beginning of chapter 6 using Gaussian shaped fields and cooling to the ground state. Then the parameters that determine the perturbation are ϵ_0 and σ (see (6.5)). After cooling to the ground state, more particles will have accumulated in the region with less repulsive interaction. To compensate one can add an additional chemical potential like term to the Hamiltonian, where the parameter ϵ_R is determined by trial-and-error until the average density in both interaction regions is about the same:

$$\hat{H} \to \hat{H} + \sum_{i \geq x_B} \epsilon_R \, \hat{n}_i \tag{6.8}$$

As we are considering only spinless fermions, magnetic field terms are not included and the spin density is not an observable of interest. The field is switched off at $t = 0$ and the perturbation propagates. No background density was substracted for the following simulations in contrast to the spin-charge separation simulations.

Normal Reflection

For the parameters $V_L = 0$, $V_R = 1$ and an interaction boundary at $x_B = 91$, we get normal (positive) reflection in a system with 128 sites and $N = 56$ particles. Figure 6.10 shows the particle density expectation value $\langle \hat{n}_i \rangle$ as grayscale. The shading of the plot is derived from a linear interpolation between the minimum (black) and the maximum value (white). The perturbation parameters are $\epsilon_0 = -2$, $\sigma = 3$, $x_0 = 45$. Other parameters are given in the figure caption. Figure 6.11 shows the same situation as 3 axes plot.

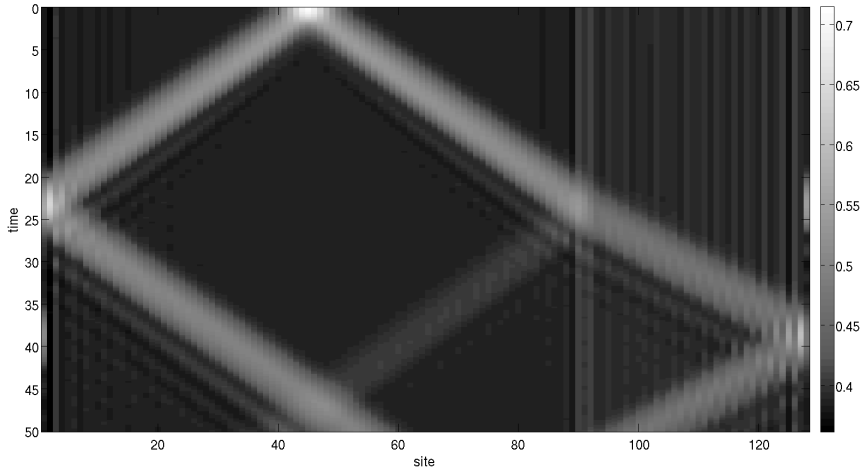

Figure 6.10: Spinless fermions: Normal reflection at an interaction boundary at site $x_B = 91$: particle/charge density (grayscale); $V_L = 0$, $V_R = 1$, $L = 128$, $N = 56$, TEBD calculation, approximately equal particle densities in left and right half, $\epsilon_0 = -2$, $\sigma = 3$, $x_0 = 45$, $\epsilon_R = -0.6$, $M = 80$, $\tau = 0.05$

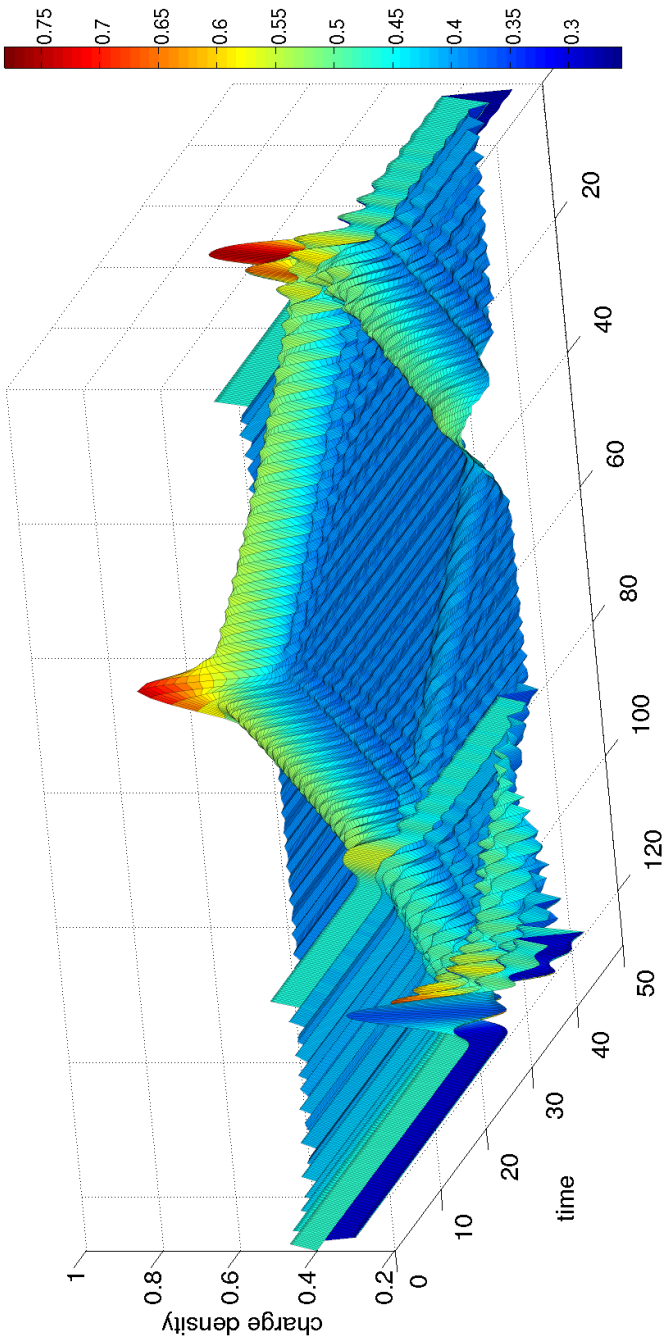

Figure 6.11: Spinless fermions: Normal reflection. $V_L = 0$, $V_R = 1$, parameters as in figure 6.10, 3 axes plot

To get an estimate for the reliability of the simulation, we can calculate the absolute difference in the particle densities for a calculation with $M = 200$ and calculations with lower matrix dimension ($M = 80$ and $M = 160$). The ground state was calculated at $M = 80$ and the matrix dimension increased for the real time evolution when desired. Figure 6.12 shows the result by plotting $|\langle\hat{n}_i(t)\rangle_{M=80} - \langle\hat{n}_i(t)\rangle_{M=200}|$ and $|\langle\hat{n}_i(t)\rangle_{M=160} - \langle\hat{n}_i(t)\rangle_{M=200}|$. The maximal difference for $M = 80$ is 1.9×10^{-3} and for $M = 160$ it is 2.8×10^{-4}.

Furthermore the maximal truncated weight $w_{\max}$ between two measurement steps at times $t - m\tau$ and t is plotted over time in figure 6.13 and compared between $M = 80$, $M = 160$ and $M = 200$. Here m is the number of time steps after which a measurement step is performed. Our measure for the truncated weight is then given by: ($w_i(s)$ is the truncated weight for the operator application on sites i and $i + 1$ at time s):

$$w_{\max}(t) = \max_{s\in[t-m\tau,t]} \max_i w_i(s) \tag{6.9}$$

We see that a higher matrix dimension leads to a reduction of the truncated weight. One can also notice that the truncated weight increases sharply at the time when the perturbation hits the boundary.

It is insightful to study the time evolution of the entanglement entropy, which serves as a measure of bipartite entanglement. For a certain point in time, one can calculate the entanglement entropy between the two parts, which result from cutting the bond between site l and site $l + 1$. It is given by (see (2.8), (2.9)):

$$S_l = -\sum_{\alpha=1}^{M} \left(\lambda_\alpha^{[l]}\right)^2 \ln\left(\lambda_\alpha^{[l]}\right)^2 \tag{6.10}$$

The choice of the logarithm base is in principle arbitrary, here the natural log-base is used. Figure 6.14 shows the situation for a cut of the bond between site 90 and site 91. This is the location of the interaction boundary. We notice an increase of entanglement entropy when the perturbation hits the boundary thus creating more entanglement between both parts of the system. One also notices that a matrix dimension of $M = 160$ or $M = 200$ preserves slightly more entanglement entropy than a dimension of $M = 80$. Furthermore there is only little difference between $M = 160$ and $M = 200$.

In figure 6.15 one sees the entanglement entropy for cuts at each bonds, calculated at $M = 200$, which is the highest matrix dimension used in this series of calculations.

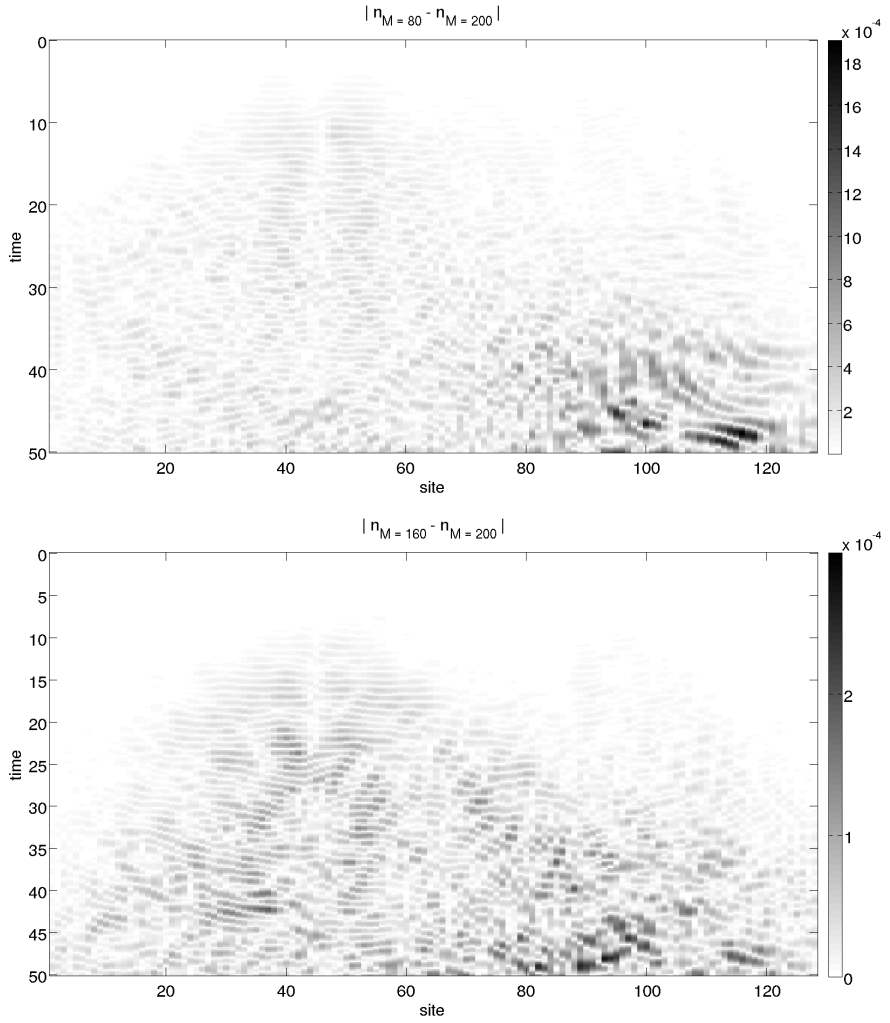

Figure 6.12: Spinless fermions: Normal reflection, $V_L = 0$, $V_R = 1$; Absolute difference in the particle density between calculation with $M = 80$ and calculation with $M = 200$ (top); difference between $M = 160$ and $M = 200$ (bottom)

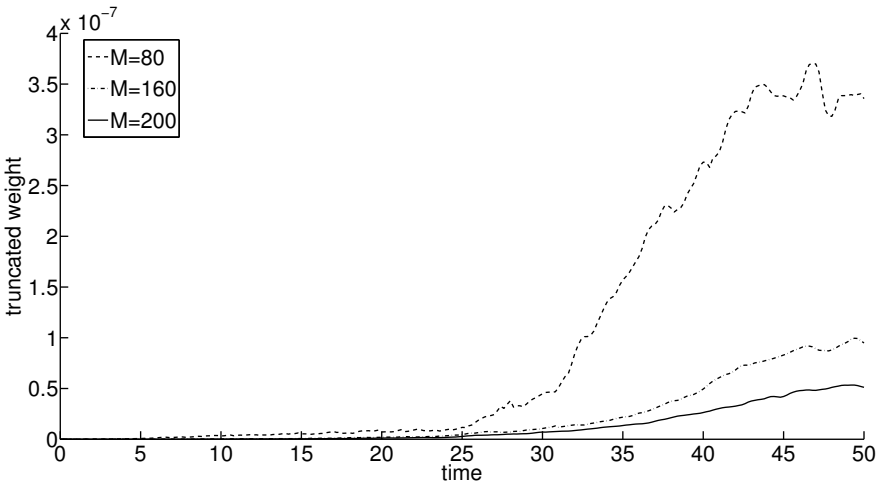

Figure 6.13: Spinless fermions: Normal reflection. Evolution of the truncated weight (6.9): Comparison between $M = 80$ (dashed line), $M = 160$ (dash-dot line) and $M = 200$

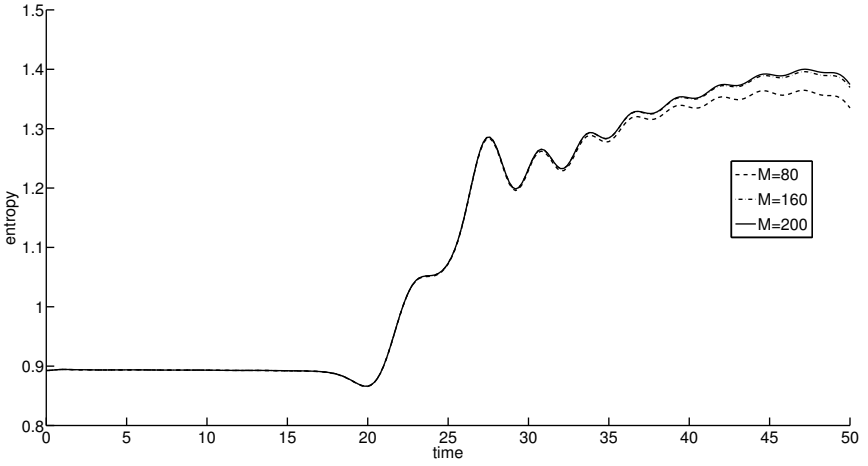

Figure 6.14: Spinless fermions: Normal reflection. Entanglement entropy for a cut between site 90 and 91 (location of interaction boundary): time dependence for $M = 80$ (dashed line), $M = 160$ (dash-dot line) and $M = 200$; (natural log-base)

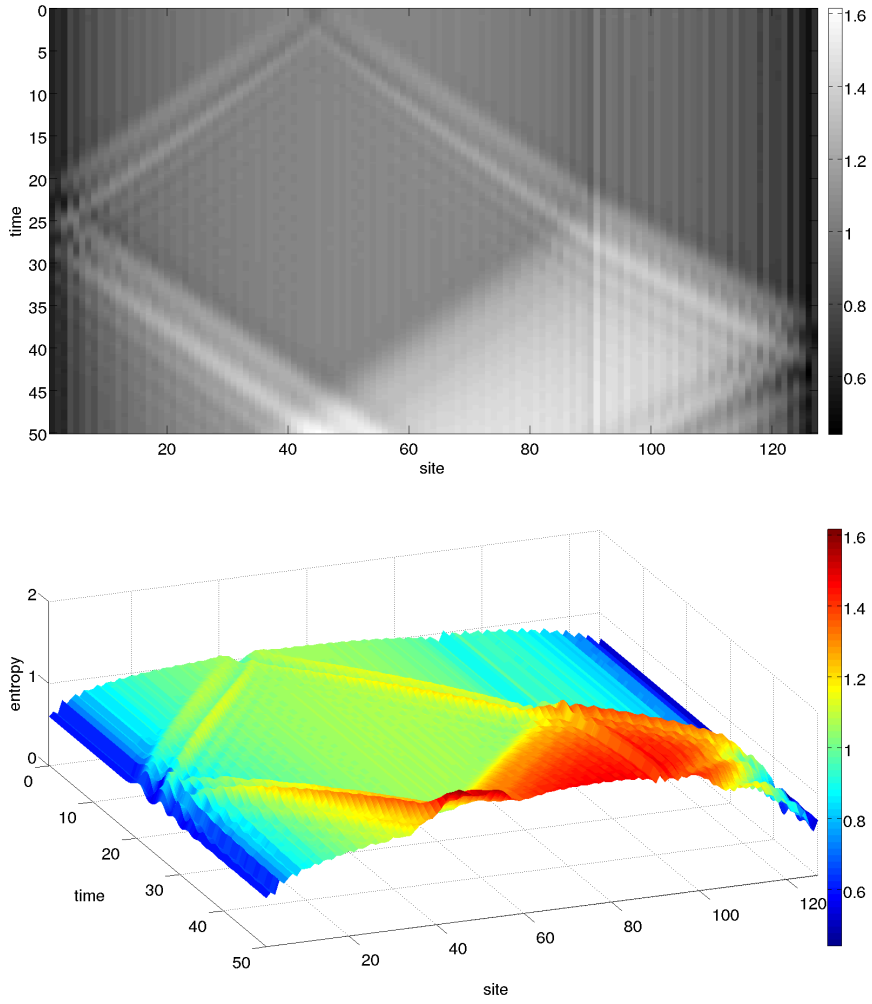

Figure 6.15: Spinless fermions: Normal reflection. Evolution of the entanglement entropy (top: grayscale, bottom: 3 axes) for cuts between site and site+1; $M = 200$

Andreev-like Reflection

Andreev-like reflection is observed when $V_R = -1$, which means an attractive nearest-neighbour interaction. It is visible in figure 6.16 as a dark reflected stripe after the perturbation hits the boundary around $t = 22$. Figure 6.17 shows a three axes plot of the same situation, which also gives a better idea of the propagation of the density perturbation. These simulations are a verification of the results in [37].

The differences in the particle densities between calculations with $M = 80$, $M = 160$ and $M = 200$ are shown in figure 6.18. The maximal difference for $M = 80$ is 1.8×10^{-3} and for $M = 160$ it is 6.8×10^{-4}. For the evolution of the truncated weight (6.9) see figure 6.19. The time dependence of the entanglement entropy for a cut at the interaction boundary is depicted in figure 6.20. We see that more entanglement is present than in the simulation of the normal reflection. Figure 6.21 shows the entanglement entropy evolution for each cut at $M = 200$.

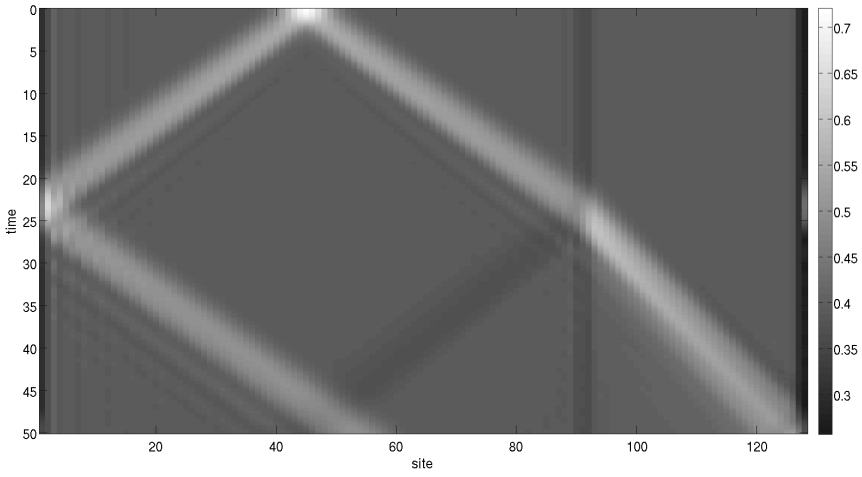

Figure 6.16: Spinless fermions: Andreev/Hole-like reflection at an interaction boundary at site $x_B = 91$: particle/charge density (grayscale); $V_L = 0$, $V_R = -1$, $L = 128$, $N = 56$, TEBD calculation, approximately equal particle densities in left and right half, $\epsilon_0 = -2$, $\sigma = 3$, $x_0 = 45$, $\epsilon_R = 0.6$, $M = 80$, $\tau = 0.05$

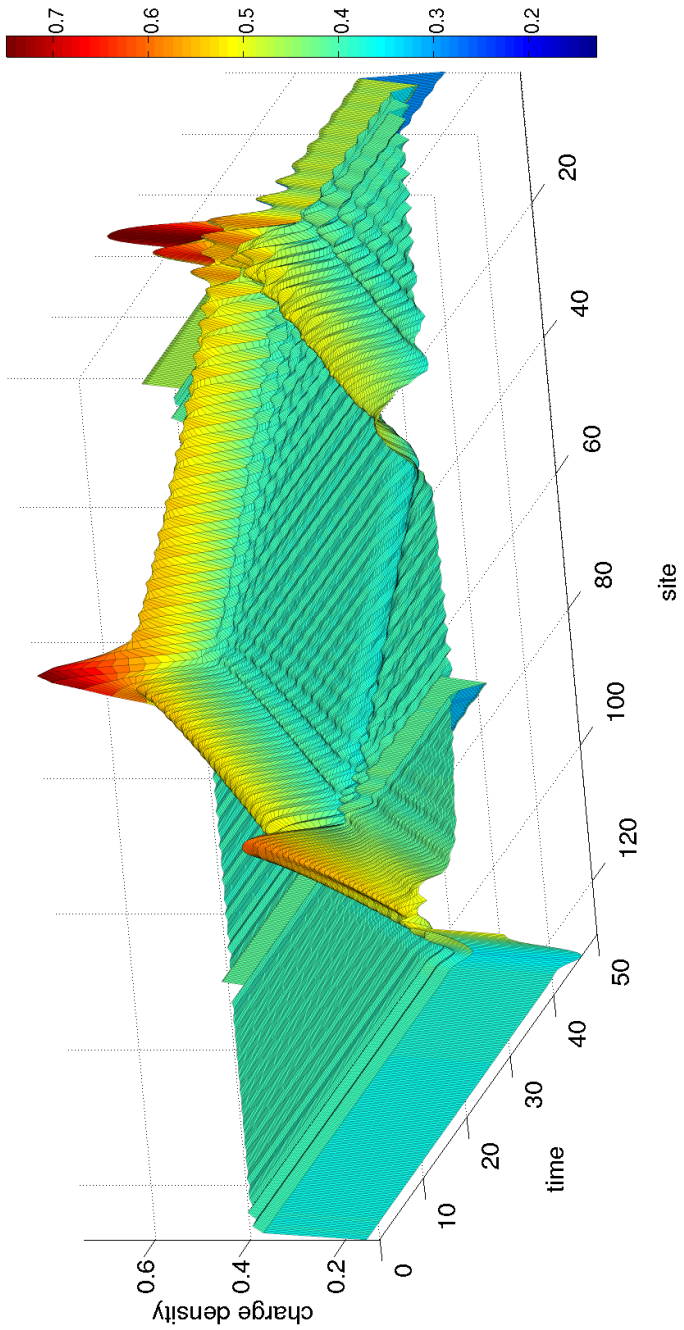

Figure 6.17: Spinless fermions: Andreev/Hole-like reflection. $V_L = 0$, $V_R = -1$, same parameters as in figure 6.16, 3 axes plot

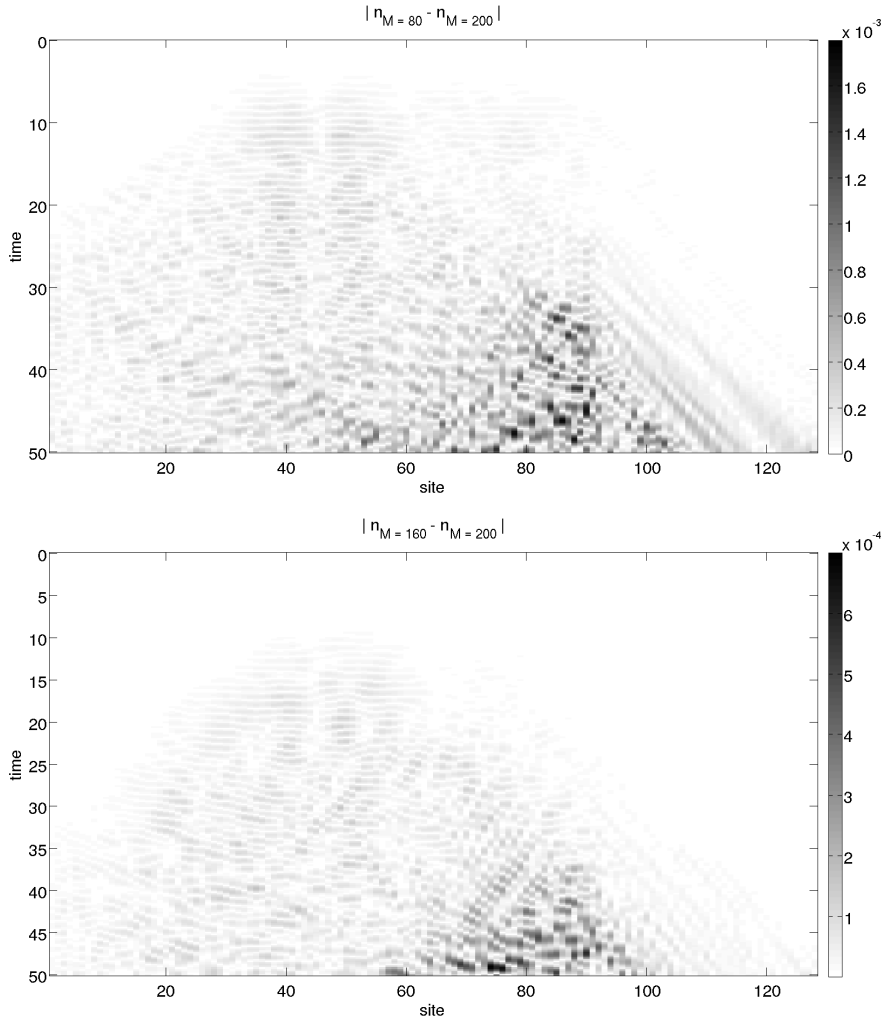

Figure 6.18: Spinless fermions: Andreev-like reflection, $V_L = 0$, $V_R = -1$; Absolute difference in the particle density between calculation with $M = 80$ and calculation with $M = 200$ (top); difference between $M = 160$ and $M = 200$ (bottom)

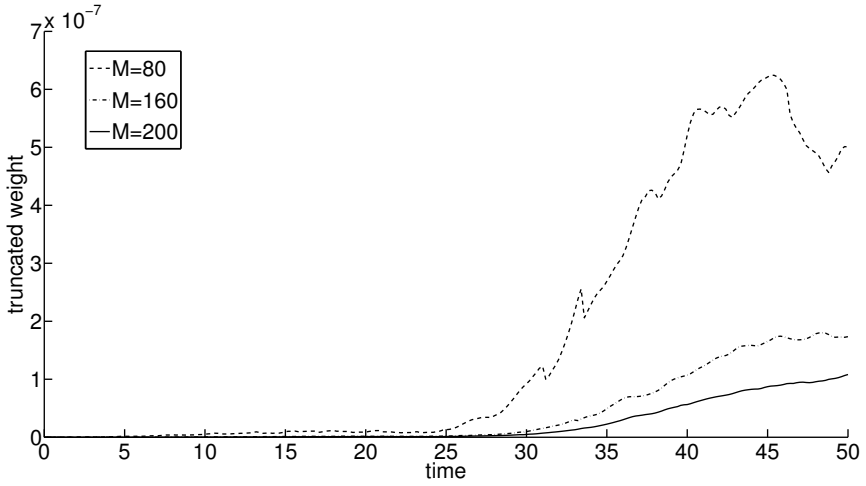

Figure 6.19: Spinless fermions: Andreev-like reflection. Evolution of the truncated weight (6.9): Comparison between $M = 80$ (dashed line), $M = 160$ (dash-dot line) and $M = 200$

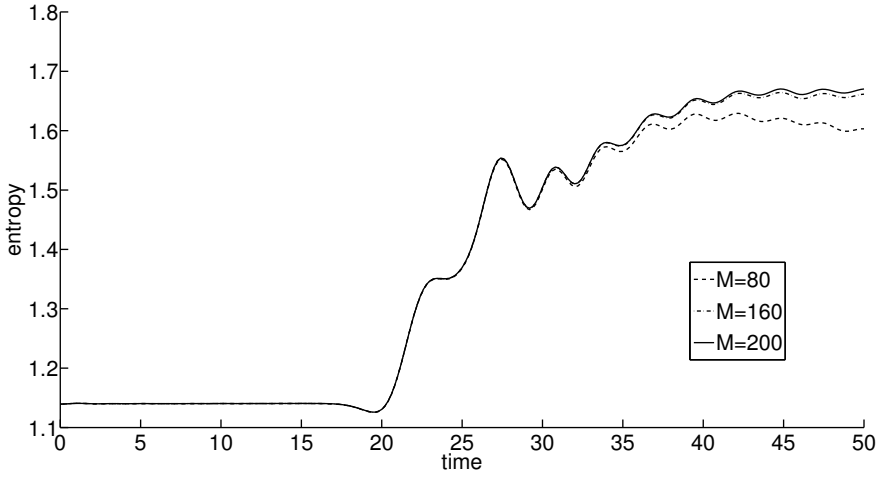

Figure 6.20: Spinless fermions: Andreev-like reflection. Entanglement entropy for a cut between site 90 and 91 (location of interaction boundary): time dependence for $M = 80$ (dashed line), $M = 160$ (dash-dot line) and $M = 200$; (natural log-base)

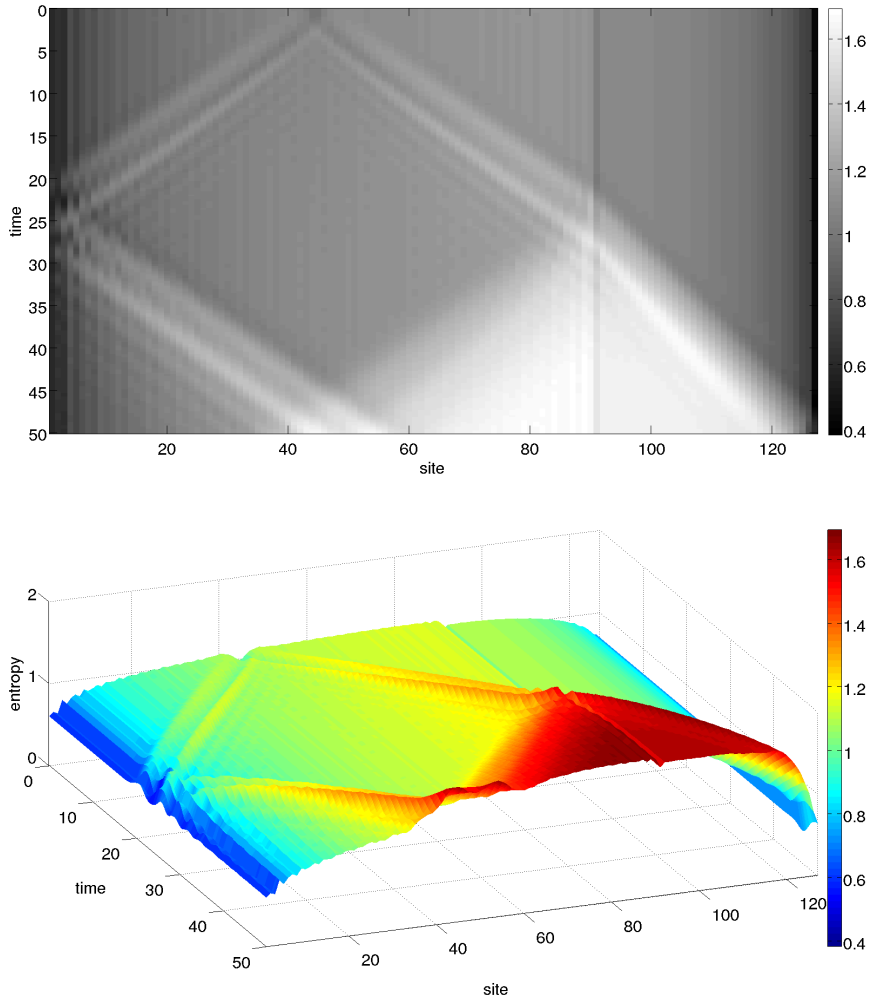

Figure 6.21: Spinless fermions: Andreev-like reflection. Evolution of the entanglement entropy (top: grayscale, bottom: 3 axes) for cuts between site and site+1; $M = 200$

6.3 Andreev-like Reflection for Fermions with Spin

When investigating Andreev-like reflections for fermions with spin, one sets (where x_B is the site of the interaction boundary)

$$U_i = \begin{cases} U_L & i < x_B \\ U_R & i \geq x_B \end{cases} \tag{6.11}$$

The Andreev-like reflection is a small effect that is often dominated by oscillations in the charge/spin density. These oscillations are induced by boundaries, such as the edges of the chain and where the interaction strength suddenly changes. Therefore the system size and the width of the initial Gaussian perturbation (6.5) have to be chosen appropriately: A large system size minimizes edge effects and allows for a clear separation into two regions with different interactions. Having included spin, one can now apply a magnetic field in addition to the chemical potential term. Choosing a sizeable width for the Gaussian shaped fields avoids abrupt changes of the interaction strength and gives a well shaped propagating wave packet. The preferred length of the chain is $L = 128$ and the width of the perturbation (6.5) is $\sigma = 3$. In contrast to the spin-charge separation calculations, no background was subtracted, since attempts to remove background oscillations did not yield more meaningful results.

On-site interactions: $U_L = 8$, $U_R = 0$

In the end of section 5.3.1 it was mentioned that hole-like reflections in the repulsive Hubbard model occur on a transition from strong to weak (or zero) on-site interaction. The goal of this section is to show that hole-like reflections also exist, when spin is taken into account.

The on-site interaction strength in the left half is chosen to be $U_L = 8$ and in the right half $U_R = 0$. This leads to different average particle densities in both halves. They were not compensated by an additional chemical potential as in the spinless case. For this parameter set I performed calculations with matrix dimensions $M = 80$ and $M = 160$.

The peak field strengths for creating the perturbation are $\epsilon_0 = -2$ and $B_0 = 0.05$ - the magnetic field was chosen to be much weaker than the electric field term. The magnetic field term was meant to create a propagating spin density wave packet. However, the spin density turned out to be not completely independent of the charge density. This is caused by the large perturbation of the charge density that is necessary to observe Andreev-like

reflection. (ϵ_0 is 20 times larger than in the spin-charge separation simulations.)

Andreev-like reflection in the Hubbard model: Figure 6.22 shows the charge and the spin density as grayscale plots. Figure 6.23 shows the same situation as 3-axes plot.

In figure 6.22 a) we see Andreev-like reflection in the charge density, which shows as a dark stripe (lower density) in the plot. The reflection is also visible in figure 6.23 a).

Compared to the background charge density, the negative reflection is a weak effect. Therefore it is useful to plot an "integrated charge density" versus time, as it suggested in [37]. Here it is calculated by averaging the charge density over sites 80 to 85. This gives us figure 6.24. The dip around $t \approx 18$ indicates negative reflection.

Due to different interactions, the mean particle density in the left part is $n_L \approx 0.43$ and in the right part $n_R \approx 0.68$. If we read off the value for $K_{\rho,L}$ (left part) from figure 5.2 we get roughly $K_{\rho,L} \approx 0.6$. In the right part $K_{\rho,R} = 1$ for non-interacting fermions ($U = 0$). With equation (5.11), we get a reflection coefficient $\gamma \approx -0.25$. By estimation, using the heights of the peaks in figure 6.24 minus the background, the reflection coefficient is $\gamma \approx -0.1$, which disagrees with the theoretical result.

The averaged/integrated spin density is plotted in figure 6.25. It is qualitatively different from the integrated charge density and not conclusive in terms of reflections. An explanation for the behaviour of the spin density is given in the section dealing with the next parameter set on page 85.

These results show that Andreev-like reflection in the charge density indeed exists in the *full* Hubbard model, using a similar strategy to the one established in [37]. In section 5.3.1 we saw that the idealised theory of the inhomogeneous Luttinger liquid predicts negative reflections in the charge density and no reflection in the spin density. As far as the charge density is concerned, the theoretical predictions are qualitatively confirmed.

Note that while the analytical results by Safi and Schulz [34, 35, 36] showed the existence of Andreev-like reflections for weak (infinitesimal) perturbations in the Luttinger liquid, these numerical results show that this effect also exists in the Hubbard model with *large* perturbations.

a)

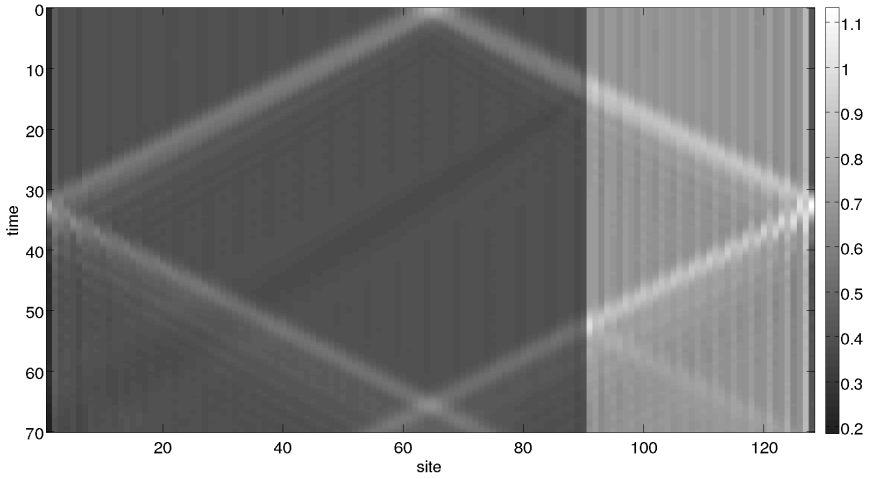

b)

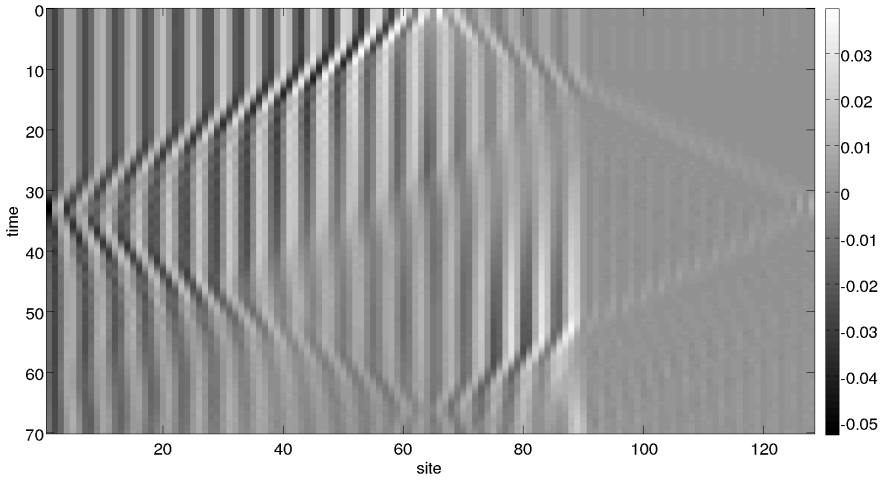

Figure 6.22: Fermions with spin: Andreev/Hole-like reflection at an interaction boundary at site $x_B = 91$: $U_L = 8$, $U_R = 0$; a) Charge density b) Spin density (grayscale); $L = 128$, $N_\uparrow = 32$, $N_\downarrow = 32$, $\epsilon_0 = -2$, $B_0 = 0.05$, $\sigma = 3$, $x_0 = 65$, $M = 160$, $\tau = 0.05$; $n_L \approx 0.43$, $n_R \approx 0.68$

a)

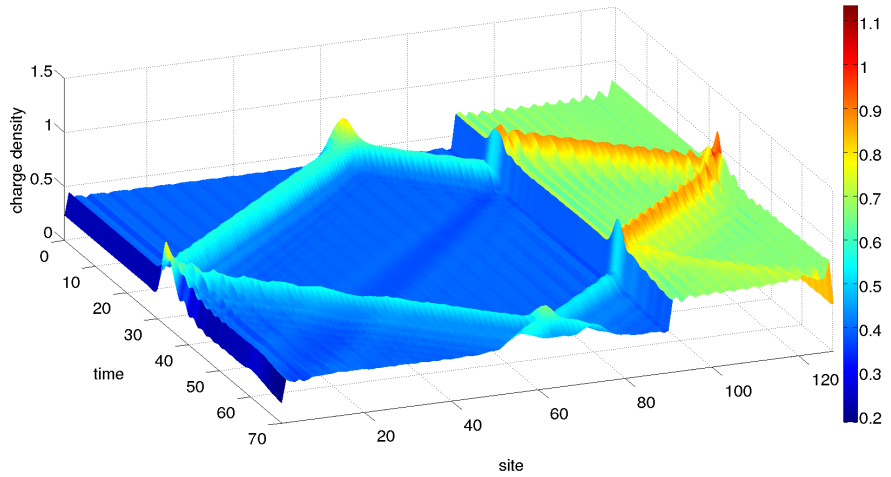

b)

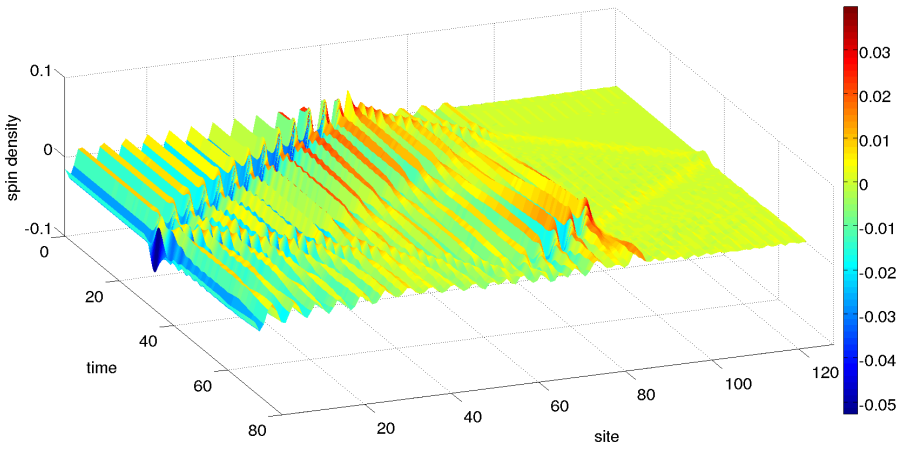

Figure 6.23: Fermions with spin: Andreev/Hole-like reflection. $U_L = 8$, $U_R = 0$; a) Charge density b) Spin density; same parameters as in figure 6.22; 3 axes plot

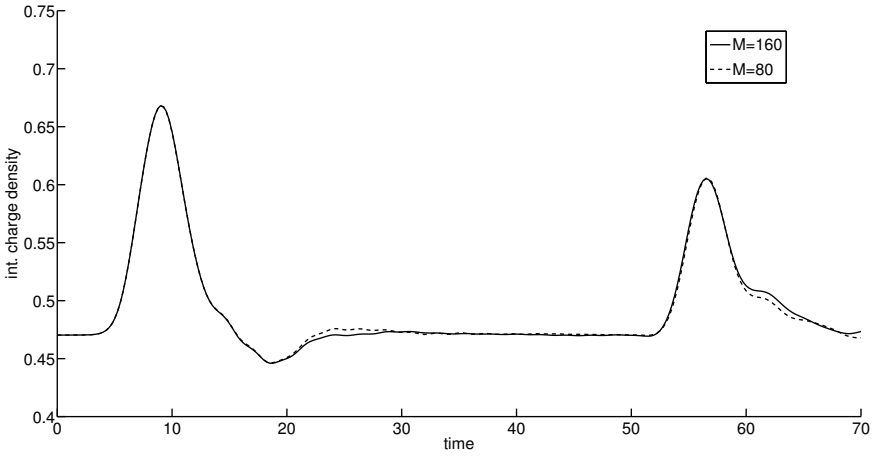

Figure 6.24: Fermions with spin: Andreev/Hole-like reflection at an interaction boundary at site $x_B = 91$. Charge density averaged over sites 80-85. $U_L = 8$, $U_R = 0$, $L = 128$, $N_\uparrow = 32$, $N_\downarrow = 32$, $M = 80$ (dashed line), $M = 160$ (solid line)

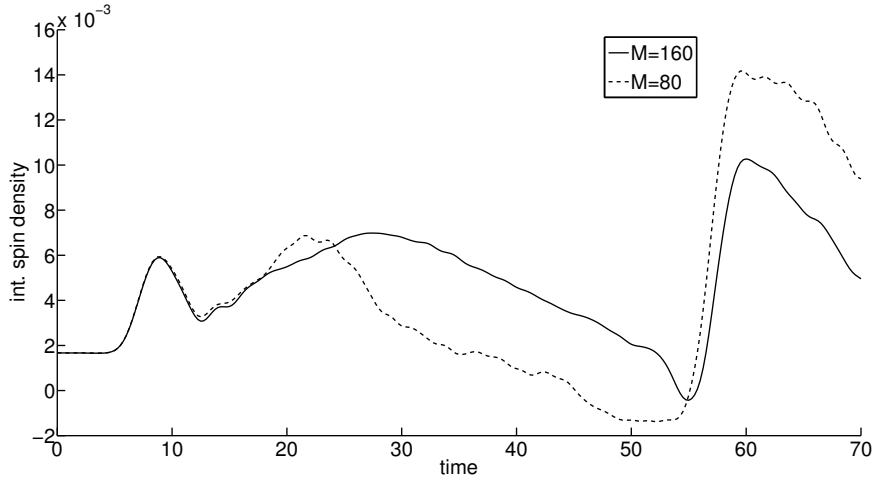

Figure 6.25: Fermions with spin: Andreev/Hole-like reflection at an interaction boundary at site $x_B = 91$. Spin density averaged over sites 80-85. $U_L = 8$, $U_R = 0$, $L = 128$, $N_\uparrow = 32$, $N_\downarrow = 32$, $M = 80$ (dashed line), $M = 160$ (solid line), note the small vertical scale

Discussion. As results for two different matrix dimensions are available, a discussion of the reliability of the simulations such as in the spinless fermion case is possible:

The absolute difference of the charge densities of calculations with $M = 160$ and $M = 80$ is plotted in figure 6.26. For the spin density the difference is given in figure 6.27. The differences are of the same order of magnitude for the charge and spin density. For the spin density the relative error is large in some regions. This can be made clear, if one looks at the definition of the spin density (5.6): Since $\langle \hat{n}_{i\uparrow} \rangle$ is about the same as $\langle \hat{n}_{i\downarrow} \rangle$, the spin density is expected to vary around zero, which gives rise to a large relative error. The situation is much less severe for the charge density, which is an order of magnitude larger than its associated error.

The comparison of the integrated charge density plotted in figure 6.24 for calculations with $M = 160$ and $M = 80$ shows only little deviations. An Andreev-like reflection can be seen in both cases and inspection by eye of the respective charge density plots such as in figure 6.22 a) yields no visible difference. (The plot for $M = 80$ is not given here.)

The averaged/integrated spin density is plotted in figure 6.25 for $M = 80$ and $M = 160$. Beyond $t = 10$ the curves for $M = 80$ and $M = 160$ differ significantly, which owes to the small magnitude of the spin density as explained before. Numerical errors that have little impact on the charge density expectation values cause large deviations here.

Figure 6.28 shows the time dependence of the truncated weight (6.9) for the matrix dimension $M = 160$ compared to $M = 80$. We see that the truncated weight is much larger than in the simulations with spinless fermions and again there is a strong increase around the time where the perturbation hits the boundary. Even if the truncated weight remained constant, one has to keep in mind that the truncation error accumulates. The long-term behaviour that is also shown in the figures ($t = 70$) therefore has to be taken with caution. More reassuring evidence for the accuracy of the simulations would need M much larger than 160, but are not accessible with the simulation program in reasonable time.

The entanglement entropy for cuts at each bond between site and site$+1$ is plotted in figure 6.30. The shade of gray indicates the amount of entanglement between the two resulting subsystems. It is notable that signatures of the reflections are clearly visible in the evolution of the entanglement entropy, as we have already noticed in the spinless fermion case.

Figure 6.29 compares the evolution of the entanglement entropy for matrix dimensions $M = 80$ and $M = 160$. In this case I plotted the maximal

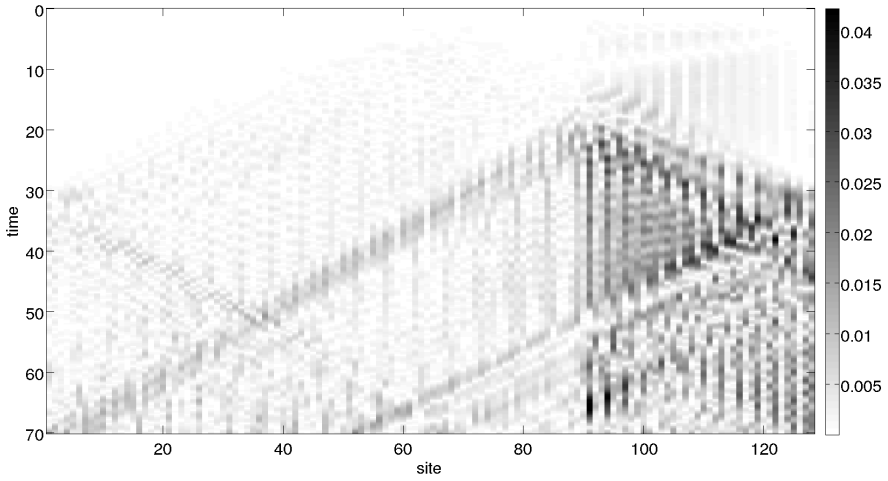

Figure 6.26: Fermions with spin: Andreev/Hole-like reflection. *Charge density:* absolute difference between calculations with $M = 80$ and $M = 160$. $U_L = 8$, $U_R = 0$

value of the entanglement entropy S_l (6.10) at each point in time, which is given by $\max_l S_l(t)$. We see that the curves begin to differ at an early time, earlier than in the spinless fermion case (section 6.2). However, the behaviour is qualitatively similar with an increase when the reflection occurs.

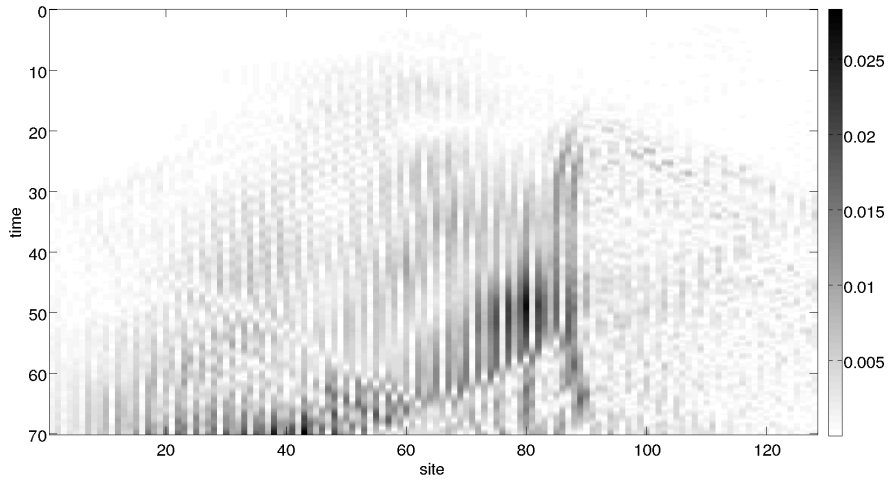

Figure 6.27: Fermions with spin: Andreev/Hole-like reflection. *Spin density:* absolute difference between calculations with $M = 80$ and $M = 160$. $U_L = 8$, $U_R = 0$

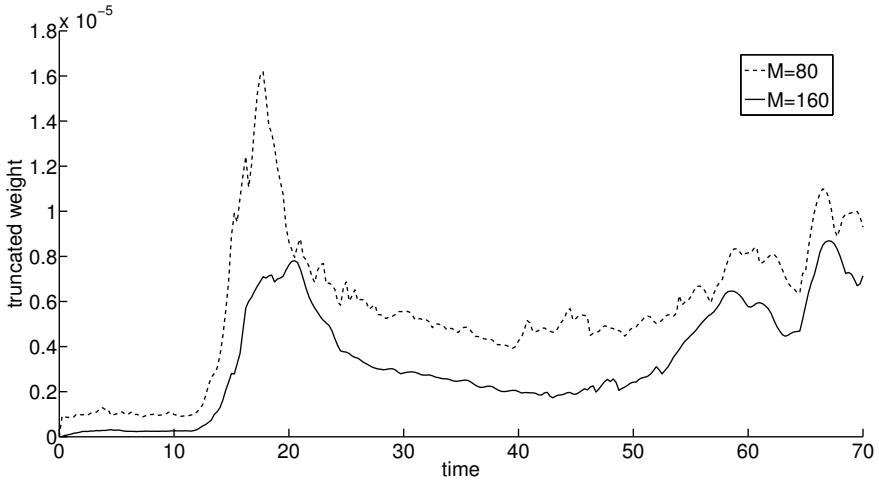

Figure 6.28: Fermions with spin: Andreev/Hole-like reflection. Evolution of the truncated weight (6.9). $U_L = 8$, $U_R = 0$, $M = 80$ (dashed line), $M = 160$ (solid line)

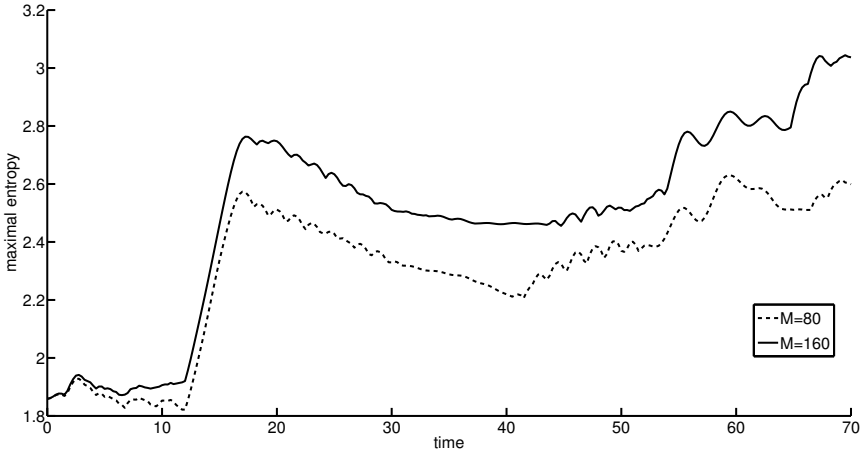

Figure 6.29: Fermions with spin: Andreev/Hole-like reflection. Evolution of the maximal entanglement entropy. $U_L = 8$, $U_R = 0$, $M = 80$ (dashed line), $M = 160$ (solid line)

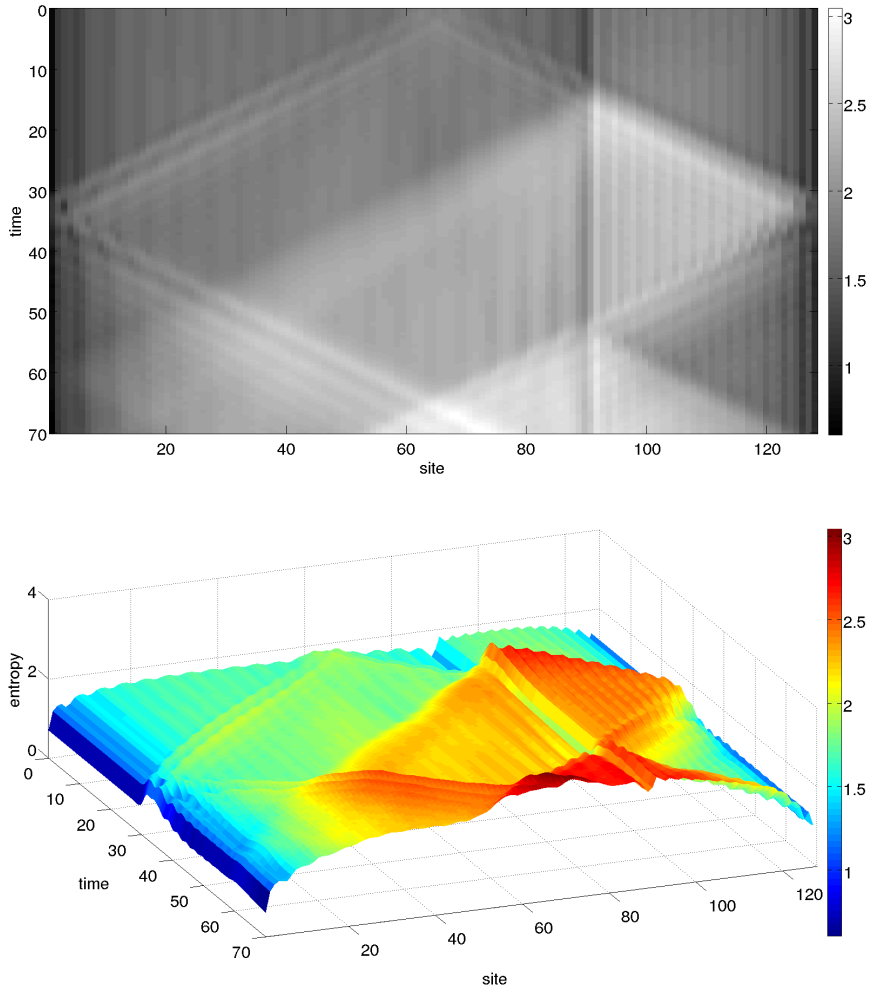

Figure 6.30: Fermions with spin: Andreev/Hole-like reflection. Evolution of the entanglement entropy (top: grayscale, bottom: 3 axes) for cuts between site and site+1; $U_L = 8$, $U_R = 0$, $M = 160$

On-site interactions: $U_L = 10$, $U_R = 2$

While in the previous simulation the fermions in the right part of the system were non-interacting, a non-zero on-site interaction is used here. It was also tried to achieve an uniform particle density, as it was done for the spinless fermion case. To equilibrate particle densities in both parts of the systems one adds the following expression to the Hamiltonian ((5.4), (6.1), (6.2)):

$$\hat{H} \to \hat{H} + \sum_{i \geq x_B}^{L} \epsilon_R \left(\hat{n}_{i\uparrow} + \hat{n}_{i\downarrow} \right) \tag{6.12}$$

Figure 6.31 a) shows Andreev-like reflection for the parameters $U_L = 10$, $U_R = 2$, $L = 128$, $N_\uparrow = 32$, $N_\downarrow = 32$. To equilibrate particle densities I set $\epsilon_R = 0.6$. The corresponding spin density is plotted in figure 6.31 b). Figure 6.33 shows the charge density averaged over sites 80 to 85. The averaged spin density is plotted in figure 6.34. $M = 80$ was used for this parameter set.

In the spin density plot one can see the propagation of a perturbation with a velocity that is higher than expected for the spin degree of freedom. This can be explained by the unavoidable (but small) coupling between charge and spin that is introduced when a perturbation is *not infinitesimal*.

This time the mean particle density is $n = 0.5$ in both parts of the system. If we read off the values for $K_{\rho,L}$ (left part) and $K_{\rho,R}$ (right part) from figure 5.2 we get roughly $K_{\rho,L} \approx 0.6$ and $K_{\rho,R} \approx 0.8$. Equation (5.11) yields a reflection coefficient $\gamma \approx -0.14$. Using the heights of the peaks in figure 6.24 minus the background, the reflection coefficient is $\gamma \approx -0.1$. A systematic analysis for the reflection coefficient for different sets of interaction parameters has not been performed.

In figure 6.36 a perturbation was created using a magnetic field only ($B_0 = 0.5$, $\epsilon_0 = 0$). Comparing figure 6.31 b) to figure 6.36 b), we see that now excitations that travel with velocities near the characteristic spin velocity for $U = 10$ dominate. Figure 6.36 a) shows the charge density which also shows small coupling to the spin degrees of freedom.

a)

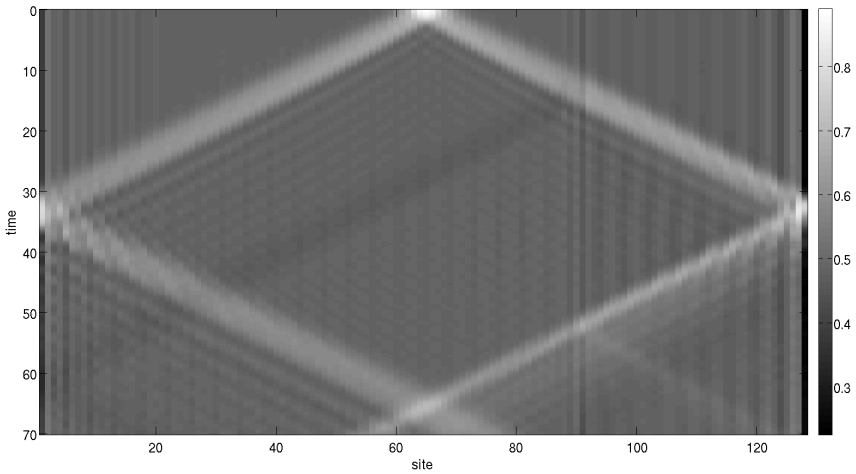

b)

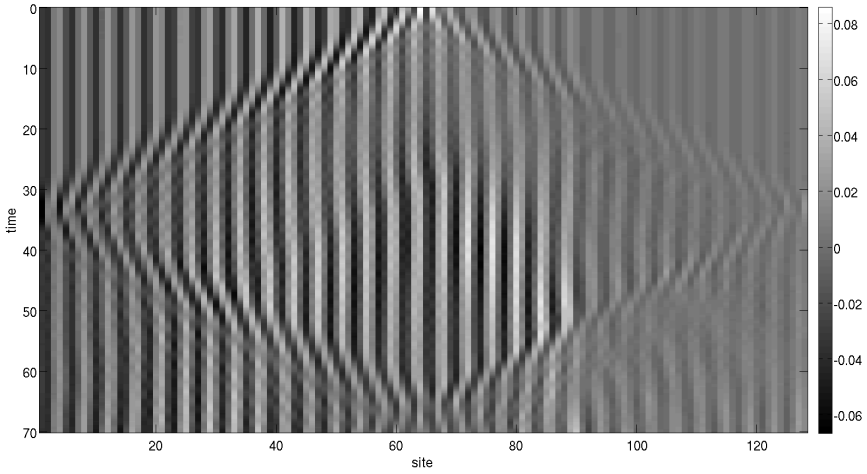

Figure 6.31: Fermions with spin: Andreev/Hole-like reflection at an interaction boundary at site $x_B = 91$: $U_L = 10$, $U_R = 2$; a) Charge density b) Spin density (grayscale); $\epsilon_R = 0.6$, $L = 128$, $N_\uparrow = 32$, $N_\downarrow = 32$, $\epsilon_0 = -2$, $B_0 = 0.05$, $\sigma = 3$, $x_0 = 65$, approximately equal particle densities in left and right half, $M = 80$

a)

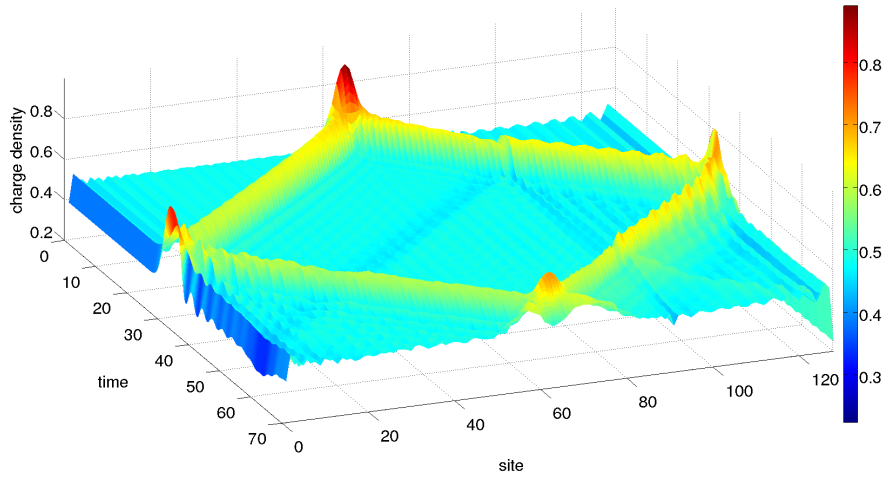

b)

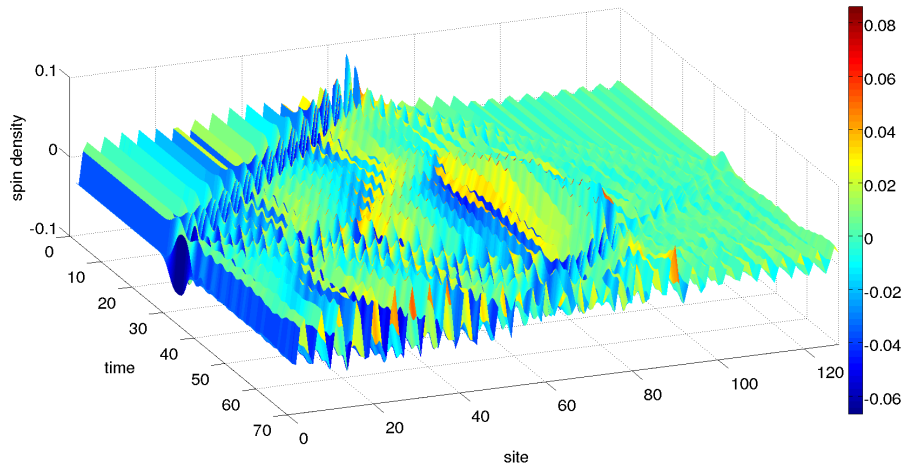

Figure 6.32: Fermions with spin: Andreev/Hole-like reflection. $U_L = 10$, $U_R = 2$, uniform particle density; a) Charge density b) Spin density; same parameters as in figure 6.31; 3 axes plot

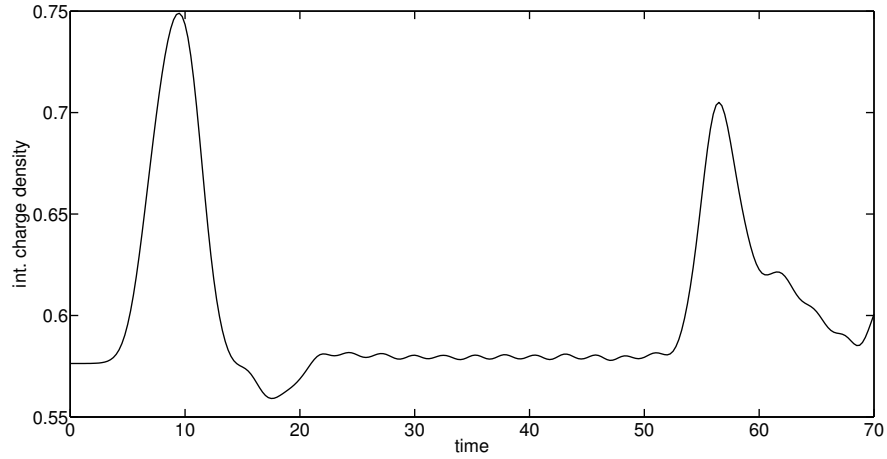

Figure 6.33: Fermions with spin: Andreev/Hole-like reflection. $U_L = 10$, $U_R = 2$. Charge density averaged over sites 80-85. Parameters as in figure 6.31

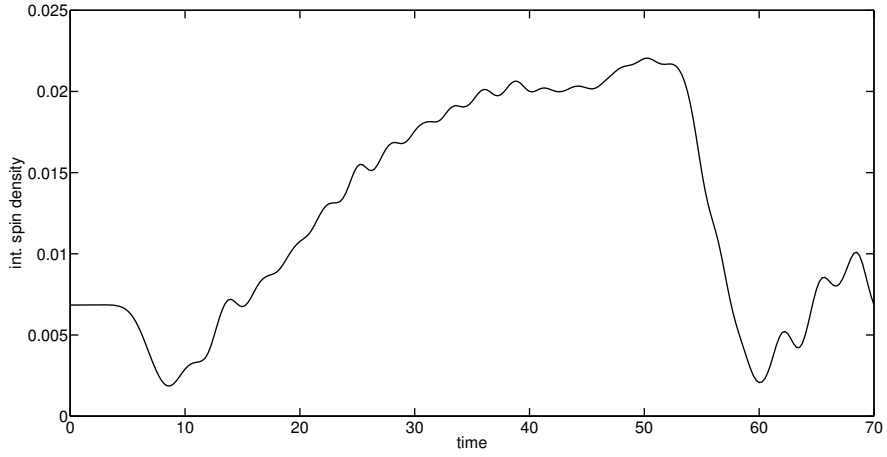

Figure 6.34: Fermions with spin: Andreev/Hole-like reflection. $U_L = 10$, $U_R = 2$. Spin density averaged over sites 80-85. Parameters as in figure 6.31

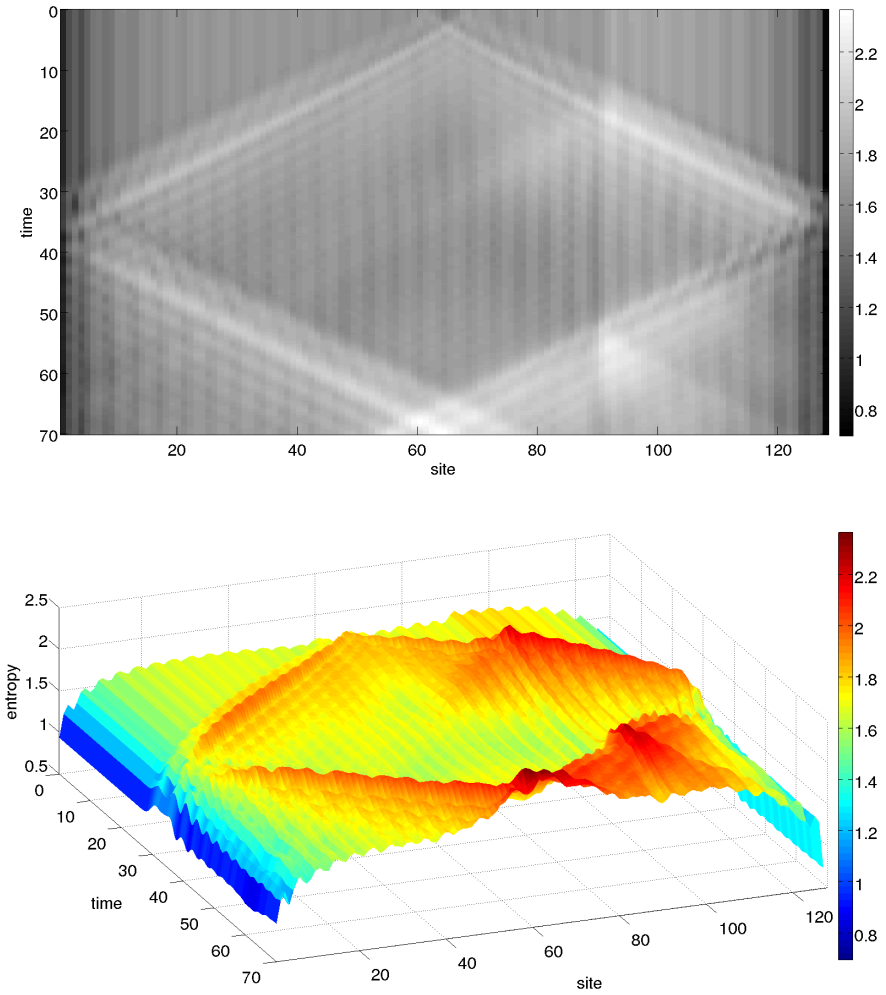

Figure 6.35: Fermions with spin: Andreev/Hole-like reflection. Evolution of the entanglement entropy (top: grayscale, bottom: 3 axes) for cuts between site and site+1; $U_L = 10$, $U_R = 2$, $M = 80$

a)

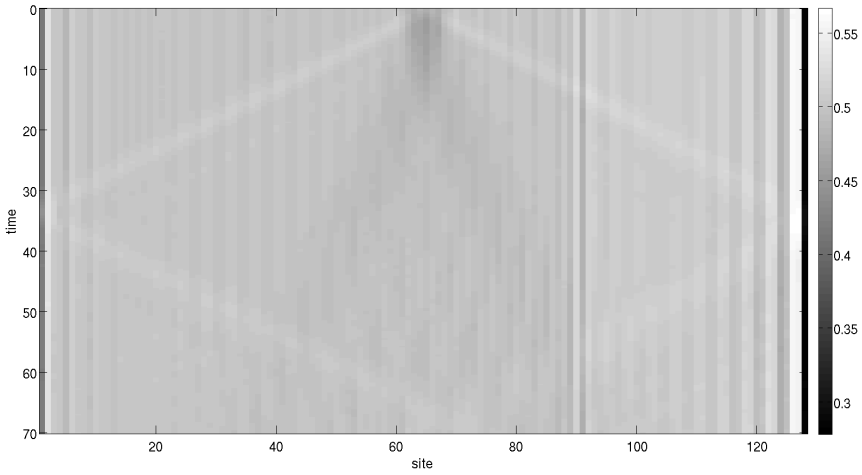

b)

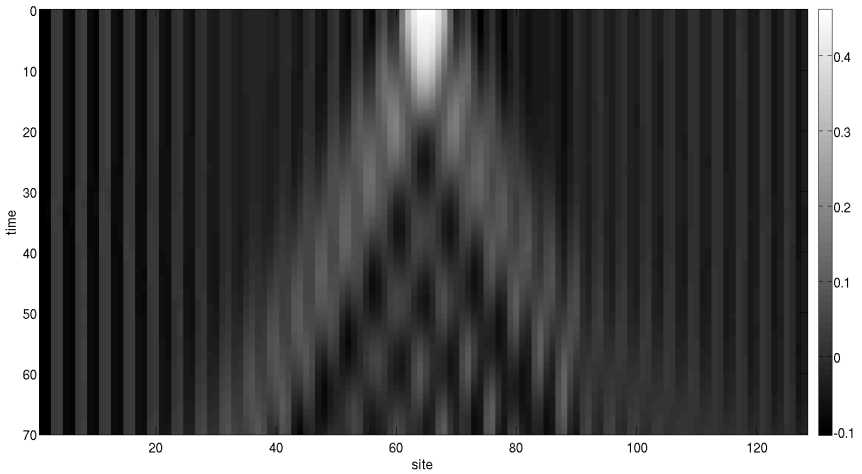

Figure 6.36: Fermions with spin: Andreev/Hole-like reflection. $U_L = 10$, $U_R = 2$. a) Charge density b) Spin density (grayscale); $\epsilon_0 = 0$, $B_0 = 0.5$, other parameters as in figure 6.31

Chapter 7

Conclusions

7.1 Summary

Concepts of quantum information theory have proved being useful for simulating strongly correlated systems. In this context the TEBD (time-evolving block decimation) algorithm was discussed: Approximating the time evolution operator by a product of two-site-operators (or two-site gates) shows that the simulation of a time evolution is equivalent to the simulation of a quantum computation.

For one dimensional lattice systems matrix product states have turned out to be an optimal state representation in physically relevant cases. The TEBD algorithm uses a matrix product state (MPS) representation based on the Schmidt decomposition (2.1).

The efficiency of the TEBD algorithm and related methods of the DMRG kind is due to the restricted amount of entanglement present in most of the physically relevant one-dimensional systems. A quantum computation involving L qubits is efficiently simulatable on a classical computer if it uses poly(L) gates and the entanglement measure E_χ (2.10) does not grow faster than $\log(L)$ [1]. (section 4.4)

Therefore the computational cost of the TEBD algorithm scales only linearly with system size for a fixed MPS matrix dimension M. The scaling of the TEBD algorithm with M is $O(M^3)$.

For open boundary conditions the calculation of matrix elements of single-site operator products also scales as $O(M^3)$.

Sources of error in the TEBD algorithm are due to the approximation of the time evolution operator and the Hilbert space truncation (= reduction of dimension). These error sources are called the Trotter and the truncation error respectively.

Imaginary time evolution is a conceptually simple method to obtain a ground state approximation. Convergence depends on the size of the energy gap of the system. In terms of speed or accuracy variational method or the DMRG are clearly superior. Nevertheless, for the observation of qualitative effects results from imaginary time evolution are sufficient.

The TEBD algorithm was implemented during this work using the C++ programming language. When a conserved quantum number is taken into account a speed-up by a considerable constant factor can be achieved.

The Luttinger-liquid theory describes the low-energy physics of fermions in one dimension, where the Luttinger parameters fully determine the properties of the system. For fermions with spins it predicts that spin and charge are separate degrees of freedom.

The Hubbard model describes interacting fermions on a lattice. It can be used as an underlying microscopic model for the Luttinger liquid. Then the Luttinger parameters are determined by the Hubbard parameters t, U and the mean particle density n.

The theory of inhomogeneous Luttinger liquids predicts normal (positive) and hole-like (negative) reflections, when a *weak* density perturbation hits an interaction barrier. Hole-like reflections are also known as Andreev-like reflections after an effect that occurs at a metal-superconductor boundary.

For simulations of fermions on a lattice a spinless fermion model with nearest-neighbour interaction and the Hubbard model were used.

Perturbations were generated by finding the ground state with applied external fields. These fields are switched of at $t = 0$. One expects that the propagation of the resulting particle density perturbation reveals characteristic properties of the system.

Numerical simulations with adaptive tDMRG for *spinless* fermions were already performed by [37]. A recalculation with TEBD agrees with the results in the cited paper.

For fermions with spin (Hubbard model) and equal number of spin-up and spin-down fermions, these reflection phenomena were also observed in the charge density. However the effect is weak compared to the background charge density. Signatures of the reflections are also seen in the evolution of the entanglement entropy as the perturbation creates entanglement as it propagates.

The results show that Andreev-like reflection in the charge density indeed exists in the *full* Hubbard model. While known analytical results showed the existence of Andreev-like reflections for weak (infinitesimal) perturbations in the idealised Luttinger liquid, these numerical results show that this effect

also exists in the Hubbard model with large perturbations.

Generation of a spin density perturbation proved to be difficult: If one works with external fields, couplings between spin and charge degrees of freedom are unavoidable, as the perturbations have to be large to observe Andreev-like reflection. The inhomogeneous Luttinger liquid theory predicts no reflection.

Simulations of spin-charge separation (section 6.1) allowed in some cases the estimation of the Luttinger parameters u_ρ and u_σ. These are characteristic velocities for charge- and spin-propagation respectively, which differ for interacting fermions. The estimated values were in good agreement with the theoretical prediction.

7.2 Outlook

Numerical time evolution may be useful for the investigation of disordered systems or systems with impurities. There it could help to identify new physical effects. Although a time resolved direct measurement of those might be impossible, one could relate macroscopic measurable effects to their underlying microscopic processes.

Time evolution algorithms, extended to mixed states, also seem to be useful for the simulation of dissipative processes, non-equilibrium physics and decoherence.

Acknowledgements

I want to thank my parents and my sister for their patience;
Martin Ganahl, Michael Krenn and Peter Pippan for helpful discussions;
Ralf Gamillscheg for his parameter parsing code;
Hans Gerd Evertz for his supervision and
Andrew Daley for answering some questions by e-mail.

Bibliography

[1] Guifré Vidal. Efficient classical simulation of slightly entangled quantum computations. *Phys. Rev. Lett.*, 91(14):147902, Oct 2003.

[2] Steven R. White. Density matrix formulation for quantum renormalization groups. *Phys. Rev. Lett.*, 69(19):2863–2866, Nov 1992.

[3] Steven R. White. Density-matrix algorithms for quantum renormalization groups. *Phys. Rev. B*, 48(14):10345–10356, Oct 1993.

[4] Guifré Vidal. Efficient simulation of one-dimensional quantum many-body systems. *Phys. Rev. Lett.*, 93(4):040502, Jul 2004.

[5] David P. DiVincenzo. Two-bit gates are universal for quantum computation. *Phys. Rev. A*, 51(2):1015–1022, Feb 1995.

[6] Michael A. Nielsen and Isaac L. Chuang. *Quantum Computation and Quantum Information*. Cambridge University Press, 2000.

[7] Charles H. Bennett, David P. DiVincenzo, John A. Smolin, and William K. Wootters. Mixed-state entanglement and quantum error correction. *Phys. Rev. A*, 54(5):3824–3851, Nov 1996.

[8] Maria Gracia Eckholt Perotti. Matrix product formalism. Diplomarbeit, Technische Universität München, September 2005.

[9] Andrew John Daley, Corinna Kollath, Ulrich Schollwöck, and Guifré Vidal. Time-dependent density-matrix renormalization-group using adaptive effective Hilbert spaces. *Journal of Statistical Mechanics-Theory and Experiment*, Apr 2004. P04005.

[10] Paolo Zanardi. Virtual quantum subsystems. *Physical Review Letters*, 87(7):077901, 2001.

[11] Paolo Zanardi. Quantum entanglement in fermionic lattices. *Physical Review A*, 65(4):042101, 2002.

[12] Stellan Östlund and Stefan Rommer. Thermodynamic limit of density matrix renormalization. *Phys. Rev. Lett.*, 75(19):3537–3540, Nov 1995.

[13] Stefan Rommer and Stellan Östlund. Class of ansatz wave functions for one-dimensional spin systems and their relation to the density matrix renormalization group. *Phys. Rev. B*, 55(4):2164–2181, Jan 1997.

[14] F. Verstraete, J. I Cirac, and V. Murg. Matrix product states, projected entangled pair states, and variational renormalization group methods for quantum spin systems. *arXiv, cond-mat/0907.2796*, July 2009. Adv. Phys. 57,143 (2008).

[15] Peter Pippan. The density matrix renormalization group and matrix product states. Diplomarbeit, Technische Universität Graz, 2006.

[16] Ulrich Schollwöck. The density-matrix renormalization group. *Reviews of Modern Physics*, 77:259, 2005.

[17] Peter Pippan, Steven R. White, and Hans Gerd Evertz. Efficient matrix-product state method for periodic boundary conditions. *Phys. Rev. B*, 81(8):081103, Feb 2010.

[18] Andrew John Daley. *Manipulation and Simulation of Cold Atoms in Optical Lattices*. Dissertation, Leopold-Franzens-Universität Innsbruck, 2005.

[19] A. T. Sornborger and E. D. Stewart. Higher-order methods for simulations on quantum computers. *Phys. Rev. A*, 60(3):1956–1965, Sep 1999.

[20] Dominique Gobert, Corinna Kollath, Ulrich Schollwöck, and Gunter Schütz. Real-time dynamics in spin-$\frac{1}{2}$ chains with adaptive time-dependent density matrix renormalization group. *Phys. Rev. E*, 71(3):036102, Mar 2005.

[21] Boost C++ Libraries. `http://www.boost.org`. Retrieved 09/02/2010.

[22] LAPACK – Linear Algebra PACKage. `http://www.netlib.org/lapack/index.html`. Retrieved 09/02/2010.

[23] Martin Jakob Ganahl, Elias Rabel, and Hans Gerd Evertz. Propagation of bound states in Heisenberg XXZ chains, 2010. Poster, International Seminar and Workshop on Quantum Information Concepts for Condensed Matter Problems, Dresden.

[24] Martin Jakob Ganahl. Simulation des Spin-Transports in eindimensionalen Quanten-Heisenberg Spin 1/2 Systemen in reeller Zeit. Diplomarbeit, Technische Universität Graz, 2010.

[25] Guifré Vidal. Classical simulation of infinite-size quantum lattice systems in one spatial dimension. *Phys. Rev. Lett.*, 98(7):070201, Feb 2007.

[26] Michael Zwolak and Guifré Vidal. Mixed-state dynamics in one-dimensional quantum lattice systems: a time-dependent superoperator renormalization algorithm. *Physical Review Letters*, 93:207205, 2004.

[27] W J Caspers. *Spin Systems*. World Scientific, 1989.

[28] Assa Auerbach. *Interacting Electrons and Quantum Magnetism*. Graduate Texts in Contemporary Physics. Springer-Verlag, 1994.

[29] H. J. Schulz, G. Cuniberti, and P. Pieri. Fermi liquids and Luttinger liquids. *arXiv, cond-mat/9807366*, 1998.

[30] Philippe Nozières. *Theory of Interacting Fermi Systems*. Advanced Book Classics. Westview Press, 1964, 1997.

[31] Thierry Giamarchi. *Quantum Physics in One Dimension*, volume 121 of *International Series of Monographs on Physics*. Oxford University Press, 2004.

[32] Corinna Kollath and Ulrich Schollwöck. Cold fermi gases: a new perspective on spin-charge separation. *New Journal of Physics*, 8(10):220, 2006.

[33] H. J Schulz. Interacting fermions in one dimension: from weak to strong correlation. *arXiv, cond-mat/9302006*, February 1993.

[34] I. Safi and H. J. Schulz. Transport in an inhomogeneous interacting one-dimensional system. *Phys. Rev. B*, 52(24):R17040–R17043, Dec 1995.

[35] Inès Safi and H. J. Schulz. Interacting electrons with spin in a one-dimensional dirty wire connected to leads. *Phys. Rev. B*, 59(4):3040–3059, Jan 1999.

[36] Inès Safi and H. J Schulz. Transport through a single-band wire connected to measuring leads. *arXiv, cond-mat/9605014*, May 1996.

[37] A. Daley, P. Zoller, and B. Trauzettel. Andreev-Like reflections with cold atoms. *Physical Review Letters*, 100(11):110404, 2008.

[38] C. Kollath, U. Schollwöck, and W. Zwerger. Spin-charge separation in cold fermi gases: A real time analysis. *Phys. Rev. Lett.*, 95(17):176401, Oct 2005.

[39] Tobias Ulbricht and P. Schmitteckert. Is spin-charge separation observable in a transport experiment? *EPL (Europhysics Letters)*, 86(5):57006, 2009.